

Nonlinear optical organic crystals for photonic applications

A dissertation submitted to
ETH Zurich

for the degree of
Doctor of Natural Sciences

presented by

Lukas Mutter

Dipl. Phys. ETH
born on the 15th May 1977
citizen of Blitzingen (VS), Switzerland

accepted on the recommendation of

Prof. Dr. P. Günter, examiner
Prof. Dr. M. Zgonik, co-examiner

Zürich 2007

Cover page:

Collage of photographs of DAST; shown are

- Planar waveguiding in ion implanted waveguides
- Photobleached spot
- Mach Zehnder structures realized by direct e-beam exposure
- Mach Zehnder structures with gold electrodes
- Channel waveguiding in DAST e-beam written waveguides
- DSTMS crystal

Contents

Abstract	vii
Zusammenfassung	xi
1 Nonlinear optics of organic materials	1
1.1 Introduction to nonlinear optics	1
1.2 Microscopic and macroscopic properties of organic materials	4
1.3 Nonlinearities of organic molecules and crystals	5
1.3.1 Molecular dispersion of the nonlinear susceptibility	5
1.3.2 Optimization of the second-order activity	6
1.4 The electro-optic effect in organic materials	7
1.5 Frequency dependence of the linear and nonlinear optical properties	8
1.6 High-speed modulation	9
1.6.1 Traveling-wave Mach-Zehnder modulator	9
1.6.2 Polymer and LiNbO ₃ Mach-Zehnder modulators	12
1.7 Microring resonators for electro-optic modulation	13
1.7.1 Basic principle of microring resonators	14
1.7.2 Electro-optic modulation using microring resonators	16
1.7.3 Comparison between Mach-Zehnder and microring resonators	16
1.8 Conclusion	19
2 Material properties of the organic crystal DAST	21
2.1 Crystal structure	21
2.2 Growth of single crystals	22
2.3 Thin film growth	24
2.4 Linear optical properties	25
2.5 Electro-optic and nonlinear optical properties	25
2.6 THz generation in DAST	28
2.7 Waveguide structuring of DAST before this work	28

2.8	Summary of the most important material properties of DAST	29
3	Photobleaching and optical properties of the organic crystal DAST	31
3.1	Introduction	31
3.2	Refractive indices and absorption coefficients	32
3.2.1	Experimental details	32
3.2.2	Results and discussion	37
3.3	Photobleaching of DAST	37
3.3.1	Estimation of the refractive indices in bleached DAST	38
3.3.2	Determination of the bleaching depth	40
3.3.3	Modeling of the bleaching process	40
3.3.4	Results and discussion	42
3.4	Conclusions	43
4	Ion implanted optical waveguides in DAST	45
4.1	Introduction	45
4.2	Ion implantation experiments	46
4.3	Refractive index profiles of He ⁺ and H ⁺ ion implantation	47
4.3.1	Model of ion implantation	47
4.3.2	Reflection scan measurement method	47
4.3.3	Refractive index profile of He ⁺ ion implantation	48
4.3.4	Refractive index profile of H ⁺ ion implantation	50
4.4	Mode analysis	52
4.4.1	Barrier coupling method	52
4.4.2	Results	53
4.5	Waveguiding experiments	54
4.5.1	Planar waveguiding	54
4.5.2	Channel waveguiding	55
4.6	Conclusions	55
5	Nonlinear optical properties of ion implanted DAST waveguides	57
5.1	Introduction	57
5.2	Ion implanted waveguides in DAST	58
5.3	Second-harmonic reflection measurement	59
5.4	Ion-induced modification in organic media	61
5.4.1	Model	61
5.4.2	Susceptibility profile	63
5.5	Electro-optic modulation	64

5.6	Conclusions	66
6	Direct electron beam writing of DAST channel waveguides	67
6.1	Introduction	67
6.2	Electron beam experiments	68
6.3	Refractive index profile induced by e-beam exposure	69
6.3.1	Model for e-beam exposure	69
6.3.2	Reflection scan measurement method	70
6.3.3	Results: Refractive index profile	71
6.4	Dispersion of the refractive index change	72
6.5	Realization of channel waveguides	73
6.5.1	Concept of channel waveguide patterning	73
6.5.2	Waveguiding observation	75
6.6	Electro-optic modulation	76
6.7	Towards single mode waveguides	78
6.8	Conclusion	79
7	New materials for nonlinear optical applications	81
8	Linear and nonlinear optical properties of the organic crystal DSTMS	85
8.1	Introduction	85
8.2	Crystal properties	86
8.3	Refractive indices of DSTMS	87
8.4	Absorption coefficients of DSTMS	90
8.5	Nonlinear optical properties	90
8.6	Phase-matched parametric interaction	92
8.7	Conclusions	94
9	Conclusions	95
A	Atmospheric dependence of the bleaching process	99
B	Sample tilting in ion implantation and single mode waveguides	101
C	Ion implanted Mach-Zehnder modulators	105
	References	110
	Acknowledgments	120

CONTENTS

Curriculum vitae	121
List of publications	122

Abstract

In telecommunication the bit rate transmitted has increased rapidly in the last decades from 0.2 Gbit/s in 1980 to 40 Gbit/s nowadays [1]. In laboratories, transmission rates of 1 Tbit/s have already been demonstrated [1]. To increase the bandwidth furthermore and to realize compacter integrated devices, a lot of research is dedicated to the investigation of new concepts in telecommunication. Both photonic crystals and microring resonators are ideally suited for dense wavelength division multiplexing, and intense research efforts are currently focused on integrating them into chip devices. Important innovations have also been attained in the field of new fabrication technologies and material research.

The ferroelectric material LiNbO_3 is now widely used in telecommunication for beam steering, modulation and signal processing through the electro-optic effect by which the phase of an optical wave is altered by an applied electrical field. Aiming for transmission rates of over 100 Gbit/s per channel, LiNbO_3 shows however some essential disadvantages. Its moderate electro-optic activity results in an unfavorable long interaction length (up to 1 cm) between the optical carrier wave and the electric modulation field. Furthermore, the large difference of the dielectric constant at the modulation and the optical frequencies $\epsilon_{33} = 28, n^2 = 4.6$, respectively, limits the modulation speed to about 100 Gbit/s, due to velocity mismatch. With respect to these material requirements two organic material classes, electro-optic polymers and organic crystals show some essential benefits, which can not be overlooked. The theoretical limit of their nonlinearity and the electro-optic activity is far from being reached yet. At the present state poled electro-optic polymers as well as appropriately designed organic crystals already have electro-optic coefficients which are by a factor two to ten higher than the one of LiNbO_3 [2]. Moreover, organic materials are well suited for high-speed modulation due to an almost pure electronic origin of the optical nonlinearity, and hence a very low material dispersion of the dielectric constant ($\epsilon \approx n^2$). Therefore, organic electro-optic materials have been intensively studied as integrated optics constituents during the last years.

Electro-optic active polymers are potentially cheap and thin film processing is easy, nevertheless they often show thermal and photochemical instabilities. On the other hand, organic crystals have superior nonlinearities, thermal and photochemical stability, but growth of high quality thin films and waveguide structuring are still challenges on the way to develop very large scale integrated (VLSI) photonic devices. Hence, it is of fundamental importance to develop new techniques for the fabrication of optical waveguides in organic crystalline materials.

The development of new waveguide structuring techniques of organic crystals is the main focus of this thesis. Particularly, we have been working with an ionic salt DAST (4-N, N-dimethylamino-4'-N'-methyl-stilbazolium tosylate), which has attracted a lot of attention due to its outstanding nonlinear optical properties. We present our results on photo structuring by photobleaching, the realization of planar waveguides by low fluence ion implantation, and the very interesting approach of channel waveguide patterning by direct electron beam irradiation. A first electro-optic demonstration in Mach-Zehnder modulators realized by electron beam exposure is shown. Besides these, also latest results on the design and characterization of new organic crystals with superior material properties compared to the organic crystal DAST are given.

The method of photobleaching, which has already been used to alter the refractive index of polymers by changing the molecular structure by illumination of light near their absorption edge, has been applied to the organic crystal DAST. A large reduction of the highest refractive index of DAST $\Delta n_1 = -0.5$ at a wavelength of $1.55 \mu\text{m}$ has been observed. Therefore, the method is well suited to produce high refractive index contrast waveguides. Fundamental investigations showed that the process of photobleaching in DAST is a photooxidation process. Under oxygen atmosphere the bleaching process has been fastened up by a factor of 2 to 3 compared to standard atmosphere. This technique can be applied to produce channel waveguides in crystals assuming that vertical light confinement is already achieved by other means, e.g. in thin films.

An important step towards the realization of waveguides in bulk crystals has been made by applying the technique of ion implantation to the organic crystal DAST. Ion implantation is widely used for the fabrication of waveguides in inorganic materials, in which a perturbed region with a lowered index of refraction is formed at the end of the ion track, whereas the properties in the waveguide core are mostly preserved. For the first time to our knowledge the process of H^+ ion implantation has been exploited to successfully realize planar waveguide structures in the organic crystal DAST. Contrary to the mechanism in inorganic crystals, where the refractive index change is produced by defect production in the crystal structure, the ionization of the target electrons during the implantation process changes the chemical composition and is mainly responsible for the refractive index change in organic crystals. A simple model, which relates the molecular changes to the measured refractive index and nonlinear susceptibility profiles has been introduced. Since the nonlinear properties are mostly preserved, which has been shown by measuring the second-harmonic efficiency on a wedged-polished sample, the technique of ion implantation opens new perspectives for using DAST in integrated optics devices. Moreover, first electro-optic modulation in the produced planar waveguide structures has been demonstrated and channel waveguides have been produced by standard photolithography and reactive ion etching.

Another fundamental breakthrough in the realization of channel waveguide has been made by direct electron beam irradiation by which the refractive index in DAST is reduced. Applying a new concept of direct electron beam patterning, channel waveguides in DAST crystals have

been successfully realized in a single process step. The waveguides have been formed by patterning two lines separated by a few microns with a reduced index of refraction. Due to scattering, the electron beams are broadened in the target material (DAST) and as a result finally merge a few micrometers below the surface. Therefore confinement is also realized in vertical direction. Waveguiding has been demonstrated at telecommunication wavelengths. Mach-Zehnder modulators have also been produced by this novel technique and a first electro-optic modulation has been demonstrated therein. The approach of direct electron beam patterning is of substantial interest since the waveguide core is not affected by electron beam irradiation and therefore the nonlinearities are preserved.

In future, new materials, which are easier to process and exhibit even higher nonlinearities than the one used at the present state, are desired. The DAST derivative DSTMS (4-N, N-dimethylamino-4'-N'-methyl-stilbazolium 2,4,6-trimethylbenzenesulfonate) shows superior growth behavior and equally high nonlinearities compared to DAST. The linear and nonlinear properties of the new material have been investigated and showed that DSTMS is an interesting candidate for electro-optic applications, parametric light generation as well as THz generation.

Zusammenfassung

Während der letzten Jahre sind die Bitraten, welche in der modernen Telekommunikation übertragen werden, von 0.2 Gbit/s 1980 auf 40 Gbit/s heutzutage angestiegen. [1]. In Forschungslaboratorien wurden bereits Übertragungsraten von 1 Tbit/s erzielt [1]. Viele wissenschaftliche Untersuchungen haben sich mit der Erforschung von neuen Konzepten beschäftigt, um die Bandbreite in der Telekommunikation weiter zu erhöhen und kompaktere integrierte Devices herzustellen. Photonische Kristalle und Mikroresonatoren sind ideal geeignet für Wellenlängendemultiplexing und haben grosses Interesse geweckt, da diese mit grosser Packungsdichte auf einem Chip integriert werden können. Auch auf dem Gebiet der Materialforschung und der Entwicklung neuer Technologien wurden wichtige Neuerungen erzielt.

Heutzutage ist das ferroelektrische Material Lithiumniobat zur elektro-optischen Datenverarbeitung in der Telekommunikation weitverbreitet. Mittels des elektro-optischen Effektes wird durch anlegen eines elektrischen Feldes die Phase einer optischen Welle beeinflusst. Das Ziel in naher Zukunft sind Übertragungsraten von über 100 Gbit/s pro Übertragungskanal. LiNbO₃ zeigt diesbezüglich einige Nachteile. Seine nur moderate elektro-optisch Aktivität führt dazu, dass die Interaktionslängen zwischen dem optischen Informationsträger und dem Modulationsfeld relativ lang sein müssen (mehr als 1 cm). Des Weiteren treten bei hohen Modulationsgeschwindigkeiten von über 100 Gbit/s Phasendifferenzen zwischen dem Modulationsfeld und der optischen Welle auf, da die dielektrischen Konstanten von Lithiumniobat bei der Modulationsfrequenz und der optischen Frequenz sehr unterschiedlich sind ($\epsilon_{33} = 28, n^2 = 4.6$). Bezüglich dieser Materialeigenschaften zeigen die in letzter Zeit intensiv untersuchten organischen Materialien; elektro-optische Polymere und organische Kristalle, einige Vorteile, die nicht übersehen werden sollten. Ihre nichtlinear optische Aktivität ist zum Zeitpunkt bereits um einen Faktor 2 bis 10 mal höher als die von LiNbO₃ [2], und theoretische Analysen zeigen weiteres Steigerungspotential. Des Weiteren sind organische Materialien ideal geeignet für Hochgeschwindigkeitsmodulation, da ihre optische Nichtlinearität fast ganz elektronischen Ursprungs ist. Daher weist die dielektrische Konstante nur eine geringe Materialdispersion auf ($\epsilon \approx n^2$).

Elektro-optisch aktive Polymere haben den Vorteil, dass sie billig sind und ihre Dünnschichtverarbeitung relativ einfach ist. Ihre Wärmeempfindlichkeit sowie die photochemische Instabilität stellen aber sehr oft Probleme dar. Andererseits haben organische Kristalle höhere Nichtlinearitäten, bessere thermische und photochemische Beständigkeit. Die Herstellung von

dünnen einkristallinen Filmen und die Fabrikation von Wellenleitern sind aber noch immer sehr anspruchsvoll. Daher ist es äusserst wichtig, neue Technologien für die Herstellung von Wellenleitern in organischen Kristallen zu erforschen und zu entwickeln.

Der Schwerpunkt dieser Forschungsarbeit beinhaltet deshalb die Entwicklung von neuen Strukturierungstechniken für organische Kristalle, im Speziellen des organischen Salzes DAST (4-N, N-dimethylamino-4'-N'-methyl-stilbazolium tosylate). Diesem wurde wegen seiner ausserordentlichen nichtlinearen optischen Eigenschaften in der Vergangenheit grosse Beachtung geschenkt.

Wir präsentieren unsere Resultate der Photostrukturierung, der planaren Wellenleiterherstellung mittels Ionenimplantation mit niedrigen Dosen und der äusserst interessanten neuen Methode der Realisierung von Kanalwellenleitern mittels direkter Elektronenlithographie. So konnten mittels der letzten Methode Mach-Zehnder Modulatoren hergestellt und eine erste elektro-optische Modulation in diesen gezeigt werden. Des Weiteren berichten wir über neu entwickelte und synthetisierte organische Kristalle, welche bessere Materialeigenschaften als DAST besitzen.

Mittels Bestrahlung von Licht, welches eine Wellenlänge nahe der Absorptionskante des Materials hat, kann die molekulare Struktur und somit der Brechungsindex von Polymeren geändert werden, so genanntes Photobleaching. Wir haben diese Methode benutzt, um den Brechungsindex von DAST zu modifizieren. Eine grosse Reduktion des Brechungsindex n_1 von DAST bei $1.55 \mu\text{m}$ von $\Delta n_1 = -0.5$ wurde erzielt. Die Methode ist deshalb sehr gut zur Herstellung von Wellenleitern mit hohem Brechungsindexkontrast geeignet. Grundlegende Untersuchungen des Prozesses haben gezeigt, das Bleaching von DAST ein Photooxidationsprozess ist. Unter reiner Sauerstoffatmosphäre wurde ein Anstieg der Geschwindigkeit des Bleachingprozesses um einen Faktor 2 bis 3 gemessen verglichen zu Bleaching unter normalatmosphärischen Bedingungen. Diese Technik ist deshalb bestens geeignet, um Kanalwellenleiter herzustellen. Eine vertikale Eingrenzung des Lichtes mittels anderer Methoden ist jedoch dazu erforderlich, zum Beispiel durch Verwendung dünner Filme.

Ein wichtiger Schritt zur Herstellung von Wellenleitern in DAST Kristallen wurde durch die erstmalige Verwendung der Technik der Ionenimplantation bei organischen Kristallen erzielt. Diese Methode ist bekannt und wird oft zur Herstellung von Wellenleitern in anorganischen Materialien verwendet. In diesen wird am Ende der Ionenbahn die Kristallstruktur stark modifizierte, wo hingegen die Veränderungen der Kristallstruktur im Wellenleiterkern nur minimal sind. Zum ersten Male, soweit uns bekannt ist, wurde der Prozess von H^+ Ionenimplantation dazu verwendet, um erfolgreich Wellenleiter in organischen Materialien herzustellen, d.h. in diesem Fall in DAST. Im Gegensatz zu anorganischen Materialien, bei welchen die Brechungsindexänderung durch Defekte in der Kristallstruktur hervorgerufen wird, ist die Brechungsindexänderung in organischen Materialien chemischer Natur, induziert durch die Ionisation von Elektronen des Target Materials. Ein einfaches Modell, welches die Änderungen auf molekularer Ebene mit denen des Brechungsindex und der nichtlinearen Suszeptibilität in Beziehung

setzt, wurde entwickelt. Die nichtlinear optischen Eigenschaften werden dabei durch die Ionenimplantation kaum beeinflusst und bleiben grösstenteils erhalten. Dies wurde durch Messung der Effizienz der Erzeugung der 2ten Harmonischen an der Oberfläche einer keilförmig polierten Probe gezeigt. Diese Methode der Ionenimplantation öffnet neue Perspektiven, um DAST auch in der integrierten Optik zu verwenden. Um so mehr, da bereits eine erste elektro-optische Modulation in den hergestellten planaren Wellenleitern demonstriert und Kanalwellenleiter mittels Photolithographie in Kombination mit reaktivem Ionenätzen hergestellt wurden.

Ein anderer fundamentaler Fortschritt wurde durch die Verwendung von Elektronenlithographie erzielt, wodurch Kanalwellenleiter durch direkte Belichtung in DAST realisiert werden konnten. Mit einem neu entwickelten Konzept, bei dem zwei Linien mit reduziertem Brechungsindex in einem Abstand von einigen Mikrometern belichtet werden, sind Wellenleiter in einem einzigen Schritt produziert worden. Durch Streuung der Elektronen im Material wird der Elektronenstrahl im Material aufgeweitet. Daher überlappen die zur Belichtung der beiden Linien verwendeten Elektronenstrahlen in einer Tiefe von ein paar Mikrometern. Auf diese Weise wird eine laterale und vertikale Eingrenzung des Lichtes realisiert. Optische Wellenleitung für Telekommunikationswellenlängen wurde gezeigt. Ebenfalls wurden mittels dieser neuen Methode Mach-Zehnder Modulatoren hergestellt und eine erste elektro-optische Modulation demonstriert. Dieses neue Konzept ist von grossem Interesse für die Elektro-Optik und nicht-lineare Optik, weil der Wellenleiterkern durch den Belichtungsprozess nicht beschädigt wird und deshalb die Nichtlinearität erhalten bleibt.

Von grossem Interesse für zukünftige Anwendungen sind Materialien, welche einfacher zu bearbeiten sind und hohe Nichtlinearitäten aufweisen. Das DAST Derivat DSTMS (4-N, N-dimethylamino-4'-N'-methyl-stilbazolium 2,4,6-trimethylbenzenesulfonate) zeigt bessere Wachstumseigenschaften im Vergleich zu DAST und besitzt gleich grosse Nichtlinearitäten. Die linearen und nichtlinear optischen Eigenschaften dieses neuen organischen Kristalls wurden untersucht und haben gezeigt, dass DSTMS ein sehr interessanter Kandidat für elektro-optische Anwendungen, parametrische Erzeugung von Licht und THz Generation ist.

Chapter 1

Nonlinear optics of organic materials

In this chapter we give a short introduction to nonlinear optics of organic materials. First we state the conventions that are further used in the thesis, since in literature different notations are present. Therefore, special care has to be taken while comparing results from different sources. After a brief introduction to the topic of nonlinear optics of nonmagnetic materials, the most important relations between microscopic and macroscopic linear and nonlinear material properties valid for organic materials are given. A description of the electro-optic effect, which is of special interest concerning the realization of integrated optic switches and modulators in organic materials, is given at the end of this chapter.

1.1 Introduction to nonlinear optics

In nature, various optical effects with breathtaking beauty are present. Astonishing, colorful rainbows, dim orange-red sunsets or the deep blue of water and sky are only some of them, which are attracting our attention. The beauty of physics is that not only these optical effects can be described with the Maxwell's equations but also more sophisticated physical phenomena, which are observed and studied in optical laboratories and used in modern telecommunications nowadays.

The Maxwell's equations given in SI units are [3, 4]:

$$\mathit{rot}\mathbf{E} = -\frac{\partial\mathbf{B}}{\partial t} \quad (1.1)$$

$$\mathit{div}\mathbf{D} = \rho \quad (1.2)$$

$$\mathit{div}\mathbf{B} = 0 \quad (1.3)$$

$$\mathit{rot}\mathbf{H} = \mathbf{j} + \frac{\partial\mathbf{D}}{\partial t}, \quad (1.4)$$

where \mathbf{E} is the electric field, \mathbf{B} the magnetic induction, \mathbf{D} the dielectric displacement, and \mathbf{H} the magnetic field strength. ρ denotes the free carrier density and \mathbf{j} the current density in the material. An electric field, which is present in a dielectric material, will lead to a redistribution

of the electric charges and hence result in an induced polarization \mathbf{P} , which is related to the dielectric displacement vector \mathbf{D} by [3, 4]

$$\mathbf{D} = \epsilon_0 \mathbf{E} + \mathbf{P}, \quad (1.5)$$

where ϵ_0 is the dielectric permittivity in vacuum. Taking the assumptions that no free carriers exist ($\rho = 0$) and no current is flowing in the material ($\mathbf{j} = 0$), we obtain by combining Eqs. (1.1), (1.4) and (1.5) for a non magnetic medium ($\mathbf{B} = \mu_0 \mathbf{H}$) the following wave equation

$$\text{rot}(\text{rot}\mathbf{E}) + \frac{1}{c^2} \frac{\partial^2 \mathbf{E}}{\partial t^2} = -\mu_0 \frac{\partial^2 \mathbf{P}}{\partial t^2}, \quad (1.6)$$

for which derivation $\epsilon_0 \mu_0 = 1/c^2$ was used. c denotes the speed of light in vacuum. To solve this equation, the induced polarization has to be expressed as a function of the electric field, which is normally rather complicated. Nevertheless, assuming that the material is reacting instantaneous to the applied electric field, the polarization can be expanded in a Taylors series. Using Einstein's summation convention, the polarization is given by [5–7]

$$P_i(\mathbf{r}, t) = P_{0,i} + \epsilon_0 \chi_{ij}^{(1)} E_j(\mathbf{r}, t) + \epsilon_0 \chi_{ijk}^{(2)} E_j(\mathbf{r}, t) E_k(\mathbf{r}, t) + \dots, \quad (1.7)$$

where $\chi^{(1)}$ is the linear susceptibility and $\chi^{(2)}$ the first-order nonlinear susceptibility tensor. The denominators of the Taylor expansion are included in the definition of the susceptibilities. $P_{0,i}$ denotes the possible static polarization of the material. Splitting up the induced polarization term in a linear and a nonlinear term

$$P_i(\mathbf{r}, t) = P_{0,i} + P_{i,lin}(\mathbf{r}, t) + P_{i,nl}(\mathbf{r}, t) \quad (1.8)$$

with

$$P_{i,lin}(\mathbf{r}, t) = \epsilon_0 \chi_{ij}^{(1)} E_j(\mathbf{r}, t) \quad (1.9)$$

$$P_{i,nl}(\mathbf{r}, t) = \epsilon_0 \chi_{ijk}^{(2)} E_j(\mathbf{r}, t) E_k(\mathbf{r}, t) + \dots, \quad (1.10)$$

the wave equation (1.6) can be simplified and we obtain

$$\text{rot}(\text{rot}\mathbf{E}) + \frac{\epsilon}{c^2} \frac{\partial^2 \mathbf{E}}{\partial t^2} = -\mu_0 \frac{\partial^2 \mathbf{P}_{nl}}{\partial t^2} \quad (1.11)$$

where $\epsilon = 1 + \chi^{(1)}$ is the dielectric tensor. \mathbf{P}_{nl} acts as a source term in the wave equation. Note, that for crystals with anisotropic dielectric properties $\text{div}\mathbf{E}$ is generally not equal to zero ($\text{div}\mathbf{E} \neq 0$) and hence the wave equation can not be further simplified.

Since the laser beams used in the experiments are monochromatic and most often only one nonlinear process is dominant, it is more convenient to relate the Fourier component of the induced nonlinear polarizability to the one of the present electric fields. The time dependent electric field $\mathbf{E}(\mathbf{r}, t)$ can be written as a superposition of monochromatic electric fields $\mathbf{E}^{\omega_p}(\mathbf{r}, t)$ with distinct frequencies ω_p

$$\mathbf{E}(\mathbf{r}, t) = \frac{1}{2} \sum_p [\mathbf{E}^{\omega_p}(\mathbf{r}) e^{-i\omega_p t} + c.c.]. \quad (\omega_p \neq 0) \quad (1.12)$$

just as well the nonlinear optical polarization

$$\mathbf{P}_{\text{nl}}(\mathbf{r}, t) = \frac{1}{2} \sum_p [\mathbf{P}^{\omega'_p}(\mathbf{r}) e^{-i\omega'_p t} + c.c.], \quad (\omega'_p \neq 0) \quad (1.13)$$

If two monochromatic electric waves with frequency ω_1 and ω_2 are present in the medium, the Fourier component of the polarization is derived by inserting Eq. (1.12) and (1.13) in Eq. (1.10). This leads to a multitude of nonlinear polarizations oscillating with different frequencies. The expansion gives in the case of sum-frequency generation for the selected frequency $\omega_3 = \omega_1 + \omega_2$

$$P_i^{\omega_3}(\mathbf{r}) = \frac{\epsilon_0}{2} \sum_{\sigma(\omega_1^2)} \chi_{ijk}^{(2)}(-\omega_3, \omega_2, \omega_1) E_j^{\omega_2}(\mathbf{r}) E_k^{\omega_1}(\mathbf{r}), \quad (1.14)$$

where σ is the permutation operator of the frequencies. The previous expression can be written in general way by

$$P_i^{\omega_3}(\mathbf{r}) = K^{(2)} \epsilon_0 \chi_{ijk}^{(2)}(-\omega_3, \omega_2, \omega_1) E_j^{\omega_2}(\mathbf{r}) E_k^{\omega_1}(\mathbf{r}), \quad (1.15)$$

where $K^{(2)}$ is a factor that depends on the nonlinear process under consideration. In Table 1.1 the $K^{(2)}$ factors are summarized for possible second-order nonlinear interactions, i.e. second-harmonic generation, sum- and difference-frequency generation, the electro-optic effect, and the process of optical rectification. Note, for the electro-optic effect one of the interacting fields is quasi static, i.e. $\mathbf{E}(\mathbf{r}, t) = \frac{1}{2} [\mathbf{E}^\omega(\mathbf{r}) e^{-i\omega t} + c.c.] + \mathbf{E}_0$, which has to be inserted into Eq. (1.10) to obtain the corresponding $K^{(2)}$ factor. Here, \mathbf{E}_0 is the electric field amplitude of the quasi static field.

Nonlinear process	Description	$\chi^{(2)}$	$K^{(2)}$
second-harmonic generation SHG	input: single beam at ω output: single beam at 2ω	$\chi^{(2)}(-2\omega, \omega, \omega)$	1/2
sum- (difference-) frequency generation	input: beams at ω_1, ω_2 output: beam at $\omega_3 = \omega_1 \pm \omega_2$	$\chi^{(2)}(-\omega_3, \omega_2, \pm\omega_1)$	1
linear electro-optic effect EO	input: static field and ω -beam output: phase shift on ω -beam	$\chi^{(2)}(-\omega, 0, \omega)$	2
optical rectification OR	input: single beam at ω output: static polarization	$\chi^{(2)}(0, -\omega, \omega)$	1/2

Table 1.1: Summary of second-order nonlinear optical processes with corresponding $K^{(2)}$ factors, compare Eq. (1.15).

Dealing with monochromatic waves, the wave equation Eq. (1.11) can be further simplified. If the polarization is oscillating with frequency $\tilde{\omega}$, electro-magnetic waves with the same frequency will be generated. Therefore, we obtain

$$\text{rot}(\text{rot}\mathbf{E}^{\tilde{\omega}}) - \frac{\tilde{\omega}^2}{c^2} \epsilon \mathbf{E}^{\tilde{\omega}} = \mu_0 \tilde{\omega}^2 \mathbf{P}^{\tilde{\omega}}. \quad (1.16)$$

The solution of this wave equation consists of a particular and a homogenous part analogous to the solution of a second-order differential equation. The homogenous solution is often called free wave and the particular the bound wave, since it is connected to the polarization of the material. For the nonlinear process of second-harmonic generation the wave equation was solved for homogenous materials [8,9] as well as for birefringent media [10]. Recently, a solution for a general case was obtained by a 4×4 matrix formalism [11], in analogy to the one used for linear media [12].

1.2 Microscopic and macroscopic properties of organic materials

In the previous section the macroscopic material properties were discussed. To understand the optical effects on the molecular level better, which is of importance for the design of new materials and the optimization of their nonlinearities, the microscopic material properties will be introduced and related to the macroscopic quantities.

In analogy to the Taylor expansion of the macroscopic polarization, the molecular polarization $\mathbf{p}(\mathbf{r}, t)$ is given by [7]

$$p_i(\mathbf{r}, t) = \mu_{g,i} + \epsilon_0 \alpha_{ij}^{(1)} E_j(\mathbf{r}, t) + \epsilon_0 \beta_{ijk}^{(2)} E_j(\mathbf{r}, t) E_k(\mathbf{r}, t) + \dots, \quad (1.17)$$

where $\mu_{g,i}$ is the i -th component of the ground state dipole moment, $\alpha^{(1)}$ the polarization tensor, and $\beta^{(2)}$ the second-order polarizability or first-order hyperpolarizability tensor.

The microscopic and macroscopic material properties can be related to each other by the oriented gas model described in Ref. [13], in which intermolecular contributions to the nonlinearity were neglected and only intramolecular interactions were taken into account. This leads to the relation for $\chi_{ii}^{(1)}$ along the dielectric axis i [6]

$$\chi_{ii}^{(1)}(-\omega, \omega) = N \frac{1}{n(g)} f_i^\omega \sum_s^{n(g)} \sum_{IJ}^3 \cos(\theta_{iI}^s) \cos(\theta_{iJ}^s) \alpha_{IJ}(-\omega, \omega), \quad (1.18)$$

where N is the number of molecules per unit volume, $n(g)$ the number of symmetry equivalent positions in the unit cell, and θ_{iI}^s are the angles between the molecular axis I and the dielectric axis i . f_i^ω is a correction factor, which accounts for that the electric field at the position of the molecule is influenced by its neighbors and hence differs from the externally applied electric field. Most often Lorentz local field factors are used with [14]

$$f_i^\omega = \frac{n_i^2(\omega) + 2}{3}, \quad (1.19)$$

where $n_i(\omega)$ is the refractive index along the dielectric i axis. For a nonlinear optical process

involving three different frequencies the corresponding relation is given by [7]

$$\begin{aligned} \chi_{ijk}^{(2)}(-\omega_3, \omega_2, \omega_1) &= N \frac{1}{n(g)} f_i^{\omega_3} f_j^{\omega_2} f_k^{\omega_1} \\ &\times \sum_s^{n(g)} \sum_{IJK}^3 \cos(\theta_{iI}^s) \cos(\theta_{jJ}^s) \cos(\theta_{kK}^s) \beta_{IJK}^{(2)}(-\omega_3, \omega_2, \omega_1). \end{aligned} \quad (1.20)$$

For molecules with strong nonlinearity along a single charge-transfer axis, it is reasonable to consider only one dominant tensor component β_{zzz} along this axis. Therefore, to attain a big diagonal component of the macroscopic nonlinear susceptibility $\chi^{(2)}$, densely packed molecules with a high nonlinear molecular activity β_{zzz} are required, which are parallel arranged so that the projection factors $\cos(\theta_{jJ}^s)$ are close to unity.

1.3 Nonlinearities of organic molecules and crystals

1.3.1 Molecular dispersion of the nonlinear susceptibility

For second-order nonlinear optical processes, molecules with π -electron ring systems with strong donor (D) and acceptor (A) end groups as shown in Fig. 1.1 are commonly used. The weakly

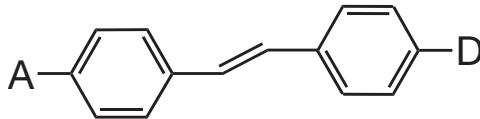


Figure 1.1: Nonlinear active molecule. Nonlinear optically active molecules are often based on relatively weak bounded π electrons combined with strong donor and acceptor end groups.

bound π electrons of the rings and of the conjugated electron bridge between these can move relatively easy towards the acceptor group when an electric field is applied, whereas the motion to the donor group is unfavorable. This results in an asymmetric response upon applying an oscillating field, shown in Fig. 1.2. Hence, such molecules show high second-order activity. In terms of quantum mechanics this circumstance implies that the first excited state has only a small energetic difference to the ground state of the molecule, whereas the second excited state has a much larger energy difference to the ground state. Therefore, the molecules can be considered in a first approximation as a quantum-mechanical two-level system. Taking this assumption, the exact definition of the quantum-mechanical molecular polarization [15] can be simplified for a molecule with a main charge-transfer axis in z direction, which yields in the case of sum-frequency generation to [6, 16]

$$\beta_{zzz}(-\omega_3, \omega_2, \omega_1) = \frac{1}{3} \frac{\omega_{eg}^4 (3\omega_{eg}^2 + \omega_1\omega_2 - \omega_3^2)}{(\omega_{eg}^2 - \omega_1^2)(\omega_{eg}^2 - \omega_2^2)(\omega_{eg}^2 - \omega_3^2)} \beta_0, \quad (1.21)$$

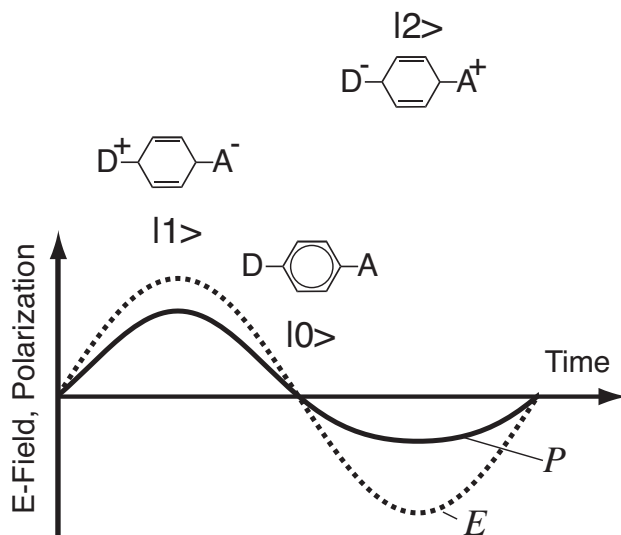


Figure 1.2: Nonlinear polarization. Induced nonlinear polarization P (full curve) as a function of time. The dashed curve represents the electric field E . Shown is as well the quantum-mechanical analogon. In the first excited state $|1\rangle$ the electron is transferred from the donor to the acceptor group. In the ground state $|0\rangle$ the π electrons of the aromatic ring are delocalized. The transition to the $|2\rangle$ excited state, for which the electrons are moved to the donor group, is unfavorable.

where ω_{eg} is the resonance frequency of the transition and β_0 the hyperpolarizability at zero frequency, which is given by

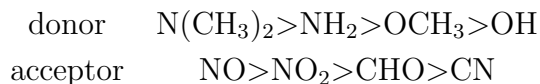
$$\beta_0 = \frac{3}{2\epsilon_0\hbar^2} \frac{\Delta\mu\mu_{eg}^2}{\omega_{eg}^2}, \quad (1.22)$$

where $\Delta\mu = \mu_e - \mu_g$ is the difference between the ground state and excited state dipole moment and μ_{eg} denotes the transition dipole moment. Inserting the frequency dependent relation for β into Eq. (1.20) leads to the dispersion relation of the nonlinear susceptibility $\chi^{(2)}$.

1.3.2 Optimization of the second-order activity

To optimize the microscopic second-order optical activity, various investigations have been made to achieve a proper design of the molecules. [6,7]. Here, a summary of the most important results is given:

- Effect of the donor and acceptor groups: β is dependent on the donor and acceptor strength of the end groups used. In the following a list of commonly used end groups ranked after their strength is given:



- Effect of the conjugation length: The molecular hyperpolarizability is proportional to the conjugation length of the π -electron system between the donor and acceptor group to the third power, i.e. $\beta \propto L_\pi^3$. Note: Long molecules exhibit generally a higher nonlinearity than short ones, but occupy a bigger volume in crystals and poled polymers. Therefore, the quantity of interest is the activity per volume.
- Effect of planarity: The planarity of the molecules is an important aspect since the mobility of the π -electron system can be lowered if the molecule is twisted or bent.

The fabrication of crystals with molecules of high nonlinear activity is still very challenging. One of the reasons is that molecules with high first-order hyperpolarizability have also large ground state dipole moments and therefore often tend to arrange antiparallel to each other, which results in a centrosymmetric packing and therefore no macroscopic second-order activity $\chi^{(2)} = 0$. One possibility to overcome this problem is based on using ionic type of molecules. The cation of the organic salt has normally a high second-order activity and the anion is used to achieve a noncentrosymmetric crystal packing by strong Coulomb interactions. Furthermore, the anion acts as a spacer in order to reduce the interactions between the nonlinear active molecules. More details are given in Chapter 2 and 7.

1.4 The electro-optic effect in organic materials

The electro-optic effect is commonly described by considering field-induced changes of the optical indicatrix and is given by [17]

$$\Delta \left(\frac{1}{n^2} \right)_{ij} = r_{ijk} E_k + R_{ijkl} E_k E_l, \quad (1.23)$$

where r_{ijk} is the linear and R_{ijkl} the quadratic electro-optic coefficient. Whereas the linear electro-optic effect or Pockels effect occurs only in noncentrosymmetric materials, the quadratic electro-optic effect or Kerr effect is present in all materials.

In inorganic centrosymmetric crystals the optical Kerr effect plays an important role near phase transitions [18], since $\chi^{(3)}$, which is related to \mathbf{R} , is largely enhanced close to the Curie point. On the other hand, in organic crystals it is of minor importance. Hence we focus on the discussion of the linear electro-optic effect.

In the linear approximation the induced refractive index change Δn_i is approximately given by [17]

$$\Delta n_i = -\frac{n_i^3 r_{iik} E_k}{2}. \quad (1.24)$$

To attain large refractive index changes, the quantity $n_i^3 r_{iik}$, which is defined as figure of merit for electro-optic amplitude modulators, has to be maximized.

1.5 Frequency dependence of the linear and nonlinear optical properties

The electro-optic coefficient is frequency dependent. It has electronic (r^e), infrared vibrational (r^o), and acoustic phonon (r^a) contributions and hence can be written as [6]

$$r^T = r^a + \underbrace{r^o + r^e}_{r^s}, \quad (1.25)$$

where r^s is defined as the clamped electro-optic coefficient.

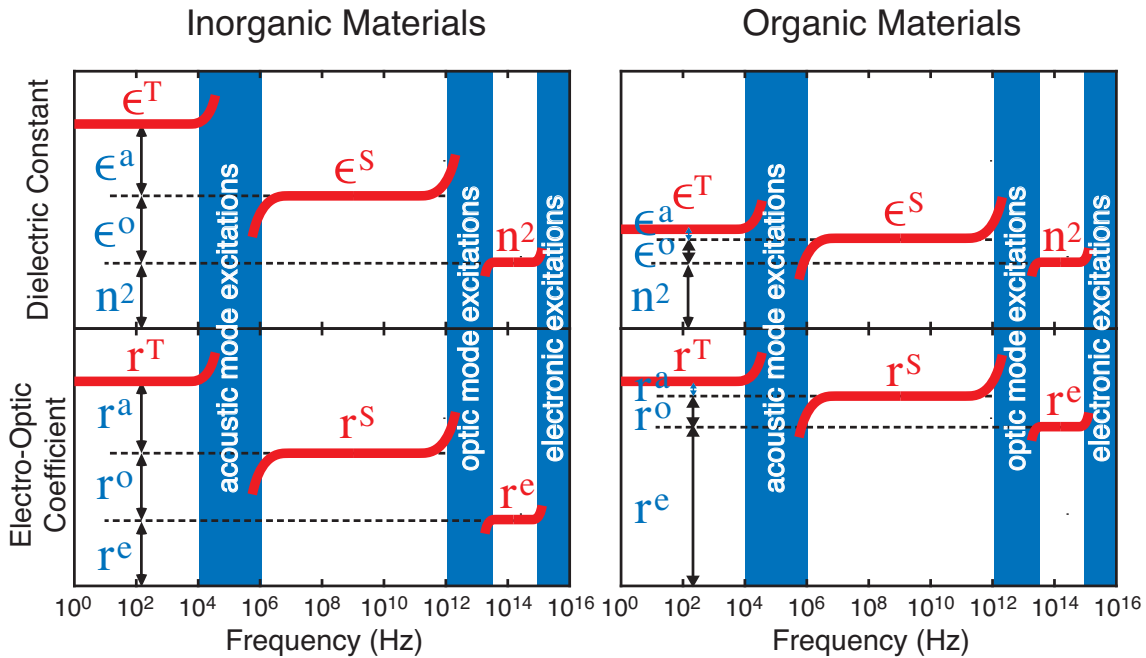


Figure 1.3: Frequency dependence for inorganics and organics. Schematic of the material linear and of the nonlinear optical response as a function of the frequency of the electric field.

The polarizability and hence the dielectric constant as well as the electro-optic activity in crystals have mainly two contributions stemming from the orderly packed molecules or atoms and interactions between them. In organic materials the nonlinearity is mainly determined by the polarizability of the molecules, which arises from the π electrons between the donor and acceptor group and corresponds to frequencies of $10^{15} - 10^{16}$ Hz. Intermolecular interactions are of minor importance. Hence, optical phonons give a small contribution to the electro-optic effect and lattice vibrations play a minor role [19]. Therefore, the electro-optic effect in organic materials is almost dispersion free and of electronic origin. On the other hand in inorganic materials, which are based on a strong bonding between the lattice components (ions), lattice vibrations play a dominant role (at low frequencies), since the ions act as additional polarizable

	ϵ^T	n^2	r^T [pm/V]	r^S [pm/V]	r^e [pm/V]	d [pm/V]
LiNbO ₃	28	4.5	30	30	5.8	34
KNbO ₃	44	4.5	63	34	3.7	21
DAST	5.2	4.6	47	48	36	290

Table 1.2: Comparison of the inorganic crystals LiNbO₃ and KNbO₃, and the organic crystal DAST with respect to the unclamped dielectric constant ϵ^T , refractive index n , unclamped r^T , clamped r^S , and electronic r^e electro-optic coefficients, and nonlinear optical coefficient d . The values for LiNbO₃ and KNbO₃ are given at 1.06 μm , and for DAST at 1.5 μm .

elements. Figure 1.3 shows a schematic drawing of the different contributions to the linear and nonlinear optical polarizability characteristics in inorganic and organic materials. As an example and for comparison the different contributions of some widely used inorganic and organic crystals are listed in Table 1.2.

The electronic contribution of the electro-optic effect in organic materials can be related to the nonlinear susceptibility and is given by [6]

$$r_{ijk}^e = \frac{-2}{n_i^2 n_j^2} \chi_{ijk}^{(2)}(-\omega, 0, \omega), \quad (1.26)$$

where $\chi^{(2)}(-\omega, 0, \omega)$ can be expressed by the dispersion relation of the microscopic first-order hyperpolarizability with help of Eq. (1.20).

1.6 High-speed modulation

To transmit high data rates per channel, high-speed modulators are key components in optical networks. During last decades a lot of effort has been put on increasing the modulation bandwidth by optimizing the performance of traveling-wave modulators. In this section a short theoretical description of the most important physical aspects of a traveling-wave modulator are given followed by an overview on contemporary polymer and LiNbO₃ modulators.

1.6.1 Traveling-wave Mach-Zehnder modulator

The traveling-wave modulators have attracted lots of attention, because larger modulation bandwidth are achievable than would otherwise be allowed by electrical capacitive effects and transit-time limitations [20, 21].

In Fig. 1.4 a configuration of a Mach-Zehnder traveling-wave modulator is shown. The optical wave and the electric modulation field overlap over an interaction length L . Assuming that the optical field is polarized along the x direction and that the electric modulation field

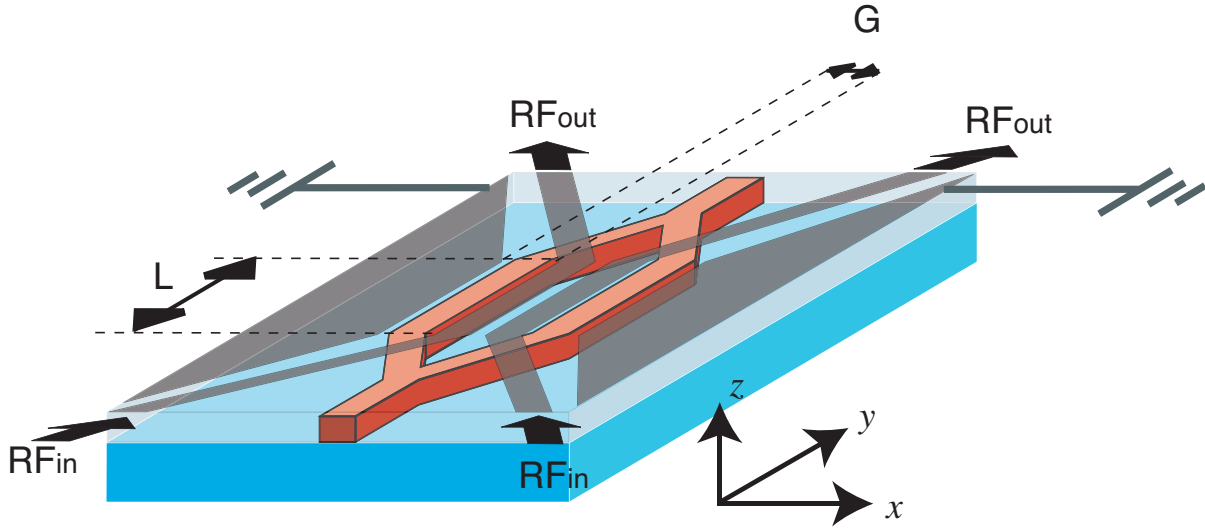


Figure 1.4: traveling-wave modulator. Schematic drawing of a traveling-wave modulator. The optical field is TE polarized and the modulation field is applied along x -direction. Therefore, the in-plane component of the electro-optic tensor r_{xxx} is causing the refractive index change, which has opposite signs in the two arms of the Mach-Zehnder Modulator.

is applied along the same direction, the refractive index and electro-optic coefficient of interest are n_x and r_{xxx} , respectively. For reason of simplicity we omit the index x further on. For the fundamental understanding of the modulator it is sufficient to consider the response to a sinusoidal driving voltage. Furthermore, we assume that the impedances of the driving source and the terminator are matched.

An optical wave traveling a distance dy in one arm of the Mach-Zehnder modulator will experience in presence of a modulation field an additional phase shifted $d\phi$ of

$$d\phi = k_o \Delta n(y, t) dy, \quad (1.27)$$

where k_o is the wave vector of the optical light wave. $\Delta n(y, t)$ is the electro-optically induced refractive index change and can be related to the modulator dimensions with help of Eq. (1.24)

$$\Delta n(y, t) = -\frac{n^3 r}{2} E_{av}(y, t) = -\frac{n^3 r}{2} \Gamma \frac{V(y, t)}{G}, \quad (1.28)$$

where E_{av} is the averaged electric field in the material, $V(y, t)$ the applied voltage to the electrodes and G the gap between the electrodes. Γ is a factor which accounts for the spatial overlap of the optical intensity profile and the applied electric field and is given by [22]

$$\Gamma = \frac{G}{V_0} \frac{\int \int E_o^2(x, z) E_m(x, z) dx dz}{\int \int E_o^2(x, z) dx dz}, \quad (1.29)$$

where E_o is the optical field and E_m the field strength of the microwave modulation field in the material and V_0 the amplitude of the applied voltage. The integral should only encompass over the electro-optic active area ($r \neq 0$) of one arm.

One important characteristic of a modulator is its half-wave voltage, which is defined as the dc voltage that has to be applied in order to achieve a phase shift of π between the two optical waves in the arms, and hence no light is transmitted. The phase shift between the two arms in presence of a dc field is given by

$$\Delta\phi = k_o n^3 r \Gamma \frac{L}{G} V_{\text{DC}}. \quad (1.30)$$

For the half-wave voltage V_π we obtain

$$V_\pi = \frac{\lambda G}{2n^3 r \Gamma L}, \quad (1.31)$$

where λ is the wavelength in vacuum of the optical field. Half-wave voltages below one volt are desirable and the aim of future devices. To attain low driving voltages, a high electro-optic figure of merit and a large overlap between optical and modulation field are beneficial. The half-wave voltage is also dropping if the interaction length is increased, nevertheless L should be kept as short as possible in order to attain a large modulation bandwidth of the device.

In presence of a microwave modulation field, which is oscillating at frequency $\Omega = 2\pi\nu$, the voltage that a photon experiences at the position y while traversing the modulator is given by [23]

$$V(y, t) = V_0 e^{i(\eta y - \Omega t)}, \quad (1.32)$$

where $\eta = \beta_e - (\Omega/\omega_o)\beta_o$ is a function of the electrical β_e and optical β_o propagation constant with $\omega_o = ck_o$ the angular frequency of the optical field. The total phase shift between the optical waves in the two arms is obtained by integrating Eq. (1.27) over y and is given by

$$\Delta\phi(t) = \frac{V_0}{V_\pi} e^{i\Omega t} \underbrace{\frac{-i}{\eta L} (e^{i\eta L} - 1)}_{F(\Omega)}, \quad (1.33)$$

where $F(\Omega)$ represents the modulator complex filter function. The propagation constant of the microwave may be written as $\beta_e = N_e k_e + i\alpha_e$, where N_e represents the real part of the microwave index and k_e the wave vector of the microwave. α_e is the attenuation constant of the microwave. Normally, the losses of the waveguides are relatively low, therefore the imaginary part of the optical waveguide propagation constant can be neglected ($\beta_o = n_{\text{eff}} k_o$). The modulator frequency response $M(\nu)$ is then given by

$$M(\nu) = FF^* = \frac{e^{-\alpha_e L} \sin^2(\frac{\gamma L}{2}) + \frac{1}{4}(1 - e^{-\alpha_e L})^2}{(\frac{\gamma L}{2})^2 + (\frac{\alpha_e L}{2})^2}, \quad (1.34)$$

where $\gamma = 2\pi\nu(N_e - n_{\text{eff}})/c$ is the walk-off constant between the optical wave and the microwave. The microwave power attenuation mainly depends on the electrode material and their geometry. A detailed study on this topic is given in Refs. [23, 24]. In absence of microwave attenuation Eq. (1.34) simplifies and can be written as

$$M(\nu) = FF^* = \text{sinc}^2\left(\frac{\gamma L}{2}\right), \quad (1.35)$$

which is only dependent on the walk-off constant and the interaction length. The 3-dB optical bandwidth of the modulator corresponds to the frequency at which $\sqrt{|M(\nu)|}$ (or the modulation amplitude of the light intensity) is reduced by a factor of 2 compared with the zero-frequency response [25].¹ In absence of microwave attenuation it is given by

$$\nu_{3\text{dB}_o} \approx 0.6 \frac{c}{N_e - n_{\text{eff}}} \frac{1}{L}. \quad (1.36)$$

In order to attain large modulation bandwidth and hence high bit transmission rates per second, either the velocities of the optical and the microwave have to be matched or the interaction length L has to be chosen as small as possible, which results in a higher driving voltage in order to attain a sufficient phase shift, compare also Eq. (1.31).

The **goals** for future modulators are the following

- modulation voltage < 1 V
- large modulation bandwidth (bigger than 100 > GHz).

To attain these aims, following **design aspects** have to be considered

- **L** small: To attain large modulation bandwidth, the interaction length needs to be as small as possible, since even though velocity matching between the optical and microwave can be achieved, the microwave attenuation places an important role.
- **rn³** and **Γ** big, **G** small. The electro-optic figure of merit and the overlap integral have to be maximized, and the electrode spacing minimized in order to keep the half-wave voltage low.

1.6.2 Polymer and LiNbO₃ Mach-Zehnder modulators

Polymeric devices as well as organic crystal have generally higher and faster nonlinearities compared to the inorganic standard lithium niobate. The quantity of importance for electro-optic applications is the figure of merit $FM = n^3 r$, which also depends on the refractive index. In Table 1.3 the figure of merit of poled electro-optic polymers, the organic crystal DAST, and the widely used LiNbO₃ are given. DAST has a figure of merit that is by one third bigger than the one of LiNbO₃ and comparable to the one of polymers. Furthermore, DAST is chemically stable to about 250°C, whereas the presented poled electro-optic polymers tend to relax around their glass transition temperature which is below 150°C for the presented devices.

In addition, organic materials are also advantageous since the overlap integral is generally higher than in LiNbO₃ [30]. The reason is the relatively large dielectric constant $\epsilon_{33} = 28$ of LiNbO₃. Therefore, even though the buffer layer, which is put between waveguide and the

¹Note that in the field of electrical communication, the bandwidth of a linear system is differently defined as the frequency at which electrical power $\propto M(\nu)$ drops by 3 dB ($M(\nu) = 0.5$).

Material	r [pm/V]	n	FM[pm/V]	Reference
CLD1+PMMA ($T_g=65^\circ\text{C}$)	58	1.54	210	[26]
AJC146+PMMA ($T_g\approx 140^\circ\text{C}$)	170	≈ 1.54	620	[27]
DAST	47	2.13	450	[28]
LiNbO ₃	31	2.14	300	[29]

Table 1.3: Electro-optic coefficient r_{333} except for DAST r_{111} , refractive index and electro-optic Figure of Merit of poled polymers, DAST and LiNbO₃ at a wavelength of $\lambda = 1.55 \mu\text{m}$, except for the polymer CLD1 at $\lambda = 1.32 \mu\text{m}$.

electrodes, is thin, a big portion of the applied voltage drops over it. For organic materials the buffer layer has normally almost the same dielectric constants, which results in a much lower voltage drop over the buffer layer. Furthermore, organic materials have a very low dispersion of the dielectric constant compared to lithium niobate, thus velocity matching between the optical and microwave is easier to realize.

Recently there have been demonstrations of electro-optic modulation with half-wave voltages below 1 V and bandwidths of over 100 GHz in organic devices, showing their future potential. In a polymeric Mach-Zehnder modulator with an arm length of 3 cm half-wave voltages of less than 1 V were reported [26]. In other polymeric modulator structures bandwidth of over 150 GHz were demonstrated [30], but due to a low electro-optic activity, the half-wave voltage was 11 V for an interaction length of 2 cm. These recent demonstrations show the potential of organic materials in future high-speed modulators, since for lithium niobate there are strong doubts about its usefulness above 100 GHz [30].

1.7 Microring resonators for electro-optic modulation

Microring resonators are photonic structures, which confine light resonantly. Commonly, they consist of a straight waveguide and a ring. Coupling between the two components is realized by bringing them in close proximity. Microrings are very attractive for the incorporation in modern telecommunication devices because of their small size (micrometers compared to millimeters of Mach-Zehnder modulators) allowing for very large scale integration (VLSI). Their strong wavelength sensitivity makes them well suited for filtering and processing of optical signals. Because of these favorable properties a lot of research effort has been put on the investigation and fabrication of microring devices during the last decade.

Ring resonators made of electro-optic active materials are of special interest, since the optical ring length can be altered by the electro-optic effect and thus the resonance wavelength tuned. Active microring resonators can be therefore used as switchable wavelength filters,

and also as electro-optic modulators. Active microring devices have been demonstrated up to now in inorganic crystals, e.g. LiNbO_3 [31, 32], and electro-optic poled polymer devices [33–35]. Electrical modulation based on carrier injection has also been demonstrated in silicon microrings [36, 37].

In this section, a brief introduction to the topic of microring resonators is given. For a detailed description we refer to standard textbooks [38,39]. In the second part the application of microrings as electro-optic modulators is studied. Their performance with respect to switching voltage and bandwidth is described and compared to those of Mach-Zehnder modulators.

1.7.1 Basic principle of microring resonators

A microring structure consists commonly of a straight waveguide and a ring. The two components are brought in close contact so that their evanescent fields overlap and thus coupling between them is achieved. A schematic drawing of a microring resonator is shown in Fig. 1.5(a). If the optical ring length L is a multiple of the optical wavelength, then the field in the ring is adding up constructively and therefore a dip in the transmission curve is observed. The resonator behavior of a microring resonator is similar to the one of a Fabry Perot resonator, where the feedback is achieved by back reflection instead of coupling. Hence, the transmission

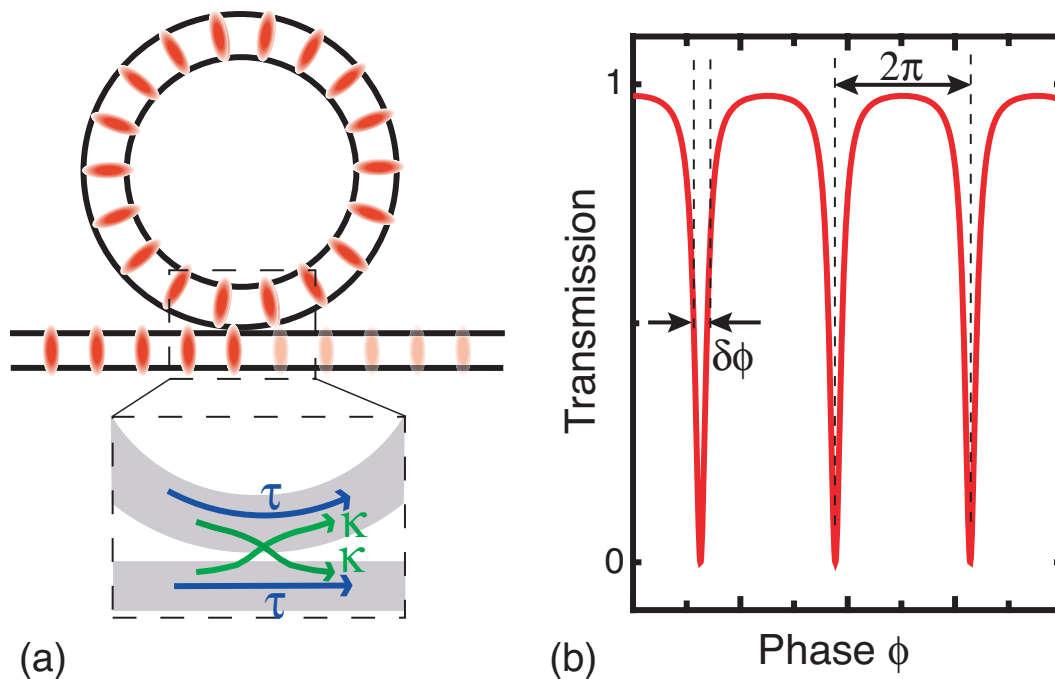


Figure 1.5: Microring modulator. (a) Schematic drawing of a microring resonator. The coupling region is shown enlarged. κ and τ are the electric field coupling and transmission coefficients, respectively. (b) Transmission as a function of the ring round trip phase delay ϕ .

as a function of the round trip phase delay $\phi = k_0 n_{\text{eff}} L$, which is depicted in Fig. 1.5(b), shows similar features. Note, that the effective index n_{eff} for single mode waveguides is strongly dependent on the waveguide dimension and therefore can considerably differ from the bulk refractive index.

The important quantities, which describe a Fabry Perot resonator as well as a microring resonator, are the resonator losses and the strength of the feedback. In a microring resonator the losses stem mainly from radiation to the substrate and cladding, because of the bend shape of the waveguide structures. The decay constant of the field inside the cavity after one round trip is given by $\sigma = e^{-\frac{\alpha}{2}L}$ with $\alpha = \frac{4\pi}{\lambda}\text{Im}(n_{\text{eff}})$. The coupling between the optical field in the port waveguide and in the ring can be described by the field amplitude transmission τ and coupling constants κ . In case of lossless coupling the total energy is conserved and therefore $|\tau|^2 + |\kappa|^2 = 1$. The transmission of a microring is given by [31, 39, 40]

$$T(\phi) = \left| \frac{E_{\text{out}}}{E_{\text{in}}} \right|^2 = \frac{(\sigma - \tau)^2 + 4\sigma\tau \sin^2(\phi/2)}{(1 - \sigma\tau)^2 + 4\sigma\tau \sin^2(\phi/2)}. \quad (1.37)$$

In case of critical coupling conditions, i.e. $\tau = \sigma \approx 1$, the extinction ratio is maximal at resonance

$$\phi = k_0 L \text{Re}(n_{\text{eff}}) = m2\pi, \quad (1.38)$$

where m is an integer. In analogy to a Fabry Perot resonator, the transmission of a microring as a function of the round trip phase delay ϕ can be written as

$$T(\phi) = 1 - \frac{T_R}{(1 + \frac{4F^2}{\pi^2} \sin^2(\phi/2))}, \quad (1.39)$$

where $T_R = (1 - \sigma^2)(1 - \tau^2)/(1 - \sigma\tau)^2$ is the maximal transmission reduction of a microring achievable under resonance conditions and $F = \pi\sqrt{\sigma\tau}/(1 - \sigma\tau)$ is defined as the finesse F . The finesse relates the free spectral range to the resonance linewidth, which is defined as full width half max $\delta\phi$,

$$F \approx \frac{2\pi}{\delta\phi}. \quad (1.40)$$

Some important relations for microring resonators are summarized in the following:

- The **free spectral range** $\Delta\lambda_{\text{FSR}}$, which is an important quantity of a microring resonator, is defined as the spacing between two adjacent resonance wavelengths

$$\Delta\lambda_{\text{FSR}} \approx \frac{\lambda^2}{Ln_{\text{eff,g}}}, \quad (1.41)$$

where $n_{\text{eff,g}} = n_{\text{eff}} - \lambda \frac{\partial n_{\text{eff}}}{\partial \lambda}$ is the group effective index.

- Expressed in terms of wavelength instead of phase, the **finesse** \mathbf{F} is given by

$$F = \frac{\Delta\lambda_{\text{FSR}}}{\delta\lambda_{\text{FWHM}}}, \quad (1.42)$$

where $\delta\lambda_{\text{FWHM}}$ is the spectral width of the resonance peak (full width half max).

- The **quality** of a cavity is often described by the **Q** factor of a resonator, which is proportional to the ratio of stored energy in the cavity divided by the loss per roundtrip

$$Q = \frac{\lambda}{\delta\lambda_{\text{FWHM}}}. \quad (1.43)$$

- The photon lifetime of an unloaded micro ring resonator (absence of a straight waveguide and therefore no coupling losses) is defined as

$$\tau_p = \frac{n_{\text{eff,g}}}{\alpha c}. \quad (1.44)$$

In case of weak and critical coupling $\sigma = \tau \approx 1$, the quantities introduced can be related to the basic ring quantities $L, \alpha, n_{\text{eff}}$ and we obtain

$$F = \frac{\pi}{\alpha L} \quad \text{and} \quad Q = \frac{\pi n_{\text{eff,g}}}{\alpha \lambda} = \pi \frac{\tau_p}{T}, \quad (1.45)$$

where $T = 1/\nu$ is the optical field period. The optical properties of a microring are therefore defined by the optical radiation loss, the ring circumference, and the effective index. A detailed study of the important topic of bending losses in dependence on the ring radius as well as on the index contrast between waveguide core and substrate/cladding are given in Ref. [31].

1.7.2 Electro-optic modulation using microring resonators

The tuning of the resonance wavelength of a microring resonance offers several very interesting potential applications, such as switching between different channels for dense wavelength division multiplexing in modern telecommunication systems or modulation of the transmitted intensity. Since for these applications fast switching is required, electro-optic active rings, particularly those made of organic materials, are of great interest. Via the electro-optic effect, the effective index of the ring is changed and as a result the optical field experiences an additional phase delay after a round trip given by

$$\Delta\phi = k_0 \Delta n_{\text{eff}} L = \frac{\pi}{\lambda} n^3 r \frac{\partial n_{\text{eff}}}{\partial n} \frac{L}{G} V, \quad (1.46)$$

where G is the distance between the electrodes, assumed that the modulation field is homogeneous. Figure 1.6(b) shows the transmission of a microring as a function of the applied voltage. Indicated is as well a sinusoidal modulation voltage which results in a modulation in the transmitted intensity.

1.7.3 Comparison between Mach-Zehnder and microring resonators

Mach-Zehnder modulators are commonly used for electro-optic modulation and are commercially available with transmission rates of 40 Gb/s. On the other hand microrings have attracted

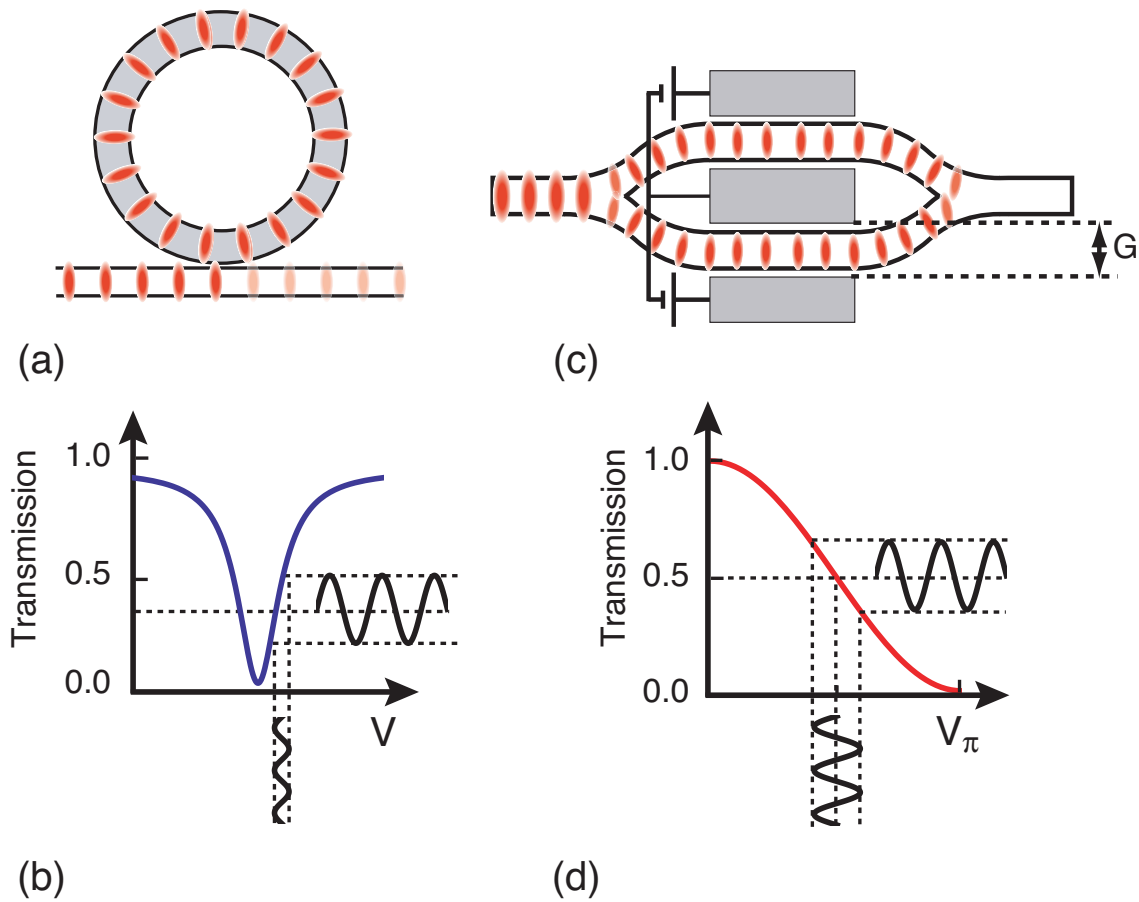


Figure 1.6: Microring and Mach-Zehnder modulator. Schematic drawings of a microring and a Mach-Zehnder modulator are shown in (a) and (c), respectively. The corresponding transmission curves in dependence on the applied voltage are depicted in (b) and (d). Indicated is as well the change in transmission induced by applying a sinusoidal modulation voltage.

		Microring	Mach-Zehnder
Transmission	$T(\Delta\phi) =$	$1 - \frac{T_R}{1 + \frac{4F^2}{\pi^2} \sin^2(\Delta\phi/2)}$	$\cos^2(\Delta\phi/2)$
Phase delay	$\Delta\phi =$	$\frac{\pi}{\lambda} n^3 r \frac{\partial n_{\text{eff}}}{\partial n} \frac{L}{G} V$	$2 \frac{\pi}{\lambda} n^3 r \frac{\partial n_{\text{eff}}}{\partial n} \frac{L}{G} V$
Maximal slope	$\left \frac{dT}{d\Delta\phi} \right _{\text{max}} =$	$\frac{3\sqrt{3}}{8} T_R \frac{F}{\pi} \approx \frac{F}{5}$	$\frac{1}{2}$
Working point	$\phi_p =$	$\frac{1}{\sqrt{3}} \frac{\pi}{F}$	$\frac{\pi}{2}$
Half-wave voltage	$V_\pi^{\text{eq}} =$	$\left \frac{dT}{d\Delta\phi} \right _{\text{max}}^{-1} \frac{\lambda G}{2n^3 r L} \frac{\partial n}{\partial n_{\text{eff}}}$	$\frac{\lambda G}{2n^3 r L} \frac{\partial n}{\partial n_{\text{eff}}}$
Optical bandwidth	$f_{3\text{dB}}^{\text{opt}} =$	$\frac{1}{2F} \frac{c}{n_{\text{eff}} L}$	$\frac{3.8}{2\pi} \frac{c}{n_{\text{eff}} L}$
Figure of merit	$f_{3\text{dB}}^{\text{opt}}/V_\pi =$	$0.65 \frac{cn^2 r}{\pi \lambda G} \frac{\partial n_{\text{eff}}}{\partial n}$	$3.8 \frac{cn^2 r}{\pi \lambda G} \frac{\partial n_{\text{eff}}}{\partial n}$

Table 1.4: Main modulator parameters of a microring resonator and a Mach-Zehnder modulator [40].

a lot of attention during the last year due to their interesting transmission characteristics, nevertheless active tunable microrings are not yet commercially available and have been only demonstrated by a few research groups till now. A ring and a Mach-Zehnder modulator with the corresponding transmission curves as a function of the applied voltage are shown in Fig. 1.6. In order to compare both types of structures with respect to electro-optic amplitude modulation, the most important modulator properties are listed in Table 1.4 and will be discussed in the following.

- Maximal slope and working point:** Large signal switching by low voltage modulation is possible by setting the working point, where the slope of the transmission curve is the largest. The maximal slope dT/dV of the transmission curve of a Mach-Zehnder modulator is the largest at 50% transmission. For microring modulators in case of weak and critical coupling a finesse of about $F = 5$ is required, in order to have the same response in dependence on the applied voltage. Both, the working point as well as the maximal slope are dependent on the finesse of the microring resonator. Microring resonators with finesses above five are therefore advantageous to Mach-Zehnder modulators with respect to their sensitivity to the applied field.
- Half-wave voltage:** Since for a microring resonator a half-wave voltage in common sense does not exist, an equivalent half-wave voltage $V_\pi^{\text{eq}} = \pi/2(|dT/dV|_{\text{max}})^{-1}$ is defined in analogy to the one of a Mach-Zehnder modulator. As well for the half-wave voltage a

finesse larger than five is required in order to have a better device performance compared to Mach-Zehnder modulators.

- **Optical bandwidth:** The expressions of the optical bandwidth for the microring and the Mach-Zehnder modulator are given considering only transit time effects. By comparing the two relations for the optical bandwidth given in Table 1.4, we see that that for finesses above five the optical bandwidth is smaller compared with the one of Mach-Zehnder modulators. Note, that the optical modulation bandwidth of Mach-Zehnder modulators can even be considerably increased by using a traveling-wave geometry as shown in the previous section.
- **Bandwidth/Voltage ratio:** Due to a tradeoff between bandwidth and voltage for microring resonators, the ratio bandwidth/voltage is for high-frequency modulation a more useful figure of merit for the device characterization. The value of the Mach-Zehnder modulator is almost by a factor 6 higher compared the one of ring modulators.

In conclusion, microring modulators require lower driving voltages as compared to Mach-Zehnder modulators. They can also be integrated on much smaller chips giving a high packing density. Nevertheless, this improved modulation performance can only be realized by sacrificing their modulation bandwidth, which is limited by the resonator line width. Traveling-wave microring modulators, which have not been discussed here, show a high modulation efficiency at frequencies around multiples of the free spectral range. So far modulation at 111 GHz with a bandwidth of about 5 GHz has been demonstrated [35]. Microring resonators are therefore well suited for applications for which an enhanced modulation response within a finite bandwidth of typically a few gigahertz is required. Mach-Zehnder modulators on the other hand are advantageous for applications with more stringent bandwidth requirements.

1.8 Conclusion

The organic crystal DAST is an interesting alternative to the inorganic material LiNbO_3 as modulator material in microring and Mach-Zehnder modulators. It offers a higher electro-optic activity combined with a low dispersion of the dielectric constant. Therefore, velocity matching between the optical wave and the modulation field can be achieved. Consequently, electro-optic modulators with a bandwidth of over 100 GHz combined with a low driving voltage below 1 V should be feasible with a proper modulator design. In contrast to poled electro-optic polymers DAST has a superior photochemical and thermal stability. Therefore, DAST is ideally suited for high-speed modulators provided that a reliable and fast waveguide structuring technique is available.

Chapter 2

Material properties of the organic crystal DAST

The crystalline material 4-N, N-dimethylamino-4'-N'-methyl-stilbazolium tosylate (DAST) was reported by Marder et al. for the first time [41]. Since then it has attracted lots of attention because of its high nonlinear optical coefficients, e.g. $d_{111} = \frac{1}{2}\chi_{111}(-2\omega, \omega, \omega) = 1010 \pm 110$ pm/V at a wavelength of 1318 nm [42], and the combination of a low dielectric constant $\epsilon_{11} = 5.2 \pm 0.4$ with relatively large electro-optic coefficients; $r_{111} = 77 \pm 8$ pm/V at a wavelength of 800 nm and $r_{111} = 47 \pm 8$ pm/V at $1.54 \mu\text{m}$ [28]. In this chapter we give a brief summary of the most important structural as well as linear and nonlinear optical material properties of DAST and show its applicability for the efficient generation of THz radiation by the nonlinear optical process of rectification and for high-speed electro-optic applications.

2.1 Crystal structure

DAST is an organic salt which consists of a positively charged stilbazolium cation and a negatively charged tosylate anion shown in Fig. 2.1. The crystal packing is achieved by strong Coulomb interactions between the two charged molecules. The cation stilbazolium is a highly nonlinear optically active chromophore, whereas the counter ion tosylate is used to promote a noncentrosymmetric crystallization.

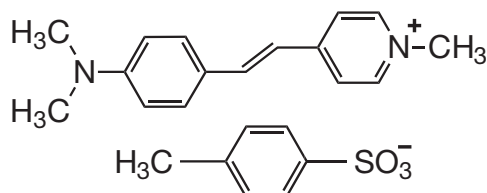


Figure 2.1: Molecular units of DAST. The positively charged, nonlinear optically active chromophore stilbazolium and the negatively charged tosylate.

Depending on the growth conditions, DAST can crystallize in either of two phases, in a centrosymmetric phase (space group $\bar{P}1$, point group $\bar{1}$, $z = 2$) containing water (orange color) [43], or in the monoclinic space group Cc (point group m , $z = 4$) with a red color [44]. The structure of the nonlinear optical active, noncentrosymmetric phase is shown in Fig. 2.2. DAST crystals show consecutive layers of stilbazolium and tosylate molecules. The lattice parameters are $a = 10.365 \text{ \AA}$, $b = 11.322 \text{ \AA}$, and $c = 17.893 \text{ \AA}$ [44].

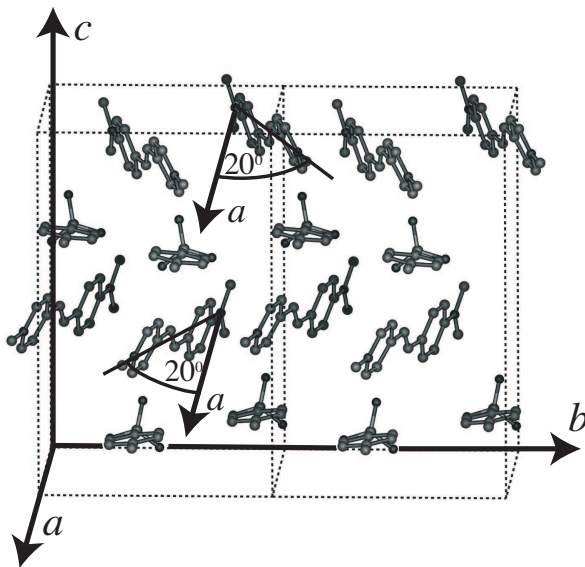


Figure 2.2: Crystal structure of DAST. Two unit cells of the DAST crystal are shown, as obtained from X-ray diffraction experiments. For clarity the hydrogen atoms are not shown. The molecular charge-transfer axis of the nonlinear optically active chromophore makes an angle of 20° to the polar a axis the crystal.

There is a slight difference between the crystallographic and the dielectric axes, as shown in Fig. 2.3. The crystallographic b axis and the dielectric x_2 axis are normal to the mirror plane. The crystallographic a axis makes an angle of $\beta = 92.2^\circ$ with the crystallographic c axis. The angles between the dielectric principal axes and the crystallographic axes a and c were determined by conoscopy and are 5.4° and 3.2° , respectively [45]. The polar axis of the crystal is along x_1 .

2.2 Growth of single crystals

DAST single crystals are grown in our laboratory from a DAST-methanol solution through controlled temperature lowering [44, 46]. A small seed crystal is placed in a growth apparatus which contains slightly supersaturated solution as shown in Fig. 2.4. Therefore, special care is taken for an accurate temperature stability of $\pm 0.002^\circ\text{C}$. The growth is started at 45°C with a ramp of $0.1^\circ\text{C}/\text{day}$. Typically a 1 cm^3 high optical quality bulk is obtained within two months.

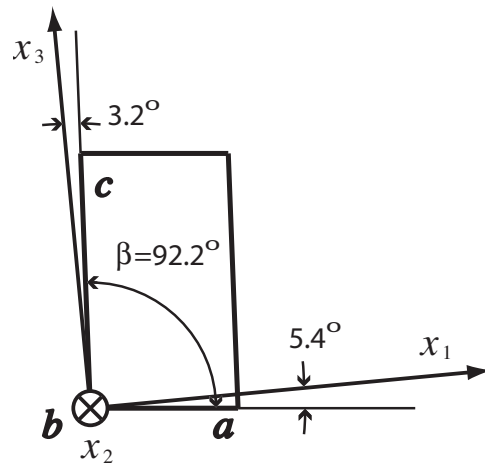


Figure 2.3: Orientation of the crystallographic and dielectric axes. Arrangement of the crystallographic a , b , c axes and the dielectric x_1 , x_2 , x_3 axes in DAST. The mirror plane is perpendicular to the crystallographic b axis.

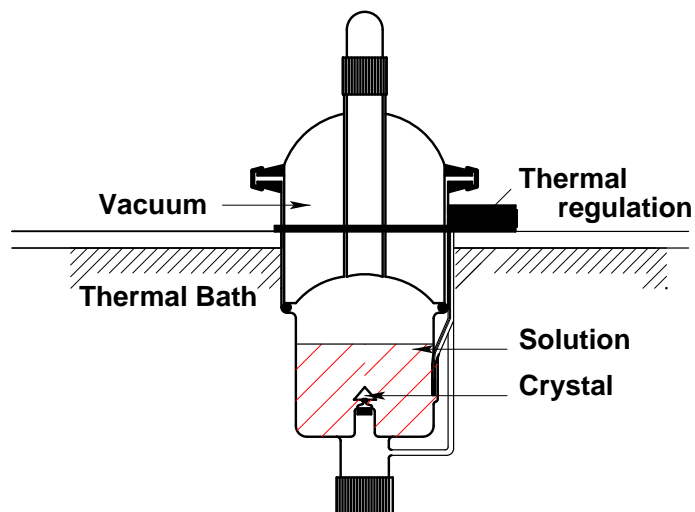


Figure 2.4: Crystal growth of DAST. Growth vessel for bulk growth in a seeded saturated methanol solution.

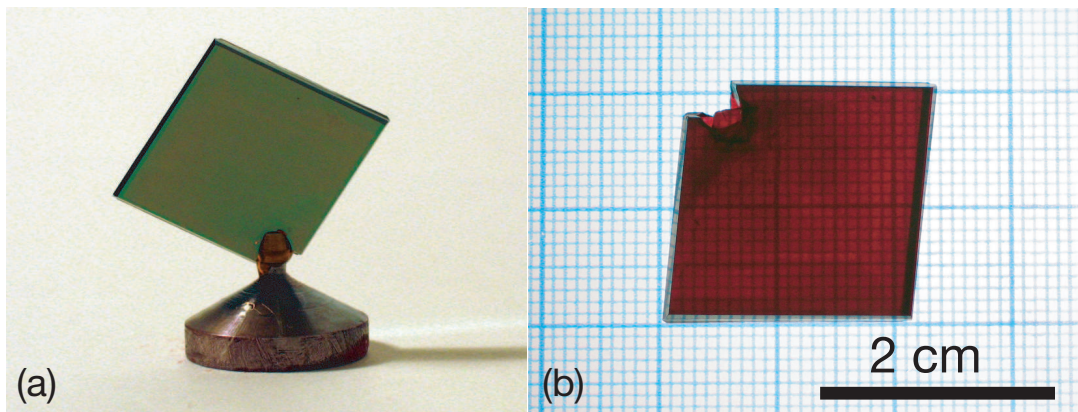


Figure 2.5: DAST crystal. (a) A photograph of a 4 cm^2 wide DAST crystal mounted on a growth holder. In back reflection the crystal looks green due to the strong material absorption in the visible wavelength range, whereas in transmission DAST crystals appear in red (b).

2.3 Thin film growth

Much effort has been devoted to DAST thin film growth lately. As an example, 2D-organic crystal growth using a melt shear or a solution shear method attracted much attention [47–49]. These methods lead to about $3\ \mu\text{m}$ thin and $30\text{--}40\ \text{mm}^2$ large crystals. Other efforts concentrated in evaporation methods. DAST decomposes when evaporated. In order to overcome this problem one approach was to evaporate the two components of DAST separately and using a carrier gas flow to deposit them on a substrate [50–53]. The surface of the obtained film is rough, with a thickness varying between 1 and $5\ \mu\text{m}$. This is due to a crystallite diameter of only about $200\ \text{nm}$. Thin films of DAST have also been prepared by polishing down bulk crystals. The thinnest obtained samples were around $20\ \mu\text{m}$ [54]. The main drawbacks of this method are the cracks that may form during polishing in the ultimate slimming step since the mechanical shear strength will proportionally decrease with the thickness.

In our laboratory several new exploratory planar solution growth methods for organic materials have been developed, in particular for the DAST/methanol system: the two-dimensional ΔT method, the traveling cell technique, the capillary and ΔT -aided capillary method, the undercooled flow cell technique, the growth by solution epitaxy, and the fabrication using laminar flow [55]. The most promising of these methods are the capillary method and the solution epitaxial growth. Solution epitaxial growth showed good results, in particular with respect to the large area of these as-grown monocrystals ($4\ \text{mm}^2$). The thickness is to be further controlled with the growth temperature and cooling rate. The minimum thickness obtained throughout the different experiments was $10\ \mu\text{m}$ with the capillary growth method.

2.4 Linear optical properties

The refractive indices of DAST were measured in our laboratory with an interferometric technique [6]. The dispersion of the refractive indices was described with a Sellmeier equation of the form

$$n^2(\lambda) = n_0^2 + \frac{q\lambda_0^2}{\lambda^2 - \lambda_0^2}, \quad (2.1)$$

where $\nu_0 = c/\lambda_0$ is the resonance frequency of the main oscillator and q the oscillator strength. Contributions from all other oscillators are summarized in n_0 . The parameters, which best described the refractive index dispersion, are given in Table 2.1 [28, 45]. Figure 2.6 shows the

	n_1	n_2	n_3
q	1.645	0.469	0.234
n_0	2.078	1.585	1.565
λ_0 [nm]	533.3 ± 1	503.5 ± 1	501 ± 1

Table 2.1: Sellmeier parameters for the refractive index dispersion of Eq. (2.1) [28, 45].

refractive indices n_1 , n_2 , and n_3 as a function of the wavelength and the absorption coefficients [6, 44]. DAST crystals are highly anisotropic with a refractive index difference between $n_1 - n_2 > 0.5$ at a wavelength of $\lambda = 1.55 \mu\text{m}$. They show small absorption bands at 1700 nm, 1400 nm, and 1100 nm, which correspond to overtones of the C-H stretching frequencies. For applications in telecommunications, DAST crystals are well suited with a material absorption that is smaller than 1 cm^{-1} at $1.5 \mu\text{m}$ wavelength.

2.5 Electro-optic and nonlinear optical properties

Electro-optic modulators based on the linear electro-optic effect are widely used in telecom applications. These devices employ the phase shift of an optical wave induced by an applied electric field. Recently, considerable effort was put in the development of new materials with high electro-optic coefficients and large optical nonlinearities. DAST is an organic crystal which fulfills these requirements ($r_{111} = 47 \text{ pm/V @} 1.54 \mu\text{m}$) [28, 42] and has the advantage of a low dielectric constant ($\epsilon_{11} = 5.2$). The molecular charge-transfer axis of the nonlinear optical active chromophores deviates by only 20° from the polar axis of the crystal, compare Fig. 2.2, which is near to optimum parallel alignment with a projection factor of $\cos(20^\circ) = 0.94$.

The nonlinear optical coefficients d_{111} , d_{122} , d_{212} of DAST were measured by Maker-fringe experiments [42] and are summarized in Table 2.2 for the fundamental wavelength of 1318 nm, 1542 nm, and 1907 nm.

Figure 2.7 shows the dispersion of the free electro-optical coefficients r_{111} , r_{221} , and r_{113} of DAST bulk crystals determined using an interferometric method [6, 28]. The other measured

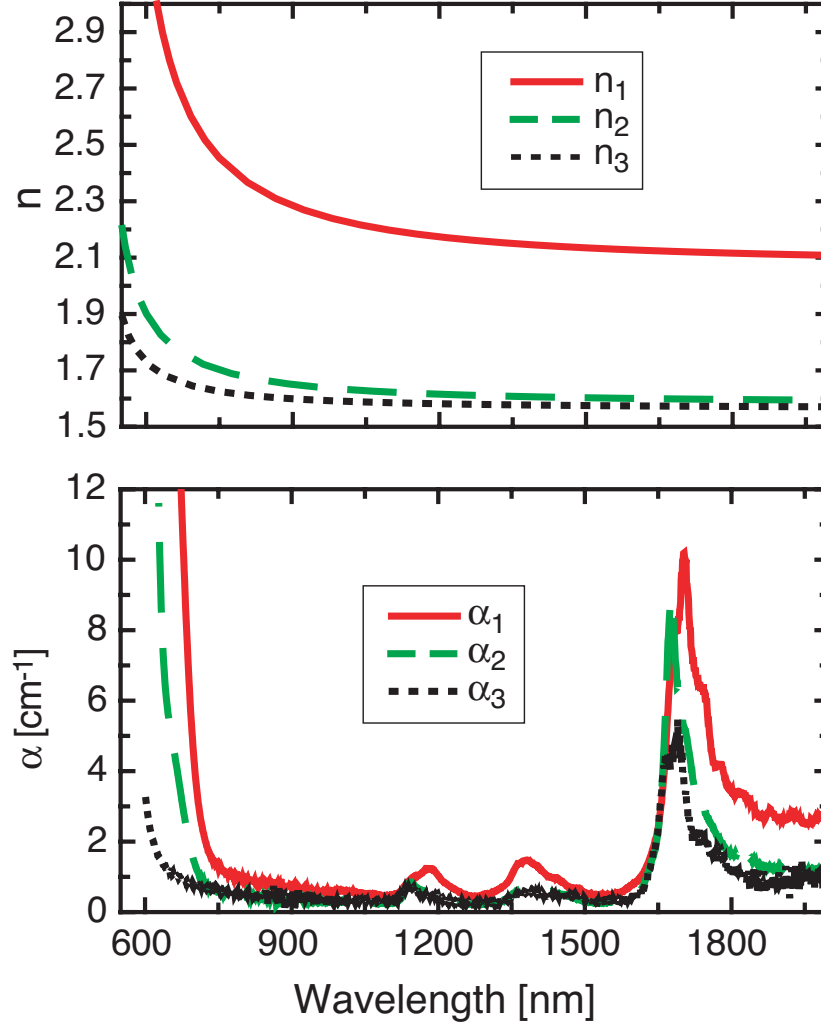


Figure 2.6: Refractive indices and absorption coefficients of DAST. Refractive indices n_1 , n_2 , n_3 and absorption coefficients α_1 , α_2 , α_3 symbolized by full, dashed and dotted curves, respectively [28, 44, 45].

λ [nm]	d_{111} [pm/V]	d_{122} [pm/V]	d_{212} [pm/V]
1318	1010 ± 110	96 ± 9	53 ± 12
1542	290 ± 15	41 ± 3	39 ± 2
1907	210 ± 55	32 ± 4	25 ± 3

Table 2.2: Nonlinear optical d coefficient of DAST determined by Maker-fringe experiments [42].

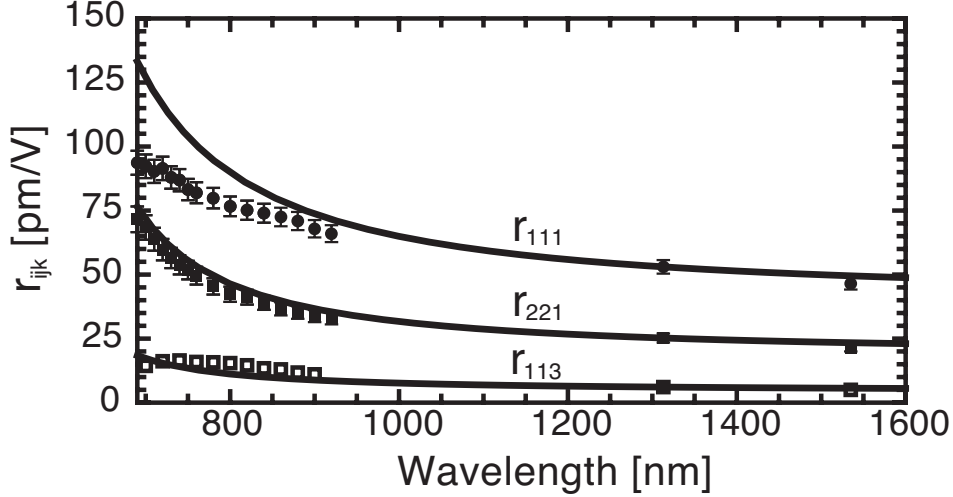


Figure 2.7: Electro-optic coefficient of DAST. Dispersion of the free electro-optic coefficient of DAST shown for r_{111} dots, r_{221} filled squared, and r_{113} open squares [28].

electro-optic coefficients r_{333} , r_{331} , and r_{223} were all smaller than 1 pm/V. For the measurements a sinusoidally modulated voltage with a frequency of $\nu = 1$ kHz and an amplitude of 10 V rms was typically applied to the DAST samples. The experimentally measured dispersion was fitted by a theoretical dispersion calculated according to the Sellmeier function and a function based on the two-level model [28]. The contribution from acoustic phonons to the linear electro-optic effect was measured by applying a step voltage to the sample [56]. A very low contribution from acoustic phonons (-2.24% at 1535 nm) was derived. The electronic contribution to the electro-optic effect r_e can be calculated with Eq. (1.26) and the measured nonlinear optical coefficient d_{111} . At 1535 nm r_e is 36 ± 2 pm/V, which is 75% of the measured unclamped coefficient [19]. Therefore, DAST is a very favorable material for broadband electro-optic switches, since the electro-optic response is large and follows almost perfectly the applied voltage from dc to at least 1 GHz, and most likely up to much higher frequencies below the optical phonon resonances [56]. Due to the large electro-optic coefficients and refractive indices of DAST, its reduced half-wave voltage $v_\pi = \lambda/(n^3 r)$ compares favorable with other organic and inorganic single crystals, e.g. $v_\pi(\text{DAST}) = 2.4$ kV, $v_\pi(\text{LiNbO}_3) = 4.6$ kV at wavelength $\lambda = 1300$ nm [28]. Some reported values of the electro-optic coefficients measured in thin films are by a factor 5 larger than those measured in bulk crystals. [28, 47]. The reason for this discrepancy is not yet known.

2.6 THz generation in DAST

Recently, DAST has also attracted lots of attention as an efficient source of Tera Hertz (THz) radiation [57–59]. Exploiting the second-order nonlinear optical process of optical rectification, THz radiation was efficiently generated by using femtosecond pulses. The polarization follows in time the amplitude of the pump pulse and thus acts as a source of THz radiation. DAST has the beneficial material properties of a very large nonlinear susceptibility $d_{111} = 1010$ pm/V at a wavelength of 1318 nm [42] combined with low dielectric constants [28]. Therefore, velocity matching between the pump pulse and the generated THz wave is possible and thus the generated THz radiation is added up constructively. This circumstance is very important to achieve high efficiencies. Tuning the pump wavelength in the range from 1000-1200 nm and from 1400-1700 nm THz radiation was efficiently generated in the frequency range from 0.3-0.7 THz and 1.7-2.3 THz, respectively [58,59].

2.7 Waveguide structuring of DAST before this work

Since DAST is an interesting material for electro-optics, waveguide structuring with different methods is being studied by several research groups. Photobleaching and photolithography were reported by Kaino et al. [60], fs laser ablation was presented by Dittrich et al. [61], and a graphoepitaxial melt growth technique was applied to DAST for the first time by Geis et al. [62]. Here, we give a short summary of the techniques previously used.

- **Photobleaching and photolithography:** For both methods DAST crystals were thinned to about $20\ \mu\text{m}$ by O_2 reactive ion etching (O_2 -RIE) and then molded on a substrate by a UV resin. Photostructuring was obtained by illuminating the crystals with a Xe lamp ($0.24\ \text{W}/\text{cm}^2$ for 65 h). The produced waveguides had a width of $40\ \mu\text{m}$. In another method serial grafted DAST waveguide structures (polymer-DAST-polymer waveguide) were produced by photolithography and subsequent O_2 -RIE etching. The waveguide width was about $30\ \mu\text{m}$. The waveguide losses for both types of structures were about $10\ \text{dB}/\text{cm}$.
- **fs ablation:** Ridge patterning was obtained by fs laser ablation with laser light of 550, 600, and 775 nm. The smallest ridge waveguide structures produced had a width of $10\ \mu\text{m}$ and a depth of $7\ \mu\text{m}$. Waveguiding with the produced structures was not demonstrated due to the lack of vertical confinement.
- **Graphoepitaxial growth:** Channel waveguide structures with a width of 2 to $15\ \mu\text{m}$ and a height of 2 to $4\ \mu\text{m}$ were produced by graphoepitaxial melt growth. For this growth technique, structures were predefined on a SiO_2 substrate, then filled with DAST-methanol-glycerin paste and locally heated. The growth speed was about 1-2 mm/s. The losses of the produced structures were below $10\ \text{dB}/\text{cm}$.

Photobleaching, photolithography, and fs ablation are suited for the production of channel waveguides, but the waveguides lack of vertical confinement. Graphoepitaxial melt growth is a promising method, since waveguide structures can be directly grown into the substrate, which is much faster compared to normal growth. However, this method is only partially suitable for DAST and other ionic organic nonlinear optical materials, since they start to decompose upon melting. The disadvantage of this method is also that the thickness is not well controllable. For the production of single mode waveguides, the accurate control of the waveguide dimensions is of great significance. Therefore, there is still a demand for new accurate structuring techniques, with which single mode waveguides in organic crystals can be realized.

2.8 Summary of the most important material properties of DAST

To give a brief overview, the most important chemical, crystallographic, linear and nonlinear optical properties are summarized below.

Formula	$C_{23}H_{26}N_2O_3S_1$
Formula weight	410.5 g/mol
Density	1.3 g/cm ³
Symmetry	monoclinic m
Lattice constants	$a = 10.365 \text{ \AA}$, $b = 11.322 \text{ \AA}$, $c = 17.892 \text{ \AA}$
Unit cell angles	$\alpha = \gamma = 90^\circ$, $\beta = 92.24^\circ$
Refractive indices	$n_1 = 2.131$, $n_2 = 1.602$, $n_3 = 1.575$ @ 1.55 μm
Absorption coefficients	$\alpha_{1,2,3} < 1 \text{ cm}^{-1}$ @ 1.55 μm
Dielectric constants	$\epsilon_1 = 5.2$, $\epsilon_2 = 4.1$, $\epsilon_3 = 3.0$ @10 ⁵ kHz
Electro-optic coefficients	$r_{111} = 47 \text{ pm/V}$, $r_{221} = 21 \text{ pm/V}$ @ 1.54 μm
Nonlinear optical susceptibility	$d_{111} = 290 \text{ pm/V}$, $d_{122} \approx d_{212} \approx 40 \text{ pm/V}$ @ 1.54 μm

Chapter 3

Photobleaching and optical properties of the organic crystal DAST §

Photobleaching of organic optical materials can be used to structure the surface layer for integrated optics applications. Linear optical properties and absorption were studied in 4-N, N-dimethylamino-4'-N'-methyl-stilbazolium tosylate (DAST) organic crystals within the absorption band from 260 – 700 nm in order to determine the depth-range of photobleaching. The results were obtained from reflectivity measurements and bleaching experiments. The depth range of photobleaching can be varied between 0.2 and 2.6 μm by selecting a suitable wavelength.

3.1 Introduction

Organic crystals with large nonlinear and electro-optical effects are interesting materials for integrated optical applications if waveguides can be fabricated. One of the most interesting materials is the organic salt 4-N, N-dimethylamino-4'-N'-methyl-stilbazolium tosylate. It crystallizes - depending on the growth conditions - in a centrosymmetric orange colored hydrated phase or in a noncentrosymmetric red colored anhydrous phase [44]. The noncentrosymmetric red phase material shows interesting electro-optic coefficients (e.g. $r_{111} = 47 \pm 8 \text{ pm/V}$ at 1535 nm) and large nonlinear susceptibilities (e.g. $d_{111} = 1010 \pm 110 \text{ pm/V}$ at 1318 nm) making it an attractive candidate for several applications at telecommunication wavelengths [28,42,56].

The production of optical waveguides in DAST is however a very difficult task. It has been shown earlier that photobleaching can lead to a reduction of the index of refraction [64, 65]. An illumination with a frequency doubled Nd:YVO₄ laser ($\lambda = 532 \text{ nm}$) having an intensity

[§]This chapter has been published in Journal of Applied Physics, **94** (3), p. 1356-1361 (2003) [63].

$I = 0.52 \text{ W/cm}^2$ for a few hours reduced the refractive index from 2.55 to 1.64 at the wavelength 633 nm and from 2.14 to 1.58 at 1550 nm [64,65]. A refractive index measurement by the light prism-coupling method yielded a depth of the refractive index change of $2.25 \mu\text{m}$ [64]. Based on this photobleaching effect grating structures on DAST crystal surfaces were fabricated by interfering two coherent beams. In this case the depth of the refractive index grating was found to be between 5 and $7 \mu\text{m}$ [64,65]. Photobleaching was also used to produce channel waveguides in thin DAST samples where ultraviolet (UV) resin was used as undercladding [66]. Thin DAST crystals were fixed on the cured UV resin and covered with a photo mask. After exposure under a Xe lamp for 65 h with an intensity of 0.24 W/cm^2 buried DAST waveguides were fabricated.

The absorption coefficients along the dielectric axes were determined in the transparency range between 700 and 2000 nm together with the dispersion of the indices of refraction [44,45]. Photobleaching is expected within the range of high absorption extending from 400 to 600 nm. So far, the absorption coefficients in this range were reported for two polarizations as measured in transmission using a thin DAST film [67].

In the present work we present the results of the measurements of the refractive indices and absorption coefficients along all three dielectric axes in the wavelength range between 266 and 700 nm using two different reflection methods. The obtained data have been found to be of fundamental importance for the bleaching experiments in the wavelength range between 266 and 600 nm. By using a suitable wavelength, light intensity, and exposure time, we could reach bleaching depths up to $2.6 \mu\text{m}$.

3.2 Refractive indices and absorption coefficients

DAST crystals used for the determination of the refractive indices and the absorption coefficients are grown from a supersaturated methanol solution by the temperature-lowering method [44]. DAST belongs to the monoclinic point group m . In Fig. 3.1 the arrangement of the crystallographic a , b , and c axes, and the dielectric x_1 , x_2 , and x_3 axes is shown. The crystallographic b axis and the dielectric x_2 axis are normal to the mirror plane. The crystallographic a axis makes an angle of $\beta = 92.2^\circ$ with the crystallographic c axis. The angles between the dielectric principal axes and the crystallographic axes a and c are 5.4° and 3.2° , respectively [45]. The polar axis of the crystal is along x_1 . Our DAST samples were prepared with one polished surface along the crystallographic ab , ac , and bc planes with a flatness of about $\pm 160 \text{ nm}$.

3.2.1 Experimental details of two different methods for measurement of light reflection

The refractive indices and the absorption coefficients were determined by two different methods which use light reflection off the surface.

In the normal incidence Kramers-Kronig method (NIKK) we measured the reflection of

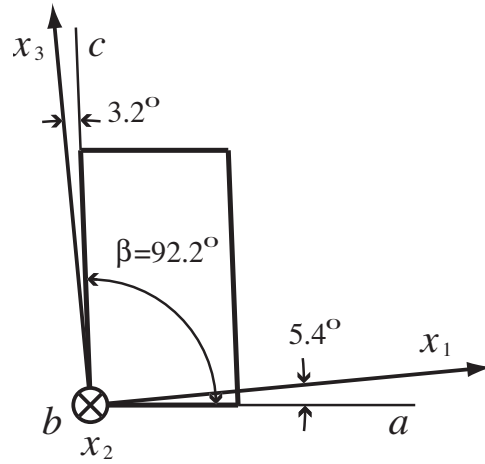


Figure 3.1: Axes orientation of DAST. Arrangement of the crystallographic a , b , and c axes, and the dielectric x_1 , x_2 , and x_3 axes in DAST.

polarized light under normal incidence within the wavelength range between 260 and 700 nm. The light was polarized along the dielectric x_1 , x_2 , and x_3 axes, respectively. From the reflection data we calculated the main refractive indices and the absorption coefficients using a Kramers-Kronig analysis [19, 68].

The second method is based on the measurement of the reflection coefficient R of laser beams reflected from the sample surface as a function of the incidence angle Θ as seen in Fig. 3.2. We name this method a variable incidence angle method (VIA). The light was either s -polarized with its polarization vector perpendicular to the incidence plane or p -polarized with the polarization vector in the incidence plane. The crystals were polished along the ab plane and were measured in two orientations with the x_2 axis and the x_1 axis in the incidence plane, respectively.

The measured angular dependence of reflectivity R is shown in Fig. 3.3 for laser beams with the wavelength 514.5 nm (dots) and 351.1 nm (open diamonds). The figure combines measurements with different orientations of the DAST sample and different polarizations of the laser beam. In Fig. 3.3(a) the s -polarization vector was parallel to the x_2 axis and in (c) the angle between the s -polarization vector to the x_1 axis was smaller than 5.4° ; in (b) and (d) the laser beam was p -polarized with the x_2 axis and the x_1 axis in the incidence plane, respectively. By comparing the reflectivity dependences in Fig. 3.3 one notes a big difference between the results at 514.5 and 351.1 nm with the light polarization having a component parallel to x_1 (cases c and d). A large reflectivity at the Brewster angle indicates a high absorption constant in the green. For the measurements shown in Figs. 3.3(a) and 3.3(b) the differences are not so pronounced in accordance with the molecular structure data which shows that the main charge-transfer axis is parallel to x_1 . At 351.1 nm the difference in reflection for different sample orientations is very small indicating a more isotropic behavior of the linear optical properties of DAST in the UV range.

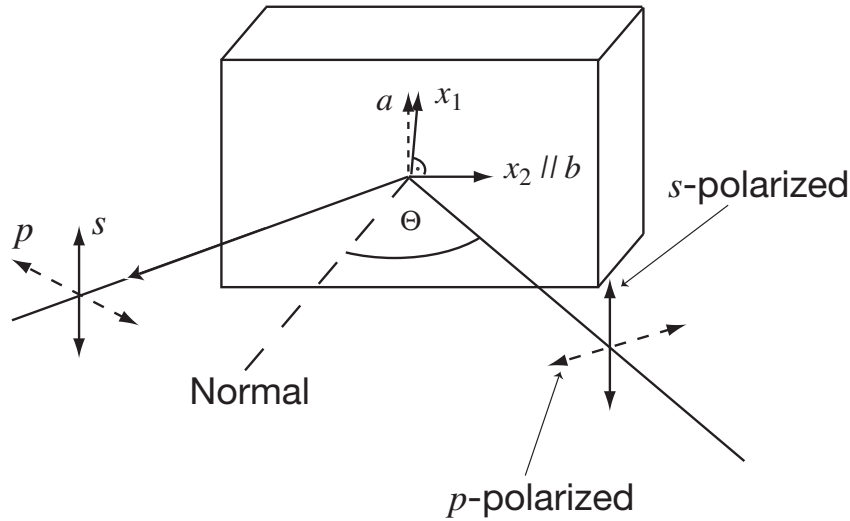


Figure 3.2: Configuration of the reflection measurements. One of the two orientations of the DAST sample used for the reflection measurement with the variable incidence angle method. The light was either *s*-polarized or *p*-polarized. Θ denotes the incidence angle.

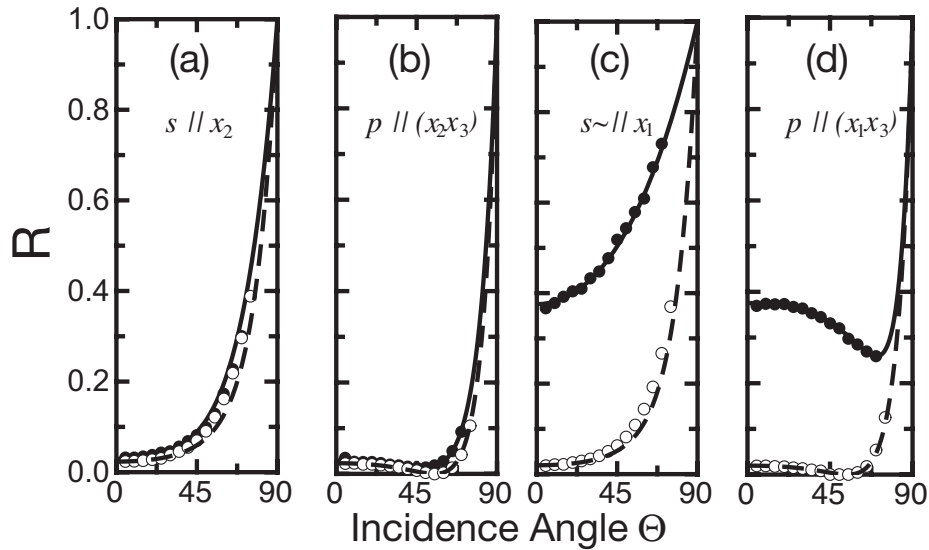


Figure 3.3: Measured reflection. Measured reflection coefficient R as a function of the incidence angle for the wavelength of 514.5 nm (dots) and 351.1 nm (open diamonds). The lines are the theoretical curves fitted to the experimental data. In Fig. 3.3(a) the *s*-polarization vector was parallel to the x_2 axis and in (b) the laser beam was *p*-polarized with the x_2 axis in the incidence plane. In (c) the angle between the *s*-polarization vector to the x_1 axis was smaller than 5.4° and in (d) the *p*-polarization vector was in the (x_1x_3) plane.

We analyzed our measurements with the help of the Fresnel formulas. The complex amplitude reflectivity coefficients \hat{r}_s and \hat{r}_p for s - and p -polarized light are given by

$$\hat{r}_s = \frac{\cos \Theta - \hat{n}_s \cos \Theta'_s}{\cos \Theta + \hat{n}_s \cos \Theta'_s}, \quad \hat{r}_p = \frac{\hat{n}_p(\Theta'_p) \cos \Theta \cos(\Theta'_p - \Omega) - \cos \Omega}{\hat{n}_p(\Theta'_p) \cos \Theta \cos(\Theta'_p - \Omega) + \cos \Omega}, \quad (3.1)$$

where $\hat{n}_{s,p} = n_{s,p} - i \cdot k_{s,p}$ is the complex refractive index, $k_{s,p}$ the absorption constant and $n_{s,p}$ the refractive index of the medium. The absorption coefficient α is defined as $\alpha = 4\pi \cdot k/\lambda_0$, where λ_0 is the wavelength of the incidence light in vacuum. The angle $\Theta'_{s,p}$ is given by the refraction law

$$\hat{n}_{s,p} \sin \Theta'_{s,p} = \sin \Theta. \quad (3.2)$$

In our case $\hat{n}_s = n_1$ or n_2 , and \hat{n}_p is related to n_3 and n_1 or n_2 over

$$\frac{1}{\hat{n}_p^2} = \frac{\cos^2 \Theta'_p}{n_{1,2}^2} + \frac{\sin^2 \Theta'_p}{n_3^2} \quad (3.3)$$

and

$$\tan \Theta'_p = \frac{n_3^2}{n_{1,2}^2} \tan \Omega \quad (3.4)$$

depending on the orientation of the crystal. Θ'_p is the angle between the sample normal and the wave normal in the crystal, while Ω is the angle between the sample normal and the energy propagation direction in the crystal.¹ The reflection coefficient R is defined as the absolute square of the complex reflection coefficient. The full line in Fig. 3.3 presents theoretical Fresnel curves fitted to the experimental data with the refractive indices n_1 , n_2 , and n_3 and the absorption coefficients α_1 , α_2 , and α_3 as the free parameters. All four measurements shown in Fig. 3.3 were taken into account in order to determine one parameter set. We repeated these measurements using the Ar⁺ laser lines 514.5, 488.0, 457.9 (Lexel) and 351.1 nm (Spectra Physics), a frequency doubled laser diode operating at 430 nm (Rainbow Photonics), and a frequency quadrupled Nd:YAG laser having a wavelength of 266 nm (NanoLaser). By comparing the reflection data R at these wavelengths, the biggest difference is observed in Figs. 3.3(c) and 3.3(d), where reflection is the biggest at 514.5 nm and becomes smaller for shorter wavelengths, approaching a similar behavior as shown in Fig. 3.3 at 351.1 nm.

Fig. 3.4(a) shows the absorption coefficients α_1 , α_2 , and α_3 and Fig. 3.4(b) the refractive indices n_1 , n_2 , and n_3 as a function of the wavelength λ_0 . The lines show the results obtained with the NIKK method, whereas the points represent the data obtained with the VIA method. The refractive indices and absorption coefficients determined with the VIA method are listed in Table 3.1.

¹Note that in the original publication [63], the difference between Θ'_p and Ω was neglected, which does not influence the results within the reported error.

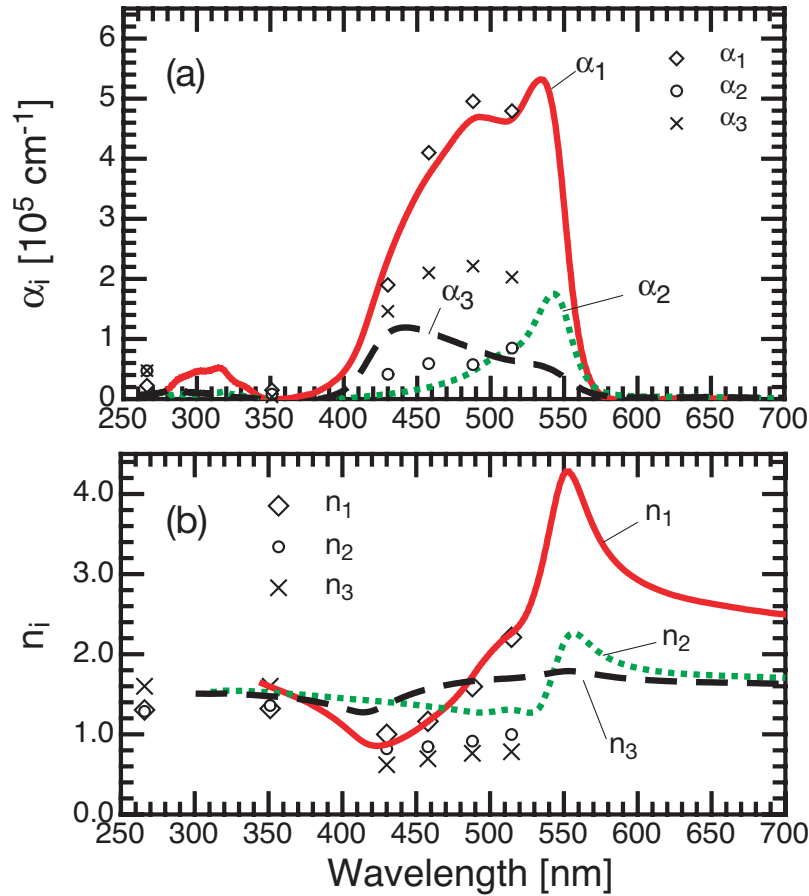


Figure 3.4: Refractive indices and absorption coefficients. Wavelength dependence of the absorption coefficients α_1 , α_2 , and α_3 (a) and the refractive indices n_1 , n_2 , and n_3 (b) of DAST within the absorption band. Lines present the results obtained with the NIKK method. Results obtained by the VIA method are presented as points.

Wavelength [nm]	n_1	n_2	n_3	α_1 [10^5 cm^{-1}]	α_2 [10^5 cm^{-1}]	α_3 [10^5 cm^{-1}]
514.5	2.2 ± 0.3	1.00 ± 0.02	0.78 ± 0.08	4.79 ± 0.05	0.83 ± 0.02	2.0 ± 0.3
488.0	1.6 ± 0.4	0.91 ± 0.02	0.76 ± 0.14	4.9 ± 0.4	0.57 ± 0.06	2.2 ± 0.4
457.9	1.2 ± 0.3	0.85 ± 0.01	0.69 ± 0.13	4.1 ± 0.4	0.6 ± 0.3	2.1 ± 0.3
430	1.0 ± 0.3	0.8 ± 0.3	0.6 ± 0.4	1.9 ± 0.6	0.4 ± 0.3	1.5 ± 0.9
351.1	1.32 ± 0.03	1.36 ± 0.02	1.6 ± 0.4	0 ... 0.7	<1.0	< 0.7
266	1.30 ± 0.05	1.29 ± 0.05	1.6 ± 0.4	0 ... 1.5	< 0.6	< 0.9

Table 3.1: Refractive indices and absorption coefficients obtained by the VIA method.

3.2.2 Results and discussion

As we see in Figs. 3.4(a) and 3.4(b) absorption coefficients α_1 , α_2 , and the refractive index n_1 for both measurements are in good agreement. The qualitative wavelength dependence of α_3 and n_3 is the same for both reflection measurements, however, the absolute values differ by a factor of three for α_3 and a factor of two for n_3 . This can be partly explained by the differences in sample geometries used for the determination of α_3 and n_3 . In the NIKK method the reflection from an *ac* plate was measured under normal incidence with light polarized along the dielectric x_3 axis, whereas in the VIA method we used only an *ab* plate. Therefore polarization has only a small component in the x_3 direction. Hence the measurements of α_3 and n_3 with the VIA method are less reliable. On the other hand, the Kramers-Kronig analysis can be performed only over a finite wavelength range, which limits the accuracy of the data obtained by the NIKK method. Furthermore, we also neglected the small angle between the dielectric x_1 axis and the crystallographic *a* axis. The dielectric axis x_3 is always orthogonal to the (x_1x_2) plane and in this approximation also orthogonal to the crystallographic *ab* plane. This seems to be a valid approximation because for a *p*-polarized probe beam in the (x_1x_3) plane the difference of reflection for a 180° rotated sample around the surface normal was within the experimental error.

By comparing our results with those reported in Ref. [67], one sees that in our new measurements the peak values for α_1 and α_2 are about 30 and 10 times, respectively, larger than the previously estimated values based on transmission measurements using thin DAST films. A possible reason could be that the physical properties of the previously used thin films and our bulk crystals vary substantially due to different growth conditions. Note that in our measurements the reflectivities were within the experimental error when we measured on different spots of the crystal or on a different crystal with the same orientation of the axes. The other cause of discrepancy may be the use of different refractive indices - which were not given in the paper [67] - in correcting the transmission results for the Fresnel losses and multiple reflections.

3.3 Photobleaching of DAST

We performed different bleaching experiments at various wavelengths under normal beam incidence to investigate the parameters required for waveguide fabrication. The following laser lines were used: 351.1 nm, 363.8 nm (Ar⁺⁺ laser, Spectra Physics), 430 nm (frequency doubled laser diode, Rainbow Photonics), 457.9 nm, 488.0 nm, 514.5 nm (Ar⁺, Lexel), 532 nm (frequency doubled Nd:YAG laser, Crystal Laser), 580 nm, and 585 nm (Dye laser, Coherent). The laser beams were 3-4 mm wide and the intensity distribution of the laser beam was almost Gaussian. The peak intensity I_0 of the bleaching beam was measured using a pinhole with a diameter of 0.97 mm at the laser beam center. Because bleaching is a destructive experiment lower quality samples were used with polished surfaces parallel to the *ab* plane.

In Fig. 3.5 we show a typical bleached spot produced by irradiation with $I_0 = 5.0 \text{ W/cm}^2$ of

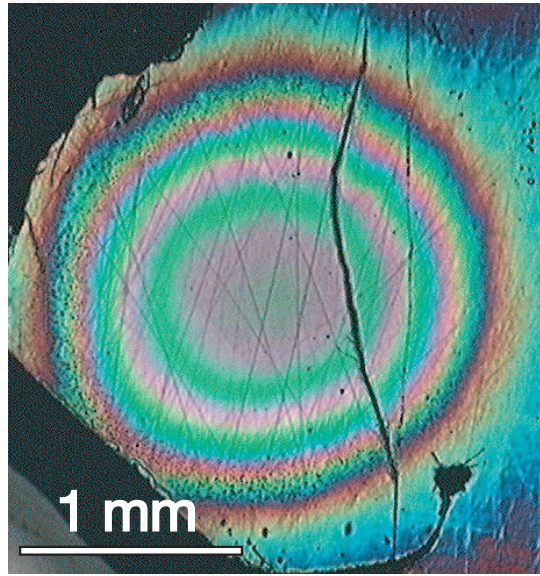


Figure 3.5: Bleached DAST crystal. White light interferogram pattern of a photobleached spot from an ab plate of DAST. Photobleaching was performed at a wavelength $\lambda_B = 488$ nm polarized along x_2 axis with an exposure time of 30 h and $I_0 = 5.0$ W/cm². The vertical crack was already visible before bleaching but became more pronounced afterwards.

488 nm laser light polarized along the x_2 axis. The colored rings shown in Fig. 3.5 were even visible by naked eye. The optical properties of the bleached samples were then investigated by evaluating the interference pattern using red and white light interferometry.

3.3.1 Estimation of the refractive indices in bleached DAST

A schematic cross section through a bleached spot is shown in Fig. 3.6. The refractive indices in the bleached area are smaller than in the unbleached area as reported in Refs. [64] and [65].

An estimation of the refractive indices of bleached DAST can be made by comparing the pictures (A) and (B) of Fig. 3.7. The spot shown in these figures was bleached with 579 nm light polarized parallel to the x_2 axis. The pictures (A) and (B) were made with red light illumination when the polarization vector of the light was almost parallel to the x_1 axis and x_2 axis in pictures (A) and (B), respectively. Because the same diameter of the dark circles in both pictures is observed, it can be concluded that the dielectric properties of the material in the bleached region are nearly isotropic. Further on, by looking at the contrast of the two pictures, one can see that the refractive index change Δn_2 is quite small. Therefore, we neglect Δn_2 and we use the unbleached value n_2 for the refractive index n_B of bleached DAST.

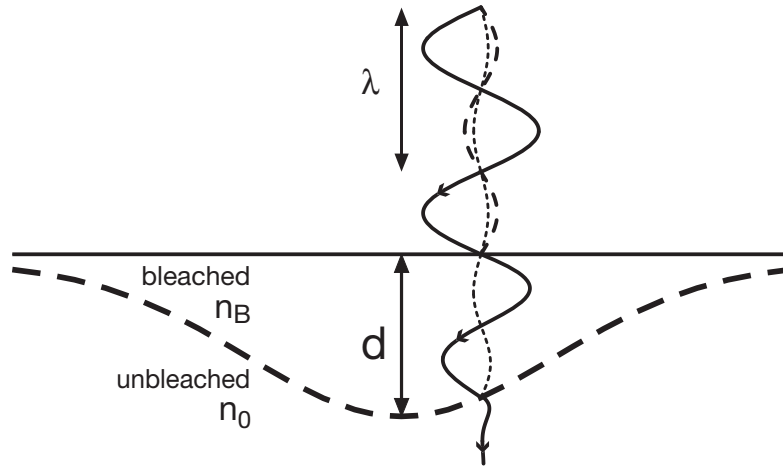


Figure 3.6: Cross section of a bleached spot. Cross section through a bleached spot observed in reflected light of wavelength λ . d denotes the depth of the bleached area, n_B the refractive index of bleached DAST, n_0 the refractive index of the unbleached region. The full sine line represents the incoming wave, the dotted and dashed lines represent the reflection at the surface of the crystal and at the interface between bleached and unbleached material, respectively. The amplitudes of the waves are shown only at a spot of constructive interference of the two reflected beams. Note that the tilt angles of the bleached area boundary are greatly exaggerated and the waves are reflected almost normally.

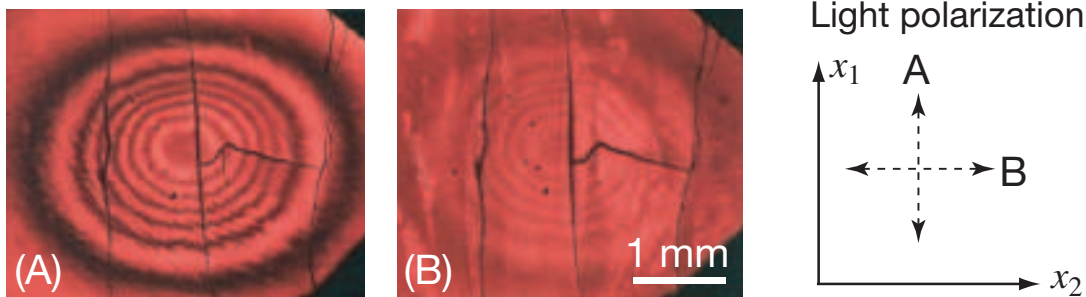


Figure 3.7: Red light interferogram of a photobleached spot. The pictures were taken under a microscope with polarized red light. (A): light is polarized along the x_1 axis; (B): light is polarized along the x_2 axis. On the right, the orientation of the dielectric axes and polarizations are shown used for making the pictures (A) and (B). For the bleaching, light of $\lambda_B = 579$ nm was used, polarized along the dielectric x_2 axis, with $I_0 = 3.6$ W/cm², and the bleaching time was $t = 16.5$ h.

3.3.2 Determination of the bleaching depth

With the help of interferometry and using the above assumptions the maximal bleaching depth d_{\max} of the bleaching process can be estimated. The transition region between the bleached and unbleached crystal area is relatively narrow as can be understood with the help of the model presented in the following section. The light beam, which is partially reflected at the air-crystal interface interferes with the beam, which is reflected at the interface between the bleached and unbleached area, as proposed in Fig. 3.6. For constructive interference of the two beams, the following equation has to be fulfilled:

$$d = \frac{\lambda_{\text{DAST}}}{2} m = \frac{\lambda}{2n_B} m, \quad m = 1, 2, 3, \dots, \quad (3.5)$$

where $\lambda_{\text{DAST}} = \lambda/n_B$ is the wavelength in DAST, λ the wavelength in vacuum, n_B the refractive index of bleached DAST, and m an integer number. The bleaching depth increases from the edge to the center of the bleached spot. According to Eq. (3.5) constructive interference is observed at certain depths giving rise to interference rings. Therefore interference rings can be used to calculate the thickness of the bleached area if the refractive index n_B is known.

The bleached spot in Fig. 3.5 has four green rings from the edge to the center of the spot, therefore $m = 4$. For the refractive index of bleached DAST we take the value of $n_B \approx n_2$ as explained in Subsection 3.3.1, here for the green wavelength range (Table 3.1). The maximal bleaching depth can be calculated with the help of Eq. (3.5), which gives a bleaching depth of $1.0 \pm 0.1 \mu\text{m}$.

To check the interferometric measurements we determined the bleaching depth also by Ar^+ ion sputtering in a plasma ion source (OXFORD Plasmalab 80 Plus). We used the following process parameters: Ar^+ flow 50 sccm (standard cube centimeter per minute), gas pressure $25 \mu\text{bar}$, rf power 200 W, and dc bias voltage -400 V. The bleached spots became smaller and the interference rings were shrinking while the material was removed. The sputtering parameters of DAST are not known, but based on the data of similar materials the results of the interferometric measurements were confirmed to $\pm 20\%$.

3.3.3 Modeling of the bleaching process

Bleaching DAST crystals leads to breaking of some molecular bonds and/or to changes in the molecular arrangement. This can lead to a reduction of the high polarizability of the molecules and therefore to a reduction of the refractive indices. After a certain amount of energy is deposited, almost all susceptible bonds are broken and/or the molecules are rearranged. The bleaching process is then completed and longer illumination does not lead to a further reduction of the refractive indices. The refractive index change Δn as a function of the exposure $\Phi = I \cdot t$, where I is the intensity and t the bleaching time, can be written as

$$\Delta n(\Phi) = \Delta n_0 \left[1 - \exp\left(-\frac{\Phi}{\Phi_0}\right) \right], \quad (3.6)$$

where Δn_0 is the peak refractive index change and Φ_0 the exposure after the refractive index has changed by $63\% \Delta n_0$. During bleaching the intensity varies with the depth z as

$$I(z) = I \exp(-\alpha_{\lambda_B} z), \quad (3.7)$$

where I is the intensity profile at the crystal surface and α_{λ_B} is the absorption coefficient at the bleaching wavelength λ_B . We can neglect any variation of α_{λ_B} with depth and time, while we apply our model only to the case when the bleaching beam is polarized along the dielectric x_2 axis. In this case changes in n_2 are small and consequently the absorption coefficient α_2 can also be assumed not to change significantly. By inserting $\Phi = I \cdot t$ and Eq. (3.7) in Eq. (3.6) one gets the refractive index change Δn as

$$\Delta n(z, t, I, \Phi_0, \alpha_{\lambda_B}) = \Delta n_0 \left[1 - \exp\left(-\frac{It \exp(-\alpha_{\lambda_B} z)}{\Phi_0(\lambda_B)}\right) \right]. \quad (3.8)$$

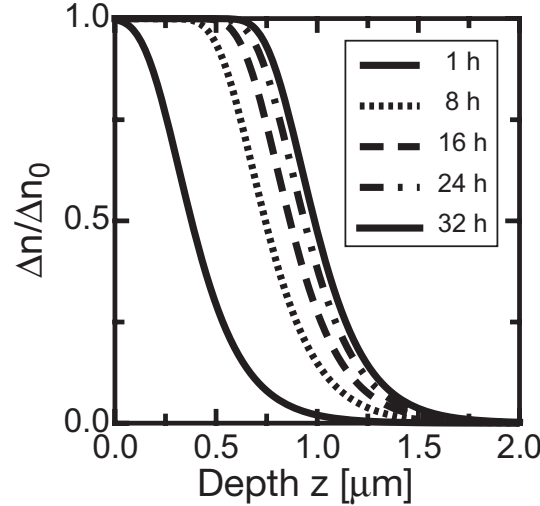


Figure 3.8: Modeled refractive index change. Normalized change of the refractive index $\Delta n/\Delta n_0$ as a function of the crystal depth z for different bleaching times t and for $I = 5 \text{ W/cm}^2$, $\alpha_{\lambda_B} = 5.7 \cdot 10^4 \text{ cm}^{-1}$ at $\lambda_B = 488 \text{ nm}$ and $\Phi_0 = 3 \text{ kJ/cm}^2$.

Fig. 3.8 shows the calculated refractive index change Δn divided by Δn_0 as a function of the crystal depth z for different bleaching times t . The parameters I and α_{λ_B} were chosen to correspond to the experimental spot shown in Fig. 3.5. The exposure $\Phi_0 = 3 \text{ kJ/cm}^2$ was chosen so that the value of $\Delta n/\Delta n_0$ was 0.5 after 32 h at $z = 1 \mu\text{m}$.

The refractive index changes from $3/4 \Delta n_0$ to $1/4 \Delta n_0$ occur always within 250 nm for all bleaching times. Hence, a sharp transition region between bleached and unbleached areas can always be assumed confirming our method of determination of the bleaching depth in Subsection 3.3.2.

3.3.4 Results and discussion

The wavelength, intensity, and time dependences of the bleaching process have been investigated in several bleaching experiments. The results are summarized in Table 3.2.

Exp.Nr.	λ_B [nm]	I_0 [W/cm ²]	t [min]	$I_0 \cdot t$ [kJ/cm ²]	pol.	α_2 [10 ³ cm ⁻¹]	d_{\max} [nm]	Φ_0 [kJ/cm ²]
1	585	3.6	1020	217.3	x_2	7	2600	50
2	580	3.6	540	115.0	x_2	9	1500	44
3	532	1.2	930	64.2	x_2	137	500	0.1
4	488	5.0	1800	514.1	x_2	47	1000	7
5	488	4.2	260	65.4	x_2	47	750	3
6	488	6.6	150	59.7	x_2	47	750	3
7	488	4.2	275	69.1	x_2	47	600	6
8	488	0.9	1080	57.7	x_2	47	300	21
9	458	1.9	660	76.4	x_2	20	500	40
10	351	2.4	180	25.9	x_2	< 0.1	-	-
11	351	1.5	600	54.0	x_1	< 0.1	-	-
12	364	2.1	315	38.7	x_2	< 0.1	-	-
13	364	2.1	505	62.1	x_1	2	-	-

Table 3.2: Bleaching parameters of some relevant experiments, where I_0 is the peak intensity, t the bleaching time, $I_0 \cdot t$ is the deposited energy. The results of these experiments are the maximal bleaching depth d_{\max} and the parameter Φ_0 .

The deepest bleaching could be reached with wavelengths near the absorption edge in the yellow range as used in experiments 1 and 2. Bleaching depths of 1.5 μm for 580 nm and an intensity of 3.6 W/cm² during 9 h, and 2.6 μm for 585 nm and an intensity of 3.6 W/cm² during 14 h could be reached.

In experiment 3 we bleached with the wavelength of 532 nm for which the absorption is by a factor of 20 higher than at 585 nm. If we compare our results on the bleaching depth obtained at this wavelength with those in Refs. [64] and [65], we could only achieve a bleaching depth of 500 nm and not the previously reported $2.25 \pm 0.75 \mu\text{m}$ even though using a higher intensity and a double exposure time.

With experiments 4 and 5, we observed the dependence of the bleaching depth on time. The intensity was in the same range with 5.0 W/cm² for experiment 4 and 4.2 W/cm² for experiment 5. By bleaching spot 4 six times longer than spot 5, the bleaching depth increased from 750 nm to only 1 μm . This is in agreement with our description presented in Fig. 3.8, which shows a saturation of the bleaching process in time.

In experiments 6, 7, and 8 we observed the dependence of the bleaching process on intensity.

We used the following three different intensities; 6.6 W/cm^2 in experiment 6, 4.2 W/cm^2 in experiment 7, and 0.9 W/cm^2 in experiment 8. The total deposited energy density in all three experiments was in the same range of approximately 60 kJ/cm^2 and the bleaching wavelength was 488 nm . By comparing the values of Φ_0 it is obvious that Φ_0 depends on intensity. For higher intensities the bleaching process is faster. We tentatively attribute this dependence to a higher temperature increase during bleaching with higher intensities. Neither with 488 nm nor 458 nm was it possible to bleach the material deeper than $1 \mu\text{m}$.

We also tried to bleach DAST near the edge of the UV absorption band with the wavelengths 351 and 364 nm . No bleaching was visible neither with light polarized along the x_1 axis nor with light polarized along the x_2 axis. The absorption seems to be too small and therefore no bleaching occurs. The bleaching parameters for these experiments are reported in rows 10-13 in Table 3.2.

Based on the data from Table 3.2 we conclude that the preferred bleaching wavelengths lie near the absorption edge in the yellow if deeper bleaching is desired. For the other wavelengths within the absorption band the bleaching process slows down at smaller bleaching depth due to the high absorption as described by Eq. (3.8). The bleaching process depends also on intensity.

3.4 Conclusions

New measurements of optical properties of DAST single crystals were used in order to refine the refractive indices and the absorption coefficients within the absorption band for the three dielectric axes of DAST crystal. Two different methods - the normal incidence Kramers-Kronig method and the method based on the measurement of a laser beam reflected from the sample surface as a function of the incidence angle - were used and have produced similar results. We have found that by photobleaching DAST crystals with light polarized along the x_2 axis with wavelengths between 458 and 585 nm , and bleaching depth between 0.2 and $2.6 \mu\text{m}$ can be reached. Therefore photobleaching can be a useful method for structuring DAST surfaces for integrated optics. The obtained parameters can be used to calculate the depth of photobleached material that can be achieved with available lasers of different wavelengths.

Chapter 4

Ion implanted optical waveguides in DAST [§]

We report for the first time to our knowledge optical waveguiding in an organic crystalline waveguide produced by ion implantation. Using H^+ ions a refractive index barrier suitable for waveguiding has been realized in the highly nonlinear optical organic crystal 4-N, N-dimethylamino-4'-N'-methyl-stilbazolium tosylate (DAST). The refractive index changes in the waveguiding region as a function of the distance from the surface have been measured. Maximal refractive index changes of up to -0.2 and -0.1 at wavelengths of 633 and 810 nm have been realized, respectively. The waveguide refractive index profiles as a function of the ion fluence have been determined. Planar waveguiding has been demonstrated by polishing sharp edges and using conventional end-fire coupling. The measured losses are ≈ 7 dB/cm at $1.57 \mu\text{m}$.

4.1 Introduction

Organic electro-optic materials combine very fast nonlinearities with low dielectric constants which result in larger optical bandwidths of over 100 GHz compared to standard inorganic materials used in telecommunication [26]. The two organic material classes, electro-optic polymers and organic crystals have been intensively studied as integrated optics constituents during the last years. Polymers are potentially cheap and thin film processing is easy, nevertheless they often show thermal and photochemical instabilities and their nonlinearities are generally lower than in the crystalline counterparts. On the other hand, organic crystals have superior nonlinearities, thermal and photochemical stability, but growth of high quality thin films is still a challenging step on the way to develop very large scale integrated (VLSI) photonic devices.

DAST (4-N, N-dimethylamino-4'-N'-methyl-stilbazolium tosylate) is a widely investigated organic crystal with large electro-optic coefficients $r_{111} = 77 \pm 8$ pm/V at 800 nm and $r_{111} =$

[§]This chapter has been published in Optics Express, **15** (2), p. 629-638 (2007) [69], except Subsection 4.5.2.

47 ± 8 pm/V at 1535 nm combined with a low dielectric constant ($\epsilon_{11} = 5.2$) [28,56]. Therefore it is an interesting candidate for high-speed applications in telecommunications provided that optical waveguiding is achievable.

Many techniques to produce waveguiding structures in DAST have already been proposed, including photobleaching [60,63], photolithography [60], fs laser ablation [61], graphoepitaxial melt growth [62], and thin film solution growth [47,55]. However, a fast standard technique allowing for a reliable thickness control of the guiding layer to a few tens of a micrometer, which is a prerequisite for the production of integrated optical structures, has not yet been established.

We decided to employ ion implantation since it is widely used for the production of waveguides in inorganic materials, for which other techniques can not be applied [70]. We present the fabrication of planar optical waveguides in an organic crystal by ion implantation. We show that the process of H^+ and He^+ ion implantation in organic crystals is essentially different from the phenomenon in inorganic crystals or polymers. We demonstrate that the thickness of the guiding layer can be controlled to a few tens of micrometers by H^+ implantation. Furthermore, we present measurements of the refractive index profile and waveguide modes, and finally demonstrate planar waveguiding by end-fire coupling.

4.2 Ion implantation experiments

The crystals used in our experiments were grown in our laboratory from supersaturated methanol solution by the temperature-lowering method [44]. DAST belongs to the monoclinic point group m [28]. The crystallographic b axis and the dielectric x_2 axis are normal to the mirror plane, and the dielectric x_1 axis makes an angle of 5.4° to the polar a axis in the symmetry plane [63]. The single crystals were cut approximately perpendicular to the dielectric axes. The typical sample size was around $7 \times 4 \times 4$ mm³ with the longest dimension along x_1 . In order to use the largest electro-optic coefficient r_{111} , the guided light should be polarized parallel to x_1 and the refractive index n_1 should be altered to ensure confinement. The x_1x_2 surface polished to $\lambda/4$ surface quality was implanted at room temperature with He^+ or H^+ ions. The ion current was kept at about 2 nA and 40 nA for He^+ and H^+ ions, respectively, while the beam was scanned over an area of 9×9 mm² to avoid thermal damage and to ensure homogenous implantation.

In order to get waveguides of small thickness we used the ions with the lowest energy achievable with the 6 MeV EN Van de Graaff tandem accelerator, that is 720 keV He^+ ions and 1 MeV H^+ ions. To avoid channeling along a crystallographic axis, the samples were tilted relative to normal incidence by 10° for He^+ ion implantation. To additionally reduce the implantation depth of H^+ ions the samples were tilted by 60° . This shortens the implantation depth by a factor of 2, having approximately the same effect as reducing the ion energy to 650 keV at normal incidence according to SRIM (The Stopping and Range of Ions in Matter) calculations (www.srim.org).

4.3 Refractive index profiles of He^+ and H^+ ion implantation

4.3.1 Model of ion implantation

The penetrating ion is losing energy on its track in the target material. This energy deposition $G(z) = dE(z)/dz$, which can be calculated with SRIM, has been shown to be responsible for the refractive index change. $G(z)$ is given by two contributions: electronic energy deposition $G_{el}(z) = (dE(z)/dz)_{el}$ due to electronic excitations prevailing at high ion velocities, and nuclear energy deposition $G_n(z) = (dE(z)/dz)_n$ due to collisions with nuclei that occur as the ion is slower at the end of the ion track. The index change induced by ion irradiation can be modeled assuming that the total refractive index change $\Delta n(z)$ is a sum of the changes due to electronic and nuclear energy deposition [71]:

$$\Delta n(z) = \Delta n_{el}(z) + \Delta n_n(z). \quad (4.1)$$

The phenomenological dependences are given by [71]

$$\Delta n_n(z) = \Delta n_{n,0} \left[1 - e^{-\left(\phi \frac{G_n(\mu z)}{G_{n,0}}\right)^{\gamma_n}} \right] \quad (4.2)$$

$$\Delta n_{el}(z) = \Delta n_{el,0} \left[1 - e^{-\left(\phi \frac{G_{el}(\mu z)}{G_{el,0}}\right)^{\gamma_{el}}} \right], \quad (4.3)$$

where $\Delta n_{n,0}, \Delta n_{el,0}$ are the saturation refractive index changes. Furthermore, $G_{n,0}, G_{el,0}$ represent the saturation energies and γ_n, γ_{el} the exponential factors for the nuclear and electronic energy deposition, respectively, while ϕ is the ion fluence. The parameter μ accounts for the limited accuracy in the prediction of the ion range obtained with SRIM.

4.3.2 Reflection scan measurement method

After implantation we investigated the optical properties of the samples by measuring the reflection of a wedge-polished surface [72]. The refractive index n is related to the intensity reflection coefficient $R = I_R/I_0$ by the Fresnel formula, where I_0 is the incident light intensity and I_R the reflected one. For normal incidence and negligible absorption, n is given by

$$n = \frac{1 + \sqrt{R}}{1 - \sqrt{R}}. \quad (4.4)$$

The sample was polished under an angle of 1° as seen in Fig. 4.1 to increase the spatial resolution of the measurement in z direction. With a laser beam focused to less than $5 \mu\text{m}$ the sample was then scanned in η direction in steps of $5 \mu\text{m}$ yielding a depth resolution in z direction of about $0.1 \mu\text{m}$. In order to probe the refractive index n_1 the incident light was polarized parallel to the dielectric x_1 axis that is normal to the ηz plane. The back reflected light was deflected

by a beam splitter and then detected with a photodiode. Signal distortions due to polishing imperfections were reduced by averaging over 22 scans taken at different positions of the sample by translating it normal to the ηz plane. In addition the back surface of the sample was polished under an angle of 8° to avoid collection of parasitic light (see Fig.4.1).

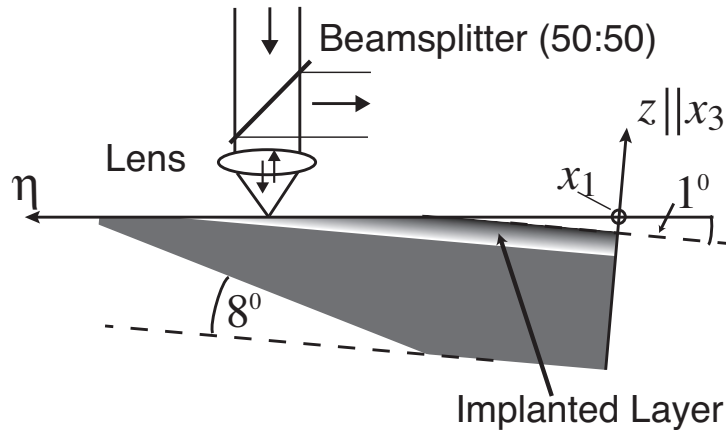


Figure 4.1: Reflection measurement setup. Experimental setup for the determination of the refractive index profile by measuring the back reflected light from a wedged-polished sample, which was scanned in η direction in steps of $5 \mu\text{m}$ yielding a depth resolution of less than $0.1 \mu\text{m}$ in z direction.

4.3.3 Refractive index profile of He^+ ion implantation

First implantation experiments were done with 720 keV leading to an ion range of about $3.1 \mu\text{m}$ in DAST as shown in Fig. 4.2. By comparing the magnitude of the electronic and the nuclear energy deposition and the area enclosed by the curves, we see that most of the ion energy is deposited by electronic excitations.

Implantation with a fluence of 1.5×10^{14} ions/ cm^2 of 720 keV He^+ resulted in a large reduction of the refractive index of around $\Delta n_1 \approx -0.9$ for $\lambda = 633 \text{ nm}$ at the surface.

With a fluence reduced to 0.8×10^{13} ions/ cm^2 a maximal refractive index change Δn_1 of about -0.15 was measured at the surface as depicted in Fig. 4.3. In inorganic materials, such refractive index changes are only possible with fluences that are more than one order of magnitude higher. The refractive index profile in DAST after He^+ implantation has a shape analogous to the electronic energy loss curve. Therefore, we can conclude that the refractive index is dominantly changed due to electronic energy deposition.

The effect of implantation is therefore essentially different compared to inorganic crystals, for which the nuclear displacements at the end of the ion track are the dominant mechanism of the refractive index change, leading to an optical barrier with reduced refractive index [70, 73]. The effect of implantation is also not the same as in the polymer PMMA [70, 74], where an increase of the refractive index was detected and attributed to an increased absorption. In He^+

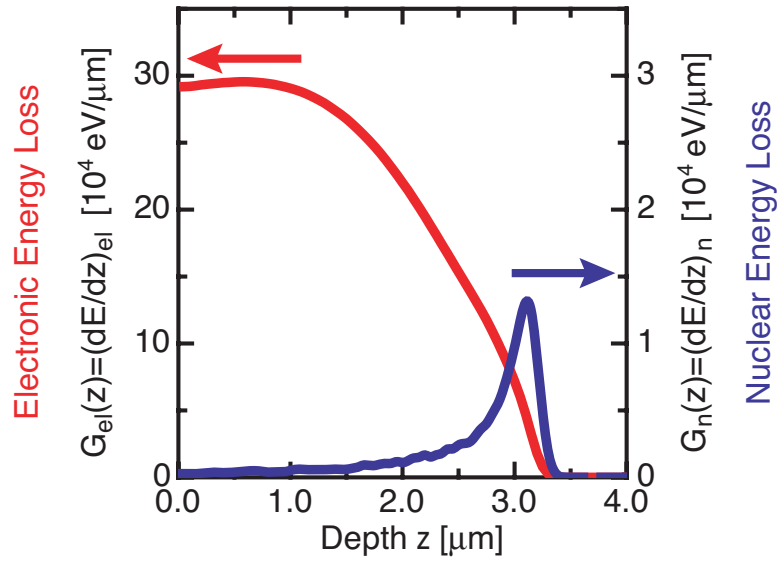


Figure 4.2: Energy deposition of He^+ ions. Nuclear (blue) and electronic (red) energy deposition in dependence on the implantation depth for 720 keV He^+ ions in DAST calculated with SRIM.

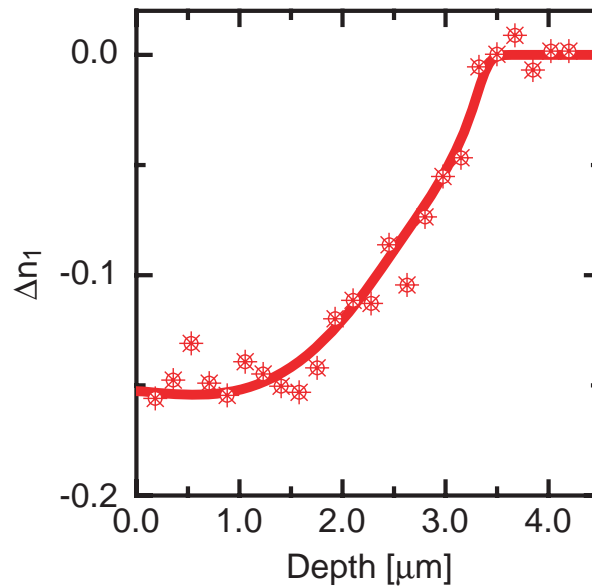


Figure 4.3: Refractive index change. Refractive index change of n_1 versus implantation depth z at the wavelength 633 nm for 720 keV He^+ ion implantation in DAST with a fluence of $\phi = 0.8 \times 10^{13}$ ions/cm² measured with the reflection scan method (Fig.4.1). The full curve is a guide line for the eye.

implanted DAST the refractive index was decreased. We attribute the lowered refractive index to a decrease of the polarizability of some molecules due to broken bonds.

We can conclude that He^+ ion implantation is not suitable for the production of planar waveguide structures in organic crystals, because of the diffusion-like shape of the refractive index profile and the fact that the refractive index is reduced, resulting in an implanted layer with a lower index than the bulk substrate.

4.3.4 Refractive index profile of H^+ ion implantation

Since the He^+ experiments with ions showed that a decrease of the refractive index induced by electronic energy deposition in DAST is present, we selected an ion with an appropriate electronic energy loss profile to produce a refractive index barrier. The electronic energy deposition curves for He^+ and H^+ ions differ considerably in DAST, as it is evident by comparing Fig. 4.2 and Fig. 4.4, respectively. Whereas for He^+ ions it is similar to a diffusion-like profile with a maximum at the sample surface, the electronic deposition curve for H^+ ions has a similar shape as the nuclear energy deposition curve showing a peak at the end of the ion track, which would result in a refractive index barrier.

We employed a fluence of 1.25×10^{14} ions/ cm^2 to produce a refractive index barrier. The measured profile of the refractive index change Δn_1 is shown in Fig. 4.5 for wavelengths of

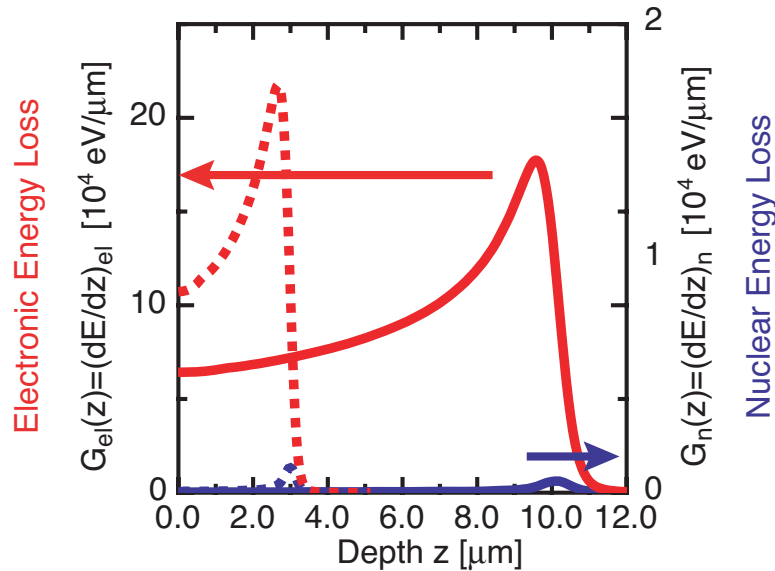


Figure 4.4: Energy deposition of H^+ ions. Nuclear (blue) and electronic (red) energy deposition curve of 1 MeV H^+ ions (full curve) in DAST calculated with SRIM. For reason of comparison, ordinate axes with the same order of magnitude as in Fig. 4.2 have been chosen. The dashed curves represent an ion energy of 450 keV and are given to show what for an impact the lowering of the ion energy has on the energy deposition profiles.

633 nm and 810 nm. Peak refractive index changes of around -0.2 at 633 nm ($n_1 = 2.69$) and -0.1 at 810 nm ($n_1 = 2.36$) were measured. The difference of these values in this small wavelength range can be attributed to the large dispersion of DAST since the wavelength of 633 nm is close to the absorption region. The solid curves in Fig. 4.5(a) and (b) are theoretical curves based on the model described in Section 4.3.1 with the following remarks. According to the results of He^+ implantation in DAST we can conclude that $\Delta n_{el} \gg \Delta n_n$ and therefore the nuclear contribution to the total index change can be neglected. Since for low fluences far below the saturation level the exponential term of $\Delta n_{el}(z)$ can be linearized, the parameters $\Delta n_{el,0}$ and $G_{el,0}$ cannot be independently modeled. Analysis showed that we are in the low fluence regime and therefore $G_{el,0}$ was fixed to $50 \times 10^{22} \text{ eV/cm}^3$. With this assumption we determined the parameters of Eq. (4.3) which correspond best to our experimental data. The results are listed in Table 4.1. In the low fluence regime the exponential factor describes the nonlinear relation between the refractive index change and deposited energy. Therefore, values of γ_{el} above 1 are desirable for the production of optical waveguides in order to have a clear distinction between the barrier region and the guiding layer combined with small refractive index changes in the waveguide core.

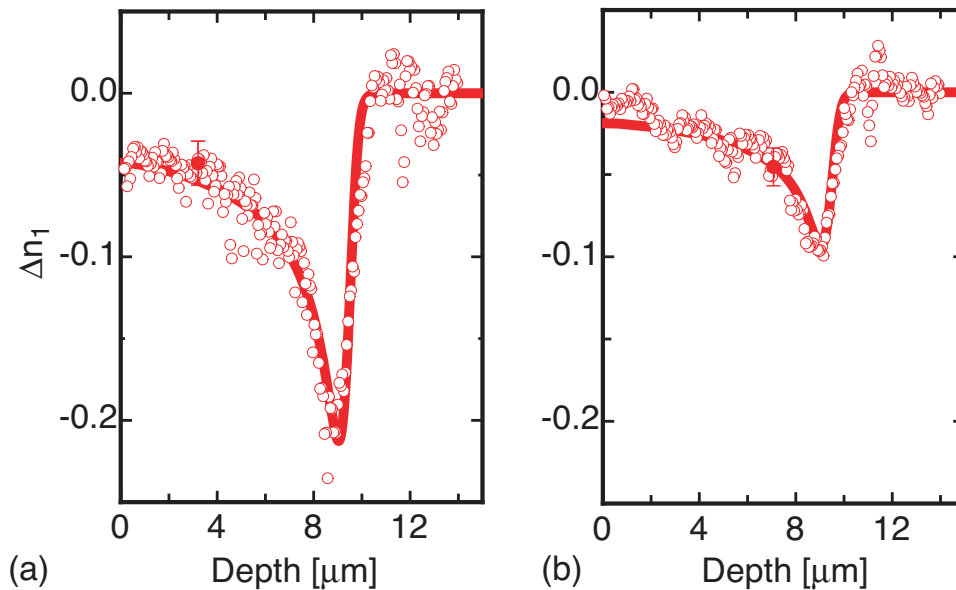


Figure 4.5: Refractive index change. Refractive index change of n_1 versus implantation depth z at the wavelength 633 nm (a) and 810 nm (b) for 1 MeV H^+ ion implantation in DAST with a fluence of $\phi = 1.25 \times 10^{14} \text{ ions/cm}^2$ measured with the reflection scan measurement method. The full curves are theoretical curves based on the theoretical model. The corresponding parameters are summarized in Table 4.1.

$\Delta n_{el,0}$ @ 633 nm	$\Delta n_{el,0}$ @ 810 nm	$G_{el,0}$ [10^{22} eV/cm ³]	γ_{el}	μ
0.94 ± 0.05	0.42 ± 0.03	50	1.68 ± 0.05	1.07 ± 0.05

Table 4.1: Model parameters of Eq. (4.3), which correspond best to the experimental data shown in Fig. 4.5 obtained by a least-square theoretical analysis.

4.4 Mode analysis

4.4.1 Barrier coupling method

In order to study the impact of the fluence on the refractive index profile, which is of great importance for a suitable waveguide tailoring, we employed implantations with three different fluences: 1.25×10^{14} ions/cm², 1.0×10^{14} ions/cm², and 0.5×10^{14} ions/cm². The mode profiles were measured with the recently developed barrier coupling method [75], which is more suitable for our organic crystal compared to prism coupling since no prism is required and the modes can be measured in a non contact configuration without applying pressure to the sample. A schematic illustration of the method is shown in Fig. 4.6(a).

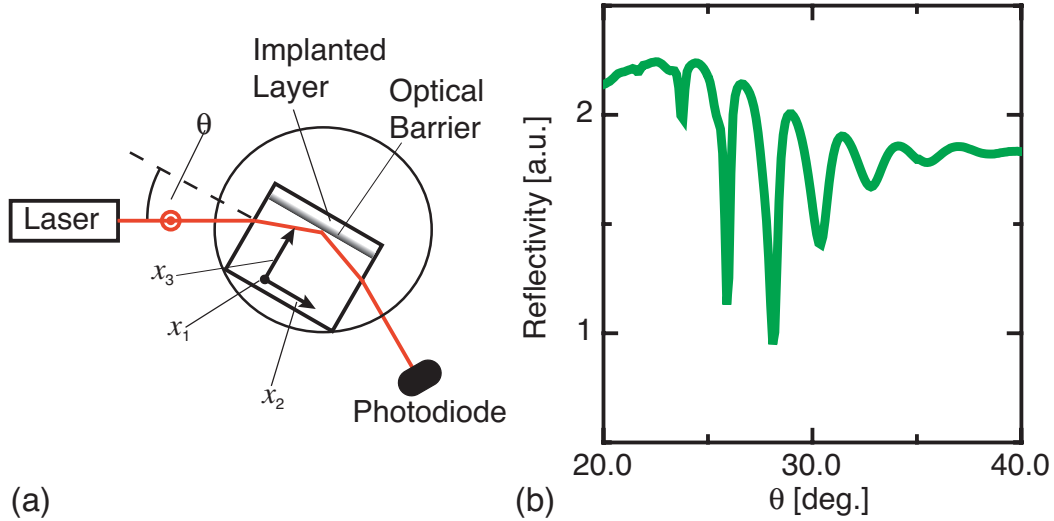


Figure 4.6: Mode measurement. (a) Experimental setup for the determination of the effective mode indices with the barrier coupling method. (b) Detected reflectivity as a function of the external angle θ at $\lambda = 850$ nm for light polarized along the dielectric x_1 axis. The DAST sample was implanted with 1 MeV H^+ ions with a fluence of 1.0×10^{14} ions/cm².

The method is based on frustrated total internal reflection on the waveguide barrier. The light beam with a vacuum wavenumber k_0 is coupled from the substrate with refractive index n_s to the waveguide core through the optical barrier. If the component of the wave-vector along the waveguide propagation direction x_2 of the beam $\beta = k_0 \sqrt{n_s^2 - \sin^2(\theta)}$ matches one

of the waveguide mode propagation constants $\beta = k_0 \cdot N_{\text{eff}}$, then the evanescent field of the reflected laser light is coupled to a waveguide mode. Coupling results in a dip in the reflection intensity. A measurement of the reflected light as a function of the external incident angle θ for a DAST sample implanted with 1 MeV H^+ ions with a fluence of 1.0×10^{14} ions/cm² is shown in Fig. 4.6(b). Eight TE modes for laser light polarized along the dielectric x_1 axis were detected. This measurement confirmed the creation of a waveguide by H^+ ion implantation.

4.4.2 Results

We compared the effective mode indices measured by the barrier coupling method with those stemming from the refractive index profiles obtained in Section 4.3.4 by the reflection scan method. These were calculated using a 2×2 matrix formalism [73]. The refractive index profiles for the three different fluences 1.25×10^{14} ions/cm², 1.0×10^{14} ions/cm² and 0.5×10^{14} ions/cm² obtained with the parameter summarized in Table 4.1 are shown in Fig. 4.7(a) and the corresponding effective mode indices in Fig. 4.7(b). The measured modes (o) and the calculated modes (full line) are in good agreement within the experimental error. The barrier

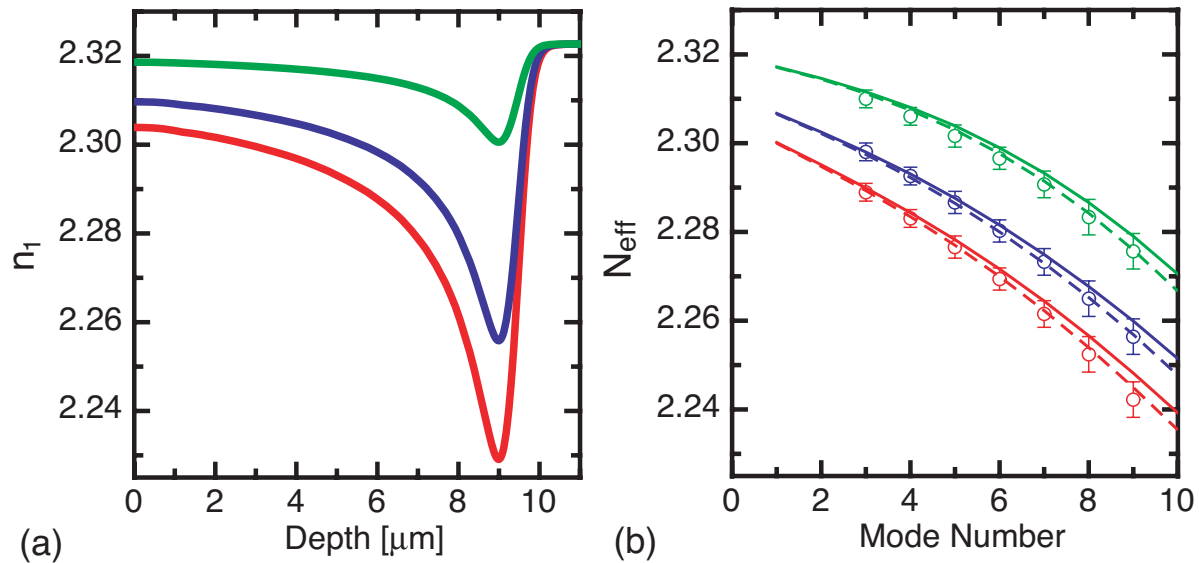


Figure 4.7: Effective indices. (a) Refractive index profiles at $\lambda = 850$ nm for fluences of 1.25×10^{14} ions/cm² (red), 1.0×10^{14} ions/cm² (blue), and 0.5×10^{14} ions/cm² (green) calculated with the parameters obtained with the reflection scan measurement method. (b) Corresponding calculated (full curve) and measured (o) effective mode indices N_{eff} ; the calculated modes indices are connected for clarity reasons. The dashed curves for the effective indices correspond best to the measured modes obtained by a reduction of the barrier position of about 5% compared to the depicted refractive index profiles in (a).

of the produced waveguides is thick, which is good to keep the losses low. However, the barrier coupling method cannot be used for modes with low tunneling losses and therefore the first two modes were not detectable as is visible by comparing the measured and calculated modes. Because of limited accuracy in the ion range predicted by SRIM, we varied the barrier position obtained by the reflection scan method ($\mu = 1.07 \pm 0.05$) within the experimental error. The dashed curves shown in Fig. 4.7(a) correspond the best to our experimental data and were obtained by assuming a reduced implantation depth of about 10% ($\mu = 1.11$) compared to SRIM calculations.

4.5 Waveguiding experiments

4.5.1 Planar waveguiding

After implantation the x_1x_3 end-faces were polished and waveguiding experiments performed by standard end-fire coupling. The light was propagating along the x_2 direction and was polarized parallel to the dielectric x_1 axis, which is the most interesting configuration for optical modulation in DAST in order to use the largest electro-optic coefficient r_{111} . The experimental setup is shown in Fig. 4.8(a). Waveguiding was clearly observed at wavelengths of 840 nm, 1315 nm, and 1570 nm. Figure 4.8(b) shows a photograph of the end-face as taken with the infrared camera of the setup with light coupled at 1570 nm.

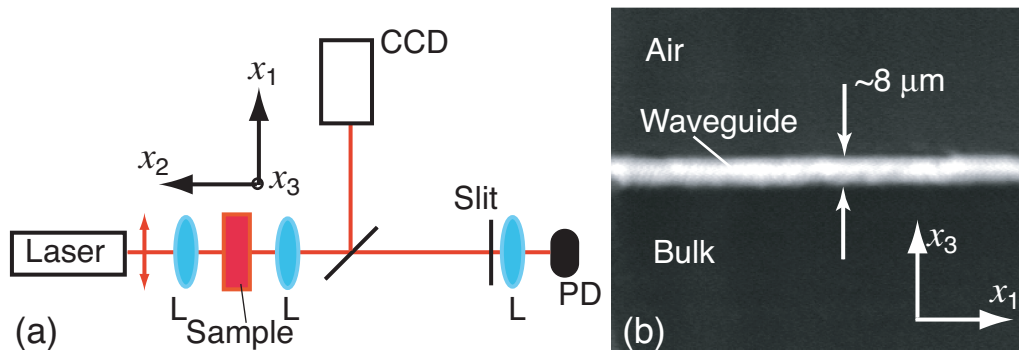


Figure 4.8: Waveguide coupling. (a) Experimental setup for the determination of the waveguiding characteristics and loss determination: L: lens, CCD: infrared camera, PD: photodiode. (b) Photograph of the end-face of the crystal taken with the CCD camera. The cross section of the planar guided light at 1570 nm is clearly visible.

The losses of the planar waveguide structures were determined by measuring the power of the guided light transmitted through the waveguide with the setup shown in Fig. 4.8 at $\lambda = 1.57 \mu\text{m}$. The guided light was collected with two lenses and detected with a photodiode. Special care was taken to only detect the guided light. Therefore, the polished end-face of the

crystal sample was imaged onto a horizontal slit that was aligned so that only the guided light could be transmitted. For an assumed coupling efficiency of 80%, the losses were 7 ± 2 dB/cm for the waveguide produced by the ion fluence of 1.0×10^{14} ions/cm² and about 10 dB/cm for two other waveguides. The contribution of bulk material absorption is about 2.5 dB/cm at $1.57 \mu\text{m}$. At the present state it is not clear if the slightly increased losses for lower 0.5×10^{14} ions/cm² and higher 1.25×10^{14} ions/cm² fluences are related to higher tunneling losses or defect concentration or to a reduced edge quality and therefore lower coupling efficiency.

4.5.2 Channel waveguiding

Channel waveguides were then produced by standard photolithography. The detailed structuring procedure is described in Appendix C. The ridges had a height of about $3.5 \mu\text{m}$. At the present stage, coupling of light at a wavelength of $1.55 \mu\text{m}$ was achieved for waveguide widths from 10 to $60 \mu\text{m}$. A photograph of the mode profile as observed at the out-coupling face is depicted in Fig. 4.9. The edge quality was not sufficient to efficiently couple waveguides with smaller widths. At the moment we are working on improving the sharp edge polishing in order to also couple light into waveguides with smaller dimensions.

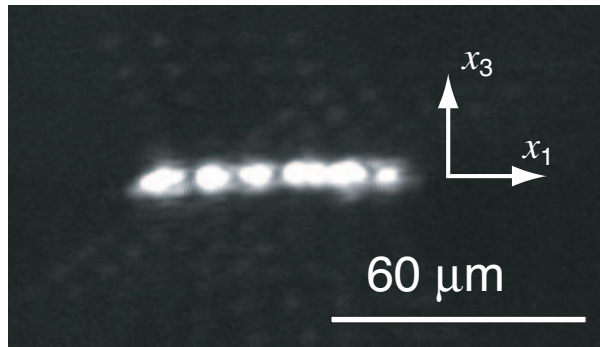


Figure 4.9: Ridge waveguiding. Photograph of the out-coupling face of a ridge waveguide with a width of $W = 60 \mu\text{m}$. The light was propagating along the x_2 direction and was polarized parallel to the x_1 direction.

4.6 Conclusions

In conclusion, we have realized optical waveguides in the organic crystal DAST by H^+ ion implantation. Waveguiding with losses of 7 dB/cm at $1.57 \mu\text{m}$ has been achieved in planar waveguides and subsequently first channel waveguides have been produced by standard photolithography. We have shown that the main refractive index changes in the organic crystal DAST are due to changes in the molecular structure and are caused by the electronic excitations. This result is a new and unexpected finding and completely different from inorganic

materials, for which the origins of the refractive index change are ion induced nuclear displacements. Therefore the work gives new perspectives for the use of ion implantation in integrated optics, being for the first time successfully applied to organic crystals. Refractive index changes in the barrier region of up to -0.1 at 810 nm have been observed at relatively low fluences of the order of 10^{14} ions/cm². We have determined the refractive index profile as a function of the H⁺ ion fluence by measuring the reflectivity of a wedged-polished sample and confirmed by measuring the effective mode indices by the barrier coupling method. Using these data the effect of ion implantation could be accurately described with a model. Since the waveguide thickness can be tailored by the implantation process within a few tens of micrometers, an important first step towards integrated optics in DAST has been made.

Chapter 5

Nonlinear optical properties of ion implanted DAST waveguides [§]

We report on the electro-optic and nonlinear optical properties of waveguides produced by low fluence ($\phi = 1.25 \times 10^{14}$ ions/cm²) H⁺ ion implantation in the organic nonlinear optic crystal DAST. The profile of the nonlinear optical susceptibility has been determined by measuring the reflected second-harmonic generation efficiency from a wedged-polished sample at a fundamental wavelength of $\lambda_\omega = 1176$ nm. In the waveguide core region the nonlinear optical susceptibility is shown to be preserved to more than 90% of its bulk value. A model which relates the molecular changes to the measured macroscopic alteration of the refractive index and the nonlinear coefficient has been introduced to quantify the fraction of molecules modified by ion implantation. Furthermore, a first electro-optic modulation in ion implanted DAST waveguides has been demonstrated.

5.1 Introduction

Ion implantation is used in a variety of inorganic materials to produce optical waveguide structures [73,76]. Recently, it has also been applied to the organic nonlinear optic crystal DAST, in which planar optical waveguides have been successfully realized by light ion implantation [69]. A barrier layer with a reduced index of refraction was formed a few micrometers below the surface by low fluence irradiation of 1 MeV H⁺ ions, and thus confinement of light was ensured in the core layer between sample surface and barrier.

DAST (4-N, N-dimethylamino-4'-N'-methyl-stilbazolium tosylate) is an organic crystal with outstanding nonlinear optical properties, e.g. a second-order nonlinear optical coefficient ($d = \chi^{(2)}/2$) $d_{111} = 1010 \pm 110$ pm/V at a fundamental wavelength of 1318 nm, and $d_{111} = 210 \pm 55$ pm/V at 1907 nm [42]. Furthermore, the combination of a low dielectric constant of $\epsilon_{11} = 5.2$

[§]This chapter has been submitted to Optics Express.

with a high electro-optic figure of merit, $n_1^3 r_{111} = 1030 \pm 110$ pm/V at 800 nm, and $n_1^3 r_{111} = 455 \pm 80$ pm/V at 1535 nm, are rendering it highly attractive for high-speed electro-optic applications [28].

To use ion implanted waveguides for active integrated photonic devices, it is of main importance to maintain the high nonlinear optical properties in the waveguide region. In inorganic nonlinear optical active crystals such as KNbO_3 or LiNbO_3 , a reduction of the nonlinear optical properties below 50% of its bulk value was observed upon implantation [77, 78]. With thermal annealing and subsequent repoling the optical nonlinearity was recovered to more than 90% of the bulk value [77]. In organic nonlinear optical crystals, the origins of the refractive index change by ion implantation are electronic excitations [69], and are therefore essentially different compared to inorganic crystals, in which the refractive index changes due to ion induced nuclear displacements. The influence of ion implantation on the nonlinear optical properties of organic crystals has not been investigated yet.

In this work we present our results on the measured nonlinear optical susceptibility profile of H^+ implanted waveguides in DAST. We introduce a model that relates microscopic material changes to the observed alteration of the nonlinear optical susceptibility. Furthermore, we report on the first electro-optic modulation experiments in the produced waveguide structures.

5.2 Ion implanted waveguides in DAST

The DAST single crystals used in our experiments were grown from supersaturated methanol solution by the temperature-lowering method [44]. DAST has a monoclinic point-group symmetry m with its mirror plane normal to the b axis. The crystallographic x_1 and x_3 axes coincide almost with the crystallographic a and c axis, respectively [63]. The grown crystals were cut approximately along the dielectric axes and the $x_1 x_2$ surface was polished to $\lambda/4$ quality. The typical sample size was about $7 \times 4 \times 4$ mm³ with the longest dimension along x_1 .

The $x_1 x_2$ sample surface was then irradiated with 1 MeV H^+ ions with a fluence of $\phi = 1.25 \times 10^{14}$ ions/cm². In order to reduce the penetration depth of the ions, the samples were tilted by 60° from normal incidence, resulting in an induced refractive index barrier at a depth of about 9 μm . The ion current was kept at 40 nA and scanned over an area of 9×9 mm² to avoid thermal damage to the samples.

We have previously shown that using these implantation parameters a refractive index barrier suitable for waveguiding is formed with a peak refractive index change of $\Delta n_1 = -0.1$ at a probing wavelength of 810 nm [69]. The refractive index profile at this wavelength was measured by detecting the reflected light from a wedged-polished sample surface and the corresponding effective mode indices were determined by the barrier coupling method [75]. By conventional end-fire coupling waveguiding at telecommunication wavelength was demonstrated with measured waveguide losses of about 7 dB/cm.

The study of the fundamental waveguide properties at $\lambda = 1.55$ μm (refractive index as

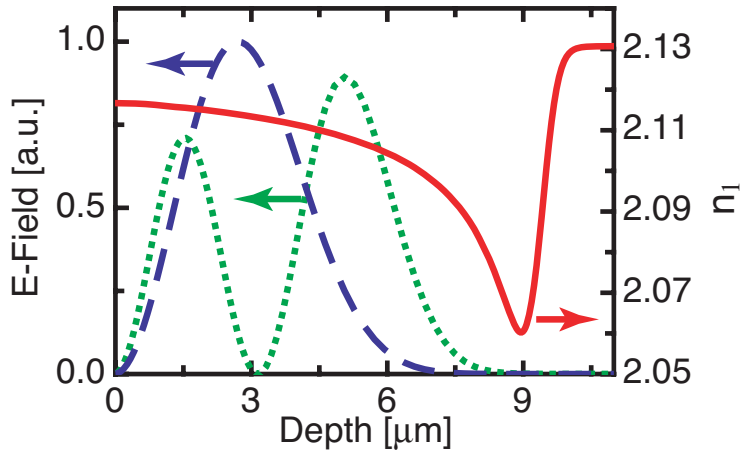


Figure 5.1: Refractive index profile and modes at 1.55 μm . Refractive index profile of ion implanted DAST waveguides at a wavelength of 1.55 μm (solid curve) for an ion fluence of $\phi = 1.25 \times 10^{14}$ ions/cm², and corresponding electric field amplitude of the first (dashed curve) and second mode (dotted curve), which have calculated tunneling losses of below 1 dB/cm.

well as waveguide mode profiles) is of significant importance concerning the use of DAST for high-speed optical modulators and switches in telecommunication.

With help of the previously obtained refractive index data at 810 nm [69] and the model described in detail in Section 5.4.1, the refractive index profile at a wavelength of 1.55 μm was obtained. Figure 5.1 shows the refractive index profile with the corresponding electric field distributions of the first and second TE mode, whose effective indices were calculated to be $n_{\text{eff},1} = 2.111$ and $n_{\text{eff},2} = 2.102$, respectively, by using a 2×2 matrix formalism [73]. The tunneling losses were determined with help of the width of the resonance peaks obtained by the matrix formalism [79] and are below 1 dB/cm for the modes depicted. Higher order modes show tunneling loss estimates of over 10 dB/cm. Therefore the produced waveguide can be considered to be bimodal.

5.3 Second-harmonic reflection measurement

In order to determine the change of the nonlinear optical susceptibility as a function of the implantation depth, the reflected second-harmonic generated light from a wedged-polished sample surface was measured. To increase the resolution of the measurement, the sample was polished under an angle of 1° as shown in Fig. 5.2. The output of an optical parametric generator/amplifier OPG/OPA (Quantronix, TOPAS), which was pumped with a Ti:sapphire laser providing 160 fs pulses at a center wavelength of 776 nm with a repetition rate of 1 kHz, was then focused on the sample surface to a diameter of less than 10 μm . The sample was scanned in η direction with a step size of 10 μm leading to a depth resolution of about 0.2 μm in z

direction. Signal distortions due to polishing imperfections were reduced by averaging over 19 scans taken at different positions. A fundamental wavelength of $\lambda_\omega = 1176$ nm was chosen so that the second-harmonic generated light at $\lambda_{2\omega} = 588$ nm was within the visible absorption band of DAST [63]. Therefore, only the second-harmonic generated light at the sample surface was observed and any substrate contributions were eliminated [77]. The polarization of the fundamental beam was parallel to the x_1 direction.

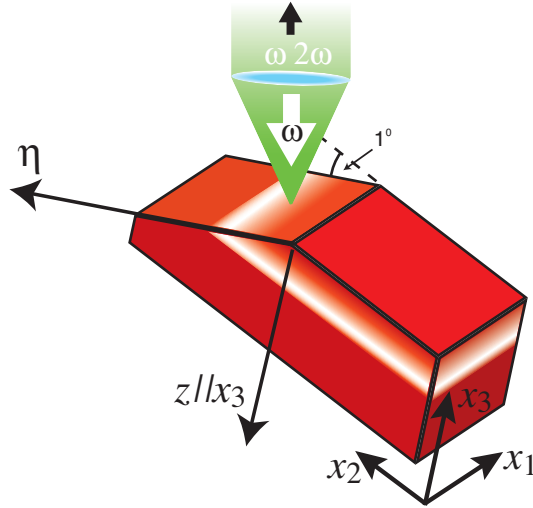


Figure 5.2: SHG back reflection measurement. Experimental setup for measuring the depth profile of the nonlinear optical susceptibility. The second-harmonic light generated on a wedged sample surface is measured while the sample is scanned in η direction. The profile as a function of the implantation depth z is finally obtained by a projection of the η to the z direction.

A light beam impinging on an interface between a linear and a nonlinear optical active medium will result in a second-harmonic reflected wave. For normal incidence the existence of a second-harmonic reflected wave can be explained with the boundary conditions that require continuous tangential electric and magnetic field components. Since in the nonlinear medium waves with second-harmonic frequency exist, the boundary condition can only be fulfilled with the presence of a back reflected second-harmonic wave. For normal incidence the second-harmonic reflected field component $E_{2\omega}^R$ at an interface between a linear and a nonlinear optical active medium is related to the induced nonlinear polarizability $P_{2\omega}^{\text{NLS}}$ in the active medium by [8]

$$E_{2\omega}^R = \frac{1}{\epsilon_0} \frac{P_{2\omega}^{\text{NLS}}}{(n_{2\omega} + 1)(n_{2\omega} + n_\omega)} = \frac{d_{111} t_\omega^2 E_\omega^2}{(n_{2\omega} + 1)(n_{2\omega} + n_\omega)}, \quad (5.1)$$

where n_ω and $n_{2\omega}$ are the refractive indices along the x_1 axis of DAST at the fundamental and second-harmonic frequencies, respectively. E_ω is the incident electric field in air, $t_\omega = 2/(n_\omega + 1)$ the transmission factor for the electric field amplitude E_ω , d_{111} the tensor element of the nonlinear optical susceptibility tensor $d_{ijk} = \frac{1}{2}\chi_{ijk}^{(2)}$, and ϵ_0 the dielectric permittivity of free

space. The back reflected light was deflected on a beamsplitter and measured with a photo avalanche diode. We ensured that only the second-harmonic intensity was detected by inserting a band pass and an interference filter, which were blocking the fundamental beam, in the beam path between the beamsplitter and the photo diode.

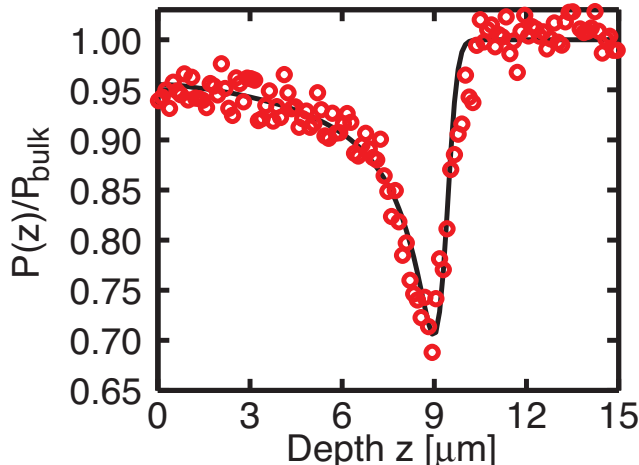


Figure 5.3: Normalized second-harmonic power at $\lambda_{2\omega} = 588 \text{ nm}$. Measured normalized second-harmonic power of an implanted DAST waveguide as a function of the implantation depth z at a second-harmonic wavelength of $\lambda_{2\omega} = 588 \text{ nm}$. The open circles represent the measured data points. The full curve is a guide to the eye.

The measured second-harmonic generated power as a function of the depth z normalized by its bulk value is shown in Fig. 5.3. In the waveguide core region a reduction of the normalized power of less than 10% was present, whereas within the barrier layer the signal dropped to about 70% of the bulk value of the virgin crystal.

5.4 Ion-induced modification of linear and nonlinear optical properties in organic media

5.4.1 Model

Since the quantity of interest is the change of the nonlinear optical susceptibility after implantation, we introduce a model which relates the microscopic and macroscopic properties to the measured second-harmonic power. With help of this model the nonlinear susceptibility d_{ijk} as well as the number of modified molecules will be calculated.

The microscopic linear polarizability $\alpha(\omega)$ at frequency ω and the first-order hyperpolarizability $\beta(-2\omega, \omega, \omega)$ at the fundamental frequency ω are related to the refractive index n and

nonlinear susceptibility d by [6]

$$n_{\omega}^2 - 1 = N f_{\omega} \alpha(\omega) \quad (5.2)$$

$$d = \frac{1}{2} N f_{\omega}^2 f_{2\omega} \beta(-2\omega, \omega, \omega), \quad (5.3)$$

where N is the number of molecules per volume and $f_{\omega, 2\omega} = (n_{\omega, 2\omega}^2 + 2)/3$ are Lorentz local field factors.

After implantation, some nonlinear optical chromophores of the implanted DAST crystals will be modified. This leads to a reduction of the molecular polarizability α and the first-order hyperpolarizability β and hence to an alteration of the macroscopic material properties n and d . The polarizability $\tilde{\alpha}$ of the modified molecules can be described by

$$\tilde{\alpha}(\omega) = k_{\omega} \alpha(\omega), \quad (5.4)$$

where k_{ω} is the percentage of remaining polarizability of the modified molecule. If we assume that the first order hyperpolarizability of the modified molecules $\tilde{\beta}$ is

$$\tilde{\beta}(-2\omega, \omega, \omega) \ll \beta(-2\omega, \omega, \omega), \quad (5.5)$$

we obtain for the refractive index $\tilde{n}_{\omega}(z)$ and the nonlinear susceptibility $\tilde{d}(z)$ of the implanted material

$$\tilde{n}_{\omega}^2(z) - 1 = N p(z) \tilde{f}_{\omega}(z) \alpha(\omega) + N [1 - p(z)] \tilde{f}_{\omega}(z) \tilde{\alpha}(\omega) \quad (5.6)$$

$$\tilde{d}(z) \approx \frac{1}{2} N p(z) \tilde{f}_{\omega}^2(z) \tilde{f}_{2\omega}(z) \beta(-2\omega, \omega, \omega), \quad (5.7)$$

where $p(z)$ is the percentage of unmodified chromophores at the depth z . Dividing Eq. (5.7) by Eq. (5.3), we obtain for the percentage of unmodified molecules

$$p(z) = \frac{\tilde{d}(z)}{d_{\text{bulk}}} \frac{f_{\omega}^2 f_{2\omega}}{\tilde{f}_{\omega}^2(z) \tilde{f}_{2\omega}(z)}. \quad (5.8)$$

With help of Eq. (5.1) the following relation can be derived for the normalized susceptibility profile $\tilde{d}(z)/d_{\text{bulk}}$

$$\frac{\tilde{d}(z)}{d_{\text{bulk}}} = \sqrt{\frac{P(z)}{P_{\text{bulk}}}} \frac{[\tilde{n}_{2\omega}(z) + 1][\tilde{n}_{2\omega}(z) + \tilde{n}_{\omega}(z)]}{[n_{2\omega} + 1][n_{2\omega} + n_{\omega}]} \frac{t_{\omega}^2}{\tilde{t}_{\omega}^2(z)}, \quad (5.9)$$

where $P(z)/P_{\text{bulk}}$ is the measured normalized power depicted in Fig. 5.3. Therefore, if the refractive index profiles $\tilde{n}_{2\omega}(z)$ and $\tilde{n}_{\omega}(z)$ are known, the normalized susceptibility profile $\tilde{d}(z)/d_{\text{bulk}}$ can be calculated. Subsequently also the percentage of unmodified molecules $p(z)$ given by Eq. (5.8) can be determined, since the local field factors are only dependent on the refractive index profile data.

5.4.2 Susceptibility profile

The refractive index profiles for our implantation parameters at a wavelength of 633 nm and 810 nm are given in Ref. [69]. The one at 633 nm was extrapolated to the wavelength of the second-harmonic light at 588 nm and the profile at 810 nm was used to obtain the corresponding refractive index profile data at the fundamental wavelength of 1176 nm with the following procedure.

With help of Eqs. (5.2), (5.4) and (5.6), $p(z)$ can be written as

$$p(z) = \frac{\frac{\tilde{n}_\omega^2(z)-1}{\tilde{n}_\omega^2(z)+2} \frac{n_\omega^2+2}{n_\omega^2-1} - k_\omega}{1 - k_\omega}. \quad (5.10)$$

Since the percentage of unmodified molecules $p(z)$ is independent of the wavelength, the refractive index profile $\tilde{n}_{\omega'}(z)$ at the frequency ω' can be calculated with help of the following equation

$$\frac{\frac{\tilde{n}_\omega^2(z)-1}{\tilde{n}_\omega^2(z)+2} \frac{n_\omega^2+2}{n_\omega^2-1} - k_\omega}{1 - k_\omega} = \frac{\frac{\tilde{n}_{\omega'}^2(z)-1}{\tilde{n}_{\omega'}^2(z)+2} \frac{n_{\omega'}^2+2}{n_{\omega'}^2-1} - k_{\omega'}}{1 - k_{\omega'}}. \quad (5.11)$$

Assuming that $k_\omega \approx k_{\omega'}$, the refractive index profiles $\tilde{n}_\omega(z)$ and $\tilde{n}_{2\omega}(z)$ were calculated with help of the refractive index data at 633 nm and 810 nm and the reported bulk refractive indices of $n_\omega = 2.18$ at 1176 nm [28] and $n_{2\omega} = 3.10$ at a wavelength of 588 nm [63].

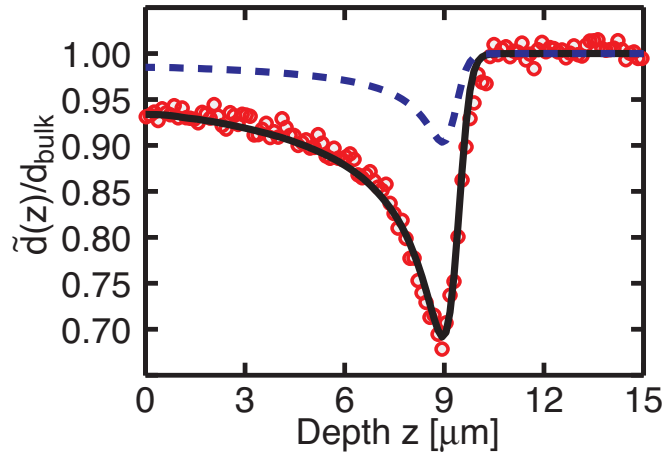


Figure 5.4: Normalized susceptibility profile at $\lambda_{2\omega} = 588$ nm. Open circles represent the normalized susceptibility profile of a waveguide structure produced by 1 MeV H^+ implantation with a fluence of $\phi = 1.25 \times 10^{14}$ ions/cm². The full curve corresponds best the theoretical model based on Eq. (5.12). The dashed curve is the ratio of unmodified molecules calculated with Eq. (5.8).

Figure 5.4 shows the normalized susceptibility profile (open circles) obtained from the measured $P(z)/P_{\text{bulk}}$ data using Eq. (5.9). Note the similarity of the amplitudes of the normalized measured power (Fig. 5.3) to the one of the susceptibility profile (Fig. 5.4). As substantiated

in Eq. (5.9), the normalized susceptibility profile is proportional to the square root of the normalized measured power. Taking also into account the reduction of the refractive index in the implanted region, which is usually neglected when analyzing induced waveguides, we obtained the described amplitude similarity. The percentage of unmodified molecules $p(z)$ is represented by a dashed curve as calculated with Eq. (5.8). At the peak position about 10% of the molecules were modified.

To describe the nonlinear susceptibility profile as a function of the deposited energy, we have chosen a model analogous to the one used for the refractive index change, in which the deposited energy was related to the induced refractive index change [69]. Hence, the relative change in the nonlinear susceptibility is given by

$$\frac{\Delta\tilde{d}(z)}{d_{\text{bulk}}} = \frac{\Delta d_{\text{max}}}{d_{\text{bulk}}} \left[1 - e^{-\left(\phi \frac{G_{el}(\mu z)}{G_{el,0}}\right)^{\gamma_{el}}} \right], \quad (5.12)$$

where Δd_{max} is the maximal change in d . $G_{el,0}$ is a normalization energy term and γ_{el} is an exponential factor. G_{el} represents the deposited energy as calculated with Srim [69] and the factor μ accounts for the limited precision in the prediction of the ion range by Srim. The full curve in Fig. 5.4 corresponds best to the experimental data obtained by least-squares theoretical analysis. The obtained parameters are summarized in Table 5.1 with the following remarks. For the analysis $\Delta d_{\text{max}}/d_{\text{bulk}}$ was fixed to -1 , since (i) for very high fluences all molecules should be modified and therefore the second-order nonlinear activity of the material lost, and (ii) we are in a low fluence regime as mentioned in Ref. [69], therefore the parameters $G_{el,0}$ and $\Delta d_{\text{max}}/d_{\text{bulk}}$ are not independent from each other. Moreover, the factor μ was fixed to the value obtained by the refractive index profile analysis [69]. The theoretical curve in Fig. 5.4 describes the data (open circles) reasonable well.

$\Delta d_{\text{max}}/d_{\text{bulk}}$	$G_{el,0}$ [10^{22} eV/cm ³]	γ_{el}	μ
-1	41 ± 5	1.66 ± 0.3	1.07

Table 5.1: Model parameters of Eq. (5.12), which correspond best to the experimental data shown in Fig. 5.4 obtained by a least-square theoretical analysis.

5.5 Electro-optic modulation

A first electro-optic modulation in the produced ion implanted planar waveguide structures was demonstrated with the experimental configuration shown in Fig. 5.5. The laser output at a wavelength of $1.55 \mu\text{m}$ was coupled into the waveguides by conventional end-fire coupling. The propagation direction of the guided light was along the dielectric x_2 direction and its polarization was parallel to x_1 . To detect the phase modulation of the guided signal, an external reference arm was set up. The resulting interference pattern was widened up with a lens and the central part of one fringe was selected with an aperture, which was placed in front of the photodiode.

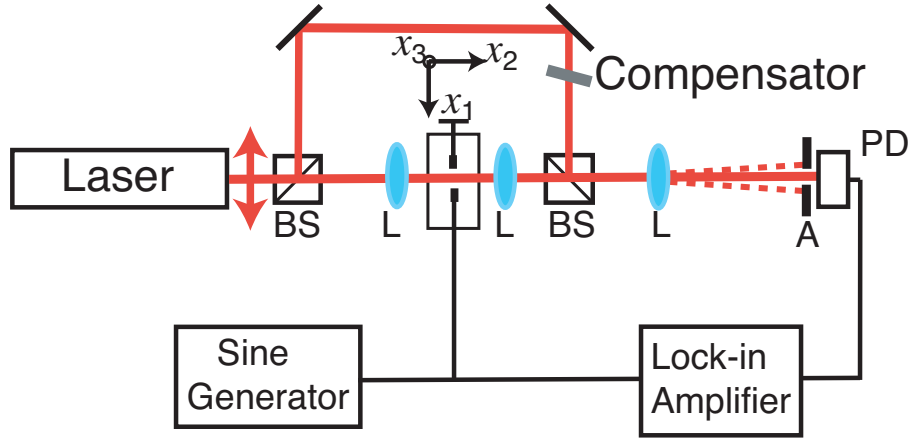


Figure 5.5: Setup for electro-optic measurement. Experimental setup with reference arm for electro-optic modulation. BS: beamsplitter, L: lens, A: aperture, PD: photodiode.

The spacing between the gold electrodes with a thickness of about 70 nm was relatively large ($D = 2$ mm). To maximize the modulator response, the phase shift between the two arms was adjusted using a compensator. The resulting linear amplitude modulation was measured with a lock-in amplifier. From the modulation depth the electro-optic coefficient was determined with help of the following equations. The induced phase shift $\Delta\varphi$ is related to the electro-optic coefficient r_{111} for an electric field applied along the x_1 direction by [6]

$$\Delta\varphi = \frac{\pi r_{111} n_1^3 L_o}{\lambda D} U, \quad (5.13)$$

where n_1 is the refractive index, L_o the interaction length between the optical beam and the applied electric field and U the applied voltage to the electrodes. The interaction length was $L_o = 1.9$ mm and we applied sinusoidal modulation voltages with amplitudes of up to 10 V. The amplitude of the measured intensity modulation δI is related to the electro-optic coefficient by [6]

$$\delta I = \frac{I_{\max} - I_{\min}}{2} \frac{\pi r_{111} n_1^3 L_o}{\lambda D} \delta U, \quad (5.14)$$

where I_{\max} and I_{\min} are the maximal and minimal intensities measured by changing the optical length of the interference arm and δU is the amplitude of the applied modulation voltage. We obtained $r_{111} = 41 \pm 10$ pm/V at a modulation frequency of 2 kHz, which is about 12% lower compared to the bulk value of 47 ± 8 pm/V [28]. The waveguide structures realized by 1 MeV ion implantation are supporting two well confined modes (see Fig. 5.1), consequently the measured reduction may be partly attributed to interference effects between these two modes.

5.6 Conclusions

We have determined the nonlinear optical properties of ion implanted waveguides in the organic crystal DAST by reflection second-harmonic generation measured from a wedged-polished sample. The planar waveguide structures investigated have been produced by H^+ ion implantation with a fluence of 1.25×10^{14} ions/cm². The measurements showed that the nonlinear optical susceptibility is preserved to more than 90% of the bulk value in the waveguide core region. A model that relates the microscopic material changes with the measured macroscopic properties has been introduced. The fraction of modified molecules after implantation has been determined with help of this model. In the barrier region less than 10% of the molecules are modified. In addition, a first electro-optic modulation in the planar waveguide structures has been demonstrated. We believe these results constitute an important step towards the utilization of organic nonlinear optical active crystals in integrated devices for telecommunication applications.

Chapter 6

Direct electron beam writing of DAST channel waveguides [§]

We report on optical channel waveguiding in an organic crystalline waveguide produced by direct electron beam patterning. The refractive index profile as a function of the applied electron fluence has been determined by a reflection scan method in the nonlinear optical organic crystal 4-N, N-dimethylamino-4'-N'-methyl-stilbazolium tosylate (DAST). A maximal refractive index reduction of $\Delta n_1 = -0.3$ at a probing wavelength of 633 nm has been measured for an electron fluence of 2.6 mC/cm². Furthermore, a new concept of direct channel waveguide patterning in bulk crystals is presented and waveguiding has been demonstrated in the produced structures by end-fire coupling. Mach-Zehnder modulators have been successfully realized and a first electro-optic modulation at a wavelength of $\lambda = 1.55 \mu\text{m}$ has been demonstrated therein.

6.1 Introduction

Organic noncentrosymmetric materials have recently attracted much attention for applications in photonic devices because of their almost unlimited design possibilities to tailor the linear and nonlinear optical properties and the fact that the nonlinear active organic molecules, embedded either in a polymer matrix or orderly packed in a crystal, show an almost pure electronic origin of their nonlinearities [26, 27, 30]. Therefore, organic nonlinear optical materials are very interesting and promising for high-speed electro-optic applications in future telecommunication networks. In contrast to the more widely studied electro-optic poled polymers, organic crystals offer the advantages of superior photochemical stability and potentially higher nonlinearities. Furthermore, in organic crystals no thermal relaxation of the chromophores is present since they are embedded in a crystalline structure, whereas poled polymers often tend to lose their electro-optic activity due to thermal relaxation of the oriented chromophores. Nevertheless,

[§]This chapter has been accepted for publication in Optics Express.

thin film growth and processing of organic crystals is still very challenging.

DAST (4-N, N-dimethylamino-4'-N'-methyl-stilbazolium tosylate) is a widely investigated nonlinear optical active organic crystal with high electro-optic coefficients $r_{111} = 77 \pm 8$ pm/V at 800 nm and $r_{111} = 47 \pm 8$ pm/V at 1535 nm, combined with a low dielectric constant $\epsilon_{11} = 5.2$ [28, 41, 56]. Hence it is a very interesting candidate for high-speed electro-optic applications. Thus different techniques for waveguide fabrication have been investigated in this material, including ion implantation [69], photobleaching [60, 63], photolithography [60], fs laser ablation [61], graphoepitaxial melt growth [62] and thin film solution growth [47, 55].

In this work we exploit the process of direct electron beam (e-beam) patterning of DAST. E-beam direct structuring has already been used to create channel waveguides in silica, in which the refractive index was increased in the exposed area [80, 81]. On the contrary, for the organic nonlinear optical crystal AANP a decrease of the refractive index has been recently observed by e-beam irradiation [82], but no waveguiding configuration has been suggested yet.

We present our results on channel waveguide patterning in organic nonlinear optical bulk crystals by electron beam exposure, which is offering several advantages over previously reported structuring techniques. Using this method, channel waveguides can be directly patterned in a single process step and the waveguide dimensions can be precisely tailored to attain single mode waveguiding, which is a prerequisite for efficient electro-optic devices. Since no mechanical or chemical etching is required as compared to standard photolithography, the produced channel waveguides have smoother side walls. Furthermore, e-beam exposure offers the benefit of submicrometer resolution.

In the first part of this work we show that the refractive index of the DAST area irradiated with electrons is reduced and we introduce a simple model that relates the induced refractive index change with the deposited energy of the electrons. Then we propose a new concept of channel waveguide patterning in a single process step in bulk crystals, which is used to successfully realize channel waveguides and Mach-Zehnder modulator structures. Furthermore, a first demonstration of electro-optic modulation in these structures is described.

6.2 Electron beam experiments

DAST belongs to the monoclinic point group m [28]. The crystallographic b axis and the dielectric x_2 axis are normal to the mirror plane, and the x_1 axis makes an angle of 5.4° to the polar a axis in the symmetry plane [63]. The noncentrosymmetric crystal packing is achieved by strong Coulomb interactions between the positively charged, nonlinear optical chromophore stilbazolium and the negatively charged counter ion tosylate, which are shown in Fig. 6.1 [41]. The samples used in our experiments were grown from supersaturated methanol solution by the temperature-lowering method [28]. The crystals were then cut almost perpendicular to the dielectric axes and the x_1x_2 surface polished to $\lambda/4$ surface quality. The typical sample size was about $7 \times 4 \times 4$ mm³ with the longest dimension along x_1 . The samples were protected

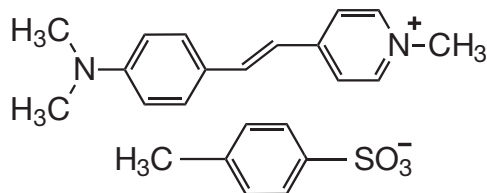


Figure 6.1: Molecular units of DAST. The positively charged, nonlinear optical chromophore stilbazolium and the negatively charged tosylate.

with a 150 nm thick polyvinylacetate (PVAc) layer and then covered with 20 nm Cr in order to prevent the sample from charging up during the electron beam exposure. For direct patterning the structures were exposed with a Raith electron beam system with an electron energy of 30 keV and a relatively low electron current of 0.3 nA to avoid thermal damage of the samples. After the exposure, the Cr layer was removed by Ar^+ sputtering and the PVAc layer, which protects DAST from Cr indiffusion during the sputtering, is dissolved in toluene.

6.3 Refractive index profile induced by e-beam exposure

6.3.1 Model for e-beam exposure

To describe the refractive index change induced by electron beam exposure, we have chosen a model analogous to the one used for H^+ implanted samples [69], in which the induced refractive index change was related to the deposited energy of the implanted ions in an organic crystal.

The energy deposition of electrons in DAST was calculated with the Monte Carlo simulation tool for electron trajectory in solids CASINO (www.gel.usherbrooke.ca/casino/). Figure 6.2

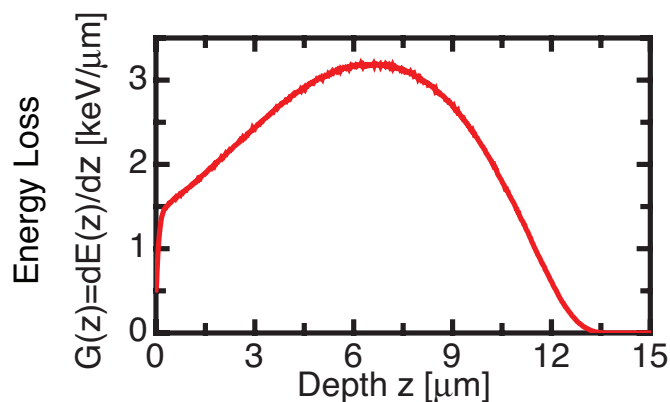


Figure 6.2: Deposited energy. Deposited energy in DAST as a function of the electron depth z for an electron energy of 30 keV and homogenous e-beam exposure as calculated by CASINO.

shows the deposited energy per electron $G(z) = dE(z)/dz$ as a function of the electron penetration depth z for an electron energy of 30 keV and a homogeneous e-beam exposure. A maximal energy deposition occurs at a depth of about $7 \mu\text{m}$.

The phenomenological relation between the induced refractive index change Δn and the stored energy is given by [69]

$$\Delta n(z) = \Delta n_{\text{max}} \left[1 - e^{-\left(\phi \frac{G(z)}{G_0}\right)^\gamma} \right], \quad (6.1)$$

where Δn_{max} is the saturation refractive index change, ϕ represents the electron fluence, G_0 is a normalization energy and γ an exponential factor. Note that for high electron fluences the expression tends to the saturation refractive index change Δn_{max} .

6.3.2 Reflection scan measurement method

The parameters Δn_{max} , G_0 , and γ in Eq. (6.1) are material depended and were determined with the following experiment. In a first step ten lines of $30 \mu\text{m}$ width were written with linearly increasing fluences from 0.26 mC/cm^2 up to 2.6 mC/cm^2 . The sample was then polished under a wedge of 1° in order to increase the spatial resolution in z direction as shown in Fig. 6.3.

The refractive index at the polished surface was determined by measuring the back reflected light from the sample surface [72]. The refractive index n is related to the intensity reflection

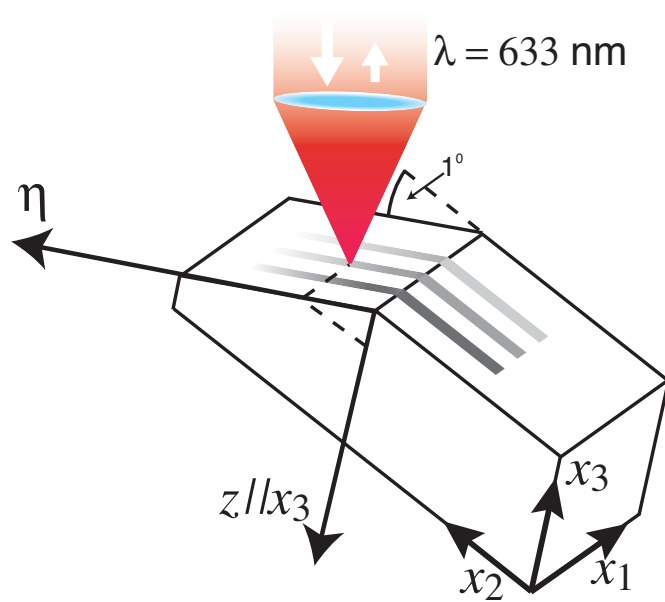


Figure 6.3: Reflection scan setup. Experimental configuration for the determination of the refractive index profile by measuring the back reflected light from a wedged-polished sample surface. The electron beam patterned lines were scanned in η direction. With a projection the refractive index profile as a function of the depth z can be obtained.

coefficient $R = I_R/I_0$ by the Fresnel formula, where I_0 is the incident light intensity and I_R the reflected one. For normal incidence n is given by

$$n = \frac{1 + \sqrt{R}}{1 - \sqrt{R}}. \quad (6.2)$$

The laser light of a HeNe laser was focused on the sample surface to a beam diameter of less than $5 \mu\text{m}$. It was linearly polarized along the dielectric x_1 axis, since the alteration of n_1 is of main interest in order to use the largest electro-optic coefficient r_{111} of DAST. The lines were then scanned in η direction with a step size of $8 \mu\text{m}$. Since the η and the z axis are related to each other by a simple projection, this measurement yields a depth resolution in z direction of less than $0.2 \mu\text{m}$. The back reflected light from the sample surface was deflected by a beam splitter and detected with a photodiode.

6.3.3 Results: Refractive index profile

The measured refractive index profiles indicated by dots for five different fluences are shown in Fig. 6.4. The refractive index is decreased by electron beam exposure. For a fluence of $\phi = 2.6 \text{ mC/cm}^2$, a maximal refractive index reduction of $\Delta n = -0.3$ is achieved. The shape of the refractive index profile is similar to the one of the deposited energy, compare Fig. 6.2. The full curves correspond best to the theoretical model described in Section 6.3.1 and were obtained by least-squares theoretical analysis with the following remarks. The analysis showed

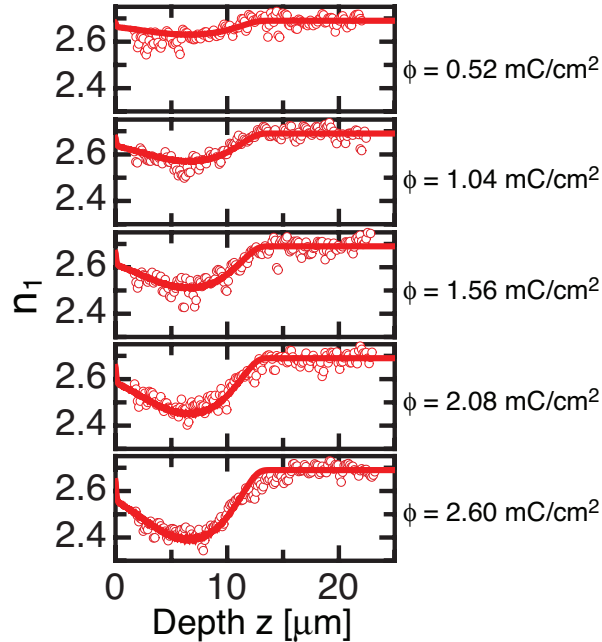


Figure 6.4: Refractive index profiles. Measured refractive index n_1 (dots) as a function of the depth z shown for five different fluences. The solid curves correspond best to the theoretical model of Eq. (6.1) or (6.3).

that the factor γ is equal to 1 and that we are in a low fluence regime for the used fluences of up to 2.6 mC/cm^2 , which means that the argument of the exponential term is $\phi G(z)/G_0 \ll 1$ and can be consequently linearised, which yields

$$\Delta n(z) = \frac{\Delta n_{\max}}{G_0} \phi G(z) = c \phi G(z) \quad (6.3)$$

with $c = -0.036 \pm 0.001 \text{ cm}^2 \mu\text{m}/(\text{CeV})$ at a wavelength of $\lambda = 633 \text{ nm}$. The refractive index change at a certain position is therefore simply proportional to the deposited energy $\phi G(z)$, and can be calculated for any exposure parameters in the low fluence regime by considering only one experimental constant c .

6.4 Dispersion of the refractive index change

Since we are mainly interested in waveguiding at telecommunication wavelengths, the dispersion of the proportionality constant $c(\lambda)$ is also important. A relation between the microscopic material modification and the resulting refractive index reduction will be derived with help of the Lorentz-Lorenz relation in order to finally calculate c at a wavelength of $\lambda = 1.55 \mu\text{m}$.

Micro Raman scattering experiments at a fundamental wavelength of 785 nm were performed to study the changes in the molecular structure appearing upon electron beam exposure. For the measurements with polarizer and analyzer oriented along the dielectric x_1 axis at the position of the highest electron fluence of $\phi = 2.6 \text{ mC/cm}^2$, a reduction of about 10-15% of the Raman line at 1577 cm^{-1} was detectable, which corresponds to the C-C=C-C in plane stretching frequency of the carbon backbone between the aromatic rings of the stilbazolium chromophore shown in Fig. 6.1 [19]. As a consequence, this leads to a reduction of the molecular polarizability α_1 and therefore to a change in the refractive index n_1 .

The refractive index n_ω at a frequency ω is related to the molecular polarizability $\alpha(\omega)$ by

$$n_\omega^2 - 1 = N f_\omega \alpha(\omega), \quad (6.4)$$

where N denotes the number of molecules per volume and $f_\omega = (n_\omega^2 + 2)/3$ is the Lorentz local field factor. After exposure, the refractive index $\tilde{n}_\omega(z)$ at depth z is altered due to the fact that some chromophores are modified. Therefore, the refractive index \tilde{n}_ω is given by

$$\tilde{n}_\omega^2 - 1 = p N \tilde{f}_\omega \alpha(\omega) + (1 - p) N \tilde{f}_\omega \tilde{\alpha}(\omega), \quad (6.5)$$

where p is the percentage of unmodified molecules after electron beam exposure and $\tilde{\alpha}$ represents the polarizability of the modified molecules. $\tilde{\alpha}$ can be expressed by

$$\tilde{\alpha}(\omega) = k_\omega \alpha(\omega), \quad (6.6)$$

where k_ω denotes the percentage of remaining polarizability of the modified molecule. Combining Eqs. (6.4-6.6), the percentage of unmodified molecules $p(z)$ at the depth z is given by

$$p(z) = \frac{\frac{\tilde{n}_\omega^2(z) - 1}{\tilde{n}_\omega^2(z) + 2} \frac{n_\omega^2 + 2}{n_\omega^2 - 1} - k_\omega}{1 - k_\omega}. \quad (6.7)$$

Since the percentage of unmodified molecules $p(z)$ is independent of the wavelength, the refractive index profile $\tilde{n}_{\omega'}(z)$ at the frequency ω' can be calculated with help of the following equation

$$\frac{\frac{\tilde{n}_{\omega}^2(z)-1}{\tilde{n}_{\omega}^2(z)+2} \frac{n_{\omega}^2+2}{n_{\omega}^2-1} - k_{\omega}}{1 - k_{\omega}} = \frac{\frac{\tilde{n}_{\omega'}^2(z)-1}{\tilde{n}_{\omega'}^2(z)+2} \frac{n_{\omega'}^2+2}{n_{\omega'}^2-1} - k_{\omega'}}{1 - k_{\omega'}}. \quad (6.8)$$

Taking the reasonable assumption that k_{ω} is constant with wavelength, i.e. $k_{\omega} = k_{\omega'}$, the refractive index profiles at $1.55 \mu\text{m}$ can be calculated using Eq. (6.8) with the data at 633 nm , which leads to $c(\lambda = 1.55 \mu\text{m}) = -0.019 \pm 0.001 \text{ cm}^2 \mu\text{m}/(\text{CeV})$. In order to estimate the accuracy of this assumption, we calculated the lower limit for c at $1.55 \mu\text{m}$ by taking the strict condition that the polarizability of the modified molecule is dispersion free. Lowering the polarizability of the modified molecules from 50% to 10% of their initial value at the zero frequency limit i.e. $\tilde{\alpha}(\lambda = 633 \text{ nm}) = \tilde{\alpha}(\lambda = 1.55 \mu\text{m}) = \tilde{\alpha}(\lambda = \infty)$, the values of the corresponding c parameters were agreeing within 15% to the value obtained by considering $k_{\omega} = k_{\omega'}$.

For a peak refractive index reduction of $\Delta n_1 = -0.3$ as obtained by using an electron fluence of $2.6 \text{ mC}/\text{cm}^2$, the percentage of unmodified molecules is $p_{\text{peak}} = 0.90$ considering $k_{\omega} = 0$, and $p_{\text{peak}} = 0.86$ considering a reduction of the polarizability to 30% i.e. $k_{\omega} = 0.3$, which is in reasonable agreement with the results of the Raman measurement.

6.5 Realization of channel waveguides

6.5.1 Concept of channel waveguide patterning

The electrons of the writing beam are scattered in the material and therefore the beam is broadened. This circumstance can be exploited to directly write channel waveguides in a bulk crystal by exposing two lines separated by the waveguide width as depicted in Fig. 6.5. Between the two lines an unexposed region surrounded by an e-beam modified area with lowered refractive index remains and thus a channel waveguide is formed. The advantage of this configuration is that the waveguide core is mostly in the virgin material, in which the nonlinear and electro-optic properties are the same as in the bulk material.

With the CASINO simulation software the 2 dimensional energy distribution in the target material for an electron beam at a fixed position can be calculated. Subsequently the energy distribution for the configuration shown in Fig. 6.5 was calculated by overlapping the single beam distributions over the exposed area. Using the relation between the refractive index reduction and the electron fluence obtained in Sections 6.3 and 6.4, the two dimensional refractive index cross section was calculated. In Fig. 6.6 the calculated refractive index profile of n_1 at the telecommunication wavelength of $1.55 \mu\text{m}$ for an electron fluence of $\phi = 2.6 \text{ mC}/\text{cm}^2$, a line width $L = 4 \mu\text{m}$ and a waveguide core width of $W = 6 \mu\text{m}$ is shown. The refractive index profile is supporting several guided modes, which were evaluated with the commercially available integrated optics software OlympIOs with the full vectorial complex bend 2D mode solver. The

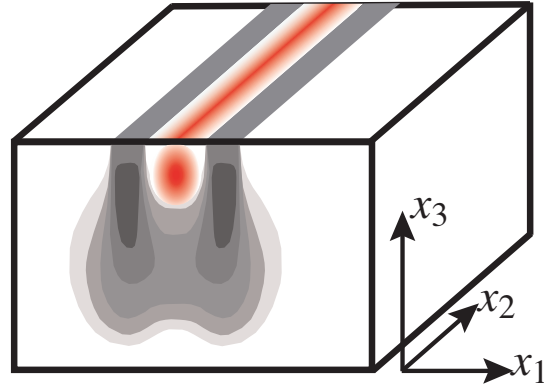


Figure 6.5: Concept of channel waveguide patterning in DAST. Two lines spaced by the waveguide core width are exposed by e-beam (gray). Since the electron beam is widened up in the target material, an unexposed region surrounded by an exposed area with lowered refractive index is created and thus a waveguide formed (red).

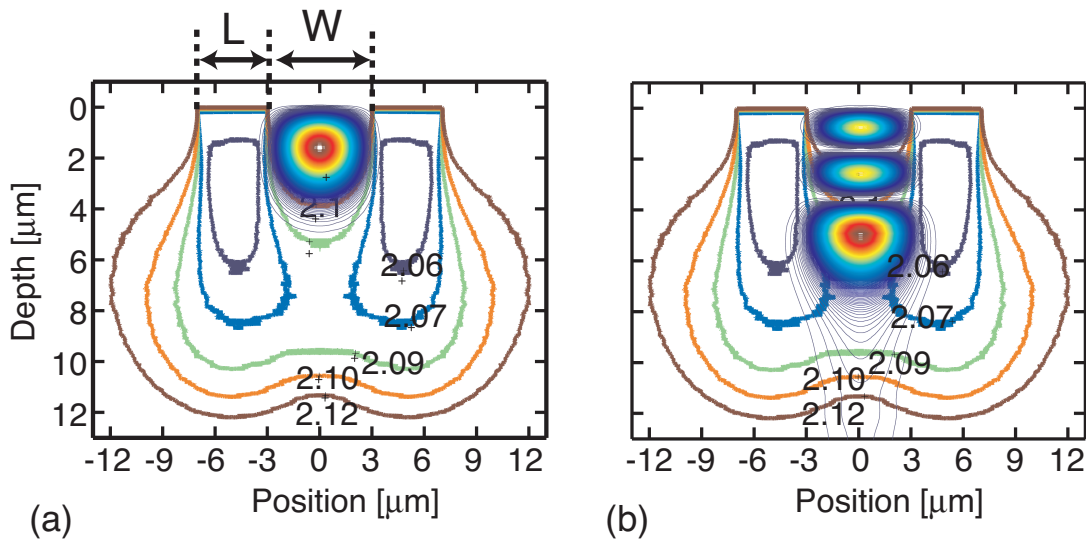


Figure 6.6: Refractive index profile and corresponding modes. Calculated 2D profile of the refractive index n_1 at a wavelength of $\lambda = 1.55 \mu\text{m}$ for an electron fluence of $\phi = 2.6 \text{ mC/cm}^2$, a line width $L = 4 \mu\text{m}$ and a waveguide core width of $W = 6 \mu\text{m}$. The corresponding first and third order modes are depicted in Figure (a) and (b), respectively.

resulting intensity profiles of the first order and the third order mode are depicted in Fig. 6.6(a) and (b), respectively. Whereas the first mode is well confined and has simulated losses below 0.1 dB/cm, the third order mode is leaky with tunneling losses of over 20 dB/cm.

6.5.2 Waveguiding observation

We have produced several channel waveguide structures using electron fluences of 0.65, 1.3, and 2.6 mC/cm² with a line width of $L = 4 \mu\text{m}$ and varying the waveguide core width $W = 3, 6, 9,$ and $12 \mu\text{m}$. The x_1x_3 end-faces were subsequently polished and waveguiding experiments performed by standard end-fire coupling with the setup depicted in Fig. 6.7(a). The laser light with a wavelength of $\lambda = 1.55 \mu\text{m}$ was propagating along the x_2 direction and was polarized parallel to x_1 as shown in Fig. 6.7(b).

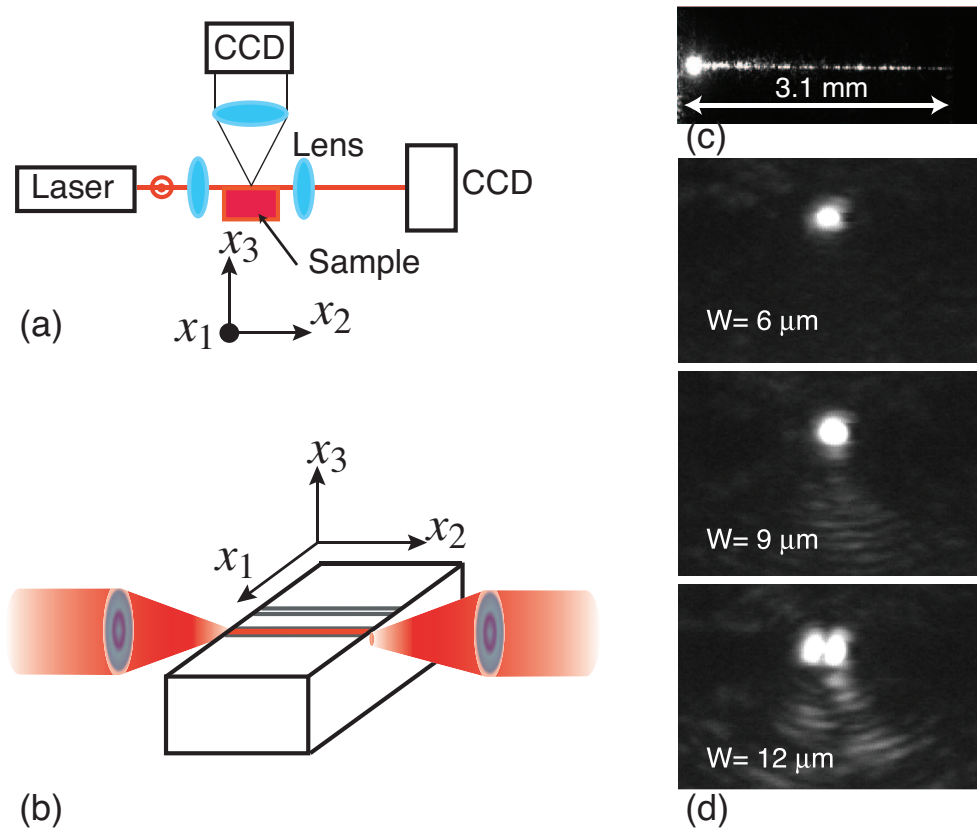


Figure 6.7: Waveguiding observation. (a) Experimental setup for the determination of the waveguiding characteristics and propagation losses: CCD: infrared camera. (b) Waveguiding configuration: the light at a wavelength of $\lambda = 1.55 \mu\text{m}$ polarized parallel to x_1 was propagating along the x_2 direction. (c) Photograph of the sample surface taken from top with the CCD camera and (d) from the end face for different waveguide widths W . The line width was $L = 4 \mu\text{m}$ and the structures were exposed with an electron fluence of $\phi = 2.6 \text{ mC/cm}^2$.

Waveguiding was clearly observed for the fluences of 1.3 and 2.6 mC/cm², whereas the structures exposed with the lowest fluence of 0.65 mC/cm² had too large tunneling losses, as confirmed by simulations. In Fig. 6.7(c) a photograph taken from top is shown and in (d) photographs of the mode profiles taken at the output face of waveguides with core widths of 6, 9, and 12 μm, and a fluence of 2.6 mC/cm² are depicted. We were not able to efficiently couple light into the waveguides with a core width of $W = 3 \mu\text{m}$ because of the not perfect edge quality.

The waveguide losses were measured by detecting the scattered light from top with a CCD camera and are about 20 dB/cm, which is in contrast to the simulated losses of less than 0.1 dB/cm for the first order modes. We attribute this partly to the edge quality and therefore to a weak coupling efficiency to the first order mode. This is confined close to the surface, whereas higher order modes are easier to excite, since they are less confined at the sample surface, but they have high tunneling losses (see also Fig. 6.6). We therefore believe that a measurement of the propagation losses from a top view is being influenced by the decay of the higher order modes, since most of the energy is coupled into them.

6.6 Electro-optic modulation

Mach-Zehnder structures were successfully realized with similar parameters as the channel waveguides. The electron fluence was varied from 1.3 to 2.6 mC/cm² at core widths of $W = 4, 6$ and $8 \mu\text{m}$. The line width L was chosen to be $5 \mu\text{m}$ in order to reduce the tunneling losses into the substrate at the Y-junctions of the structures. A schematic illustration of the Mach-Zehnder geometry is shown in Fig. 6.8.

Electrodes were patterned subsequent to the electron beam exposure by the following procedure. First, the sample was covered with a SU-8 layer with a thickness of about $2 \mu\text{m}$, which was acting as an optical buffer and at the same time as a protecting layer against different solvents used during the electrode structuring process. The electrodes were then patterned in an AZ-5214 photoresist by standard photolithography. After depositing 5 nm Cr and 100 nm Au, the AZ-resist was washed away with acetone. A schematic illustration of the structuring procedure is shown in Appendix C.

The electro-optic modulation measurements were performed in the experimental configuration shown in Fig. 6.9(a). The light was propagating in x_2 direction and was polarized parallel to the dielectric x_1 axis in order to use the largest electro-optic coefficient of DAST i.e. $r_{111} = 47 \text{ pm/V}$ at $1.55 \mu\text{m}$. The phase shift between the two arms is given by [6]

$$|\phi| = 2k|\Delta n_1|L_o = 2\frac{\pi}{\lambda}n_1^3r_{111}E_1L_o, \quad (6.9)$$

where L_o is the arm length (overlap length between the modulation field the guided optical wave) and E_1 represents the magnitude of the modulation field along x_1 inside the DAST waveguides, which was calculated with Femlab (www.femlab.com). The modulation amplitude

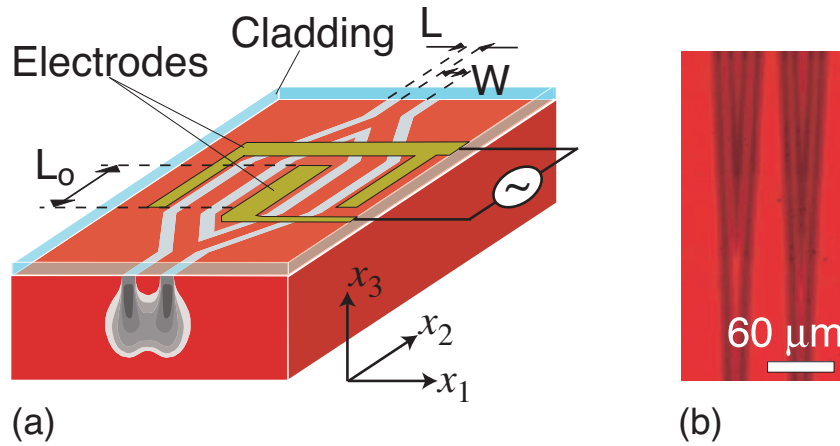


Figure 6.8: Mach-Zehnder modulator. (a) Mach-Zehnder modulator geometry in DAST with in plane electrodes in order to use the largest electro-optic coefficient r_{111} of DAST; L_o : electrical and optical field overlap length, L : line width, and W : waveguide core width. (b) Photography of a Y-junction with light illumination in transmission. The modified regions appear darker due to a red shift of the absorption edge upon e-beam irradiation. The bend radii of the circle segments used to pattern the Y-junctions were 5 mm long.

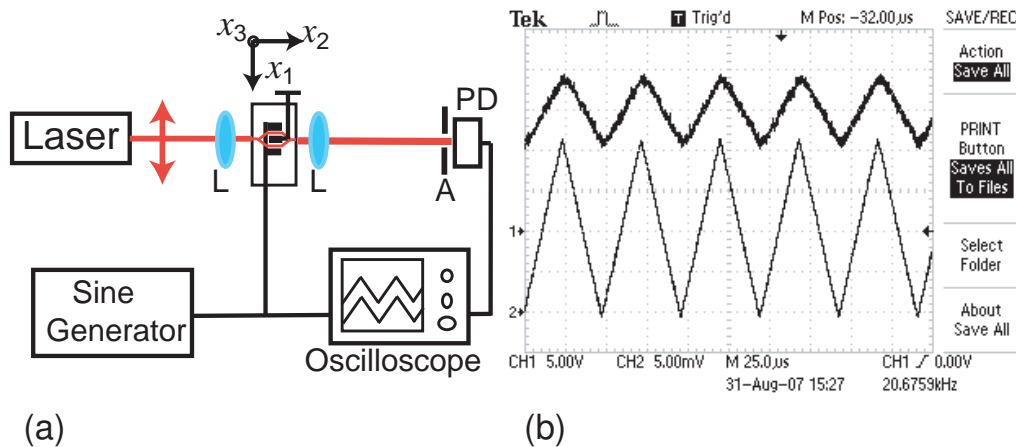


Figure 6.9: Electro-optic modulation in DAST. (a) Measurement setup for the electro-optic modulation experiment. The light at a wavelength of $1.55 \mu\text{m}$ is propagating along the x_2 direction and is polarized parallel to the x_1 axis. The modulated light intensity was detected with a photodiode. PD: photodiode, A: aperture and L: lens. (b) The applied modulation voltage at a frequency of 20 kHz (lower curve) and the detected signal with the photodiode (upper curve) are depicted.

at the output of the Mach-Zehnder structure is proportional to $\cos^2(\phi/2)$. In Fig. 6.9(b) the applied modulation voltage (amplitude of 10 V, lower curve) and the measured modulated signal (upper curve) at the output of the Mach-Zehnder device are shown for a waveguide width of $W = 4 \mu\text{m}$, for which the best performance was obtained. The amplitude of the modulation was about 20% of the output signal. At present, the half wave voltage is still higher than 10V, since the modulator dimensions and the electrode arrangement have not been optimized yet. The electrode spacing was with $20 \mu\text{m}$ relatively wide, and the effective interaction arm length, where the optical and electric fields were overlapping, was only $L_o = 0.85 \text{ mm}$ long.

6.7 Towards single mode waveguides

Single mode characteristics is of importance for electro-optic applications. Some electron beam systems offer now the possibility to irradiate the sample under an angle. This possibility can be used to produce single mode waveguides in DAST. In Fig. 6.10 one possible configuration with single mode behavior is given with a waveguide core width of $W = 4 \mu\text{m}$ and a side wall width of $3 \mu\text{m}$. The refractive index profile depicted corresponds to an applied electron fluence of 2.6 mC/cm^2 . The electron beam was tilted by 30° in this simulation. The simulated losses for this single mode configuration are lower than 1 dB/cm .

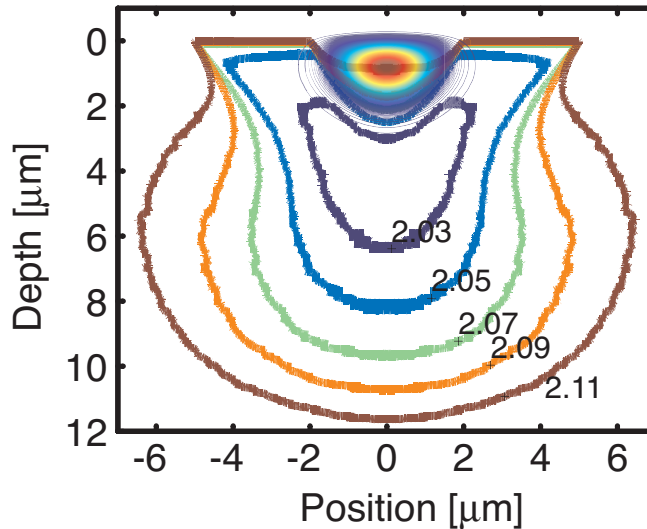


Figure 6.10: Single mode waveguide. A possible configuration for the production of a single mode waveguide obtained by tow irradiations and tilting the electron beam by 30° . The depicted refractive index profile at $1.55 \mu\text{m}$ corresponds to an electron fluence of 2.6 mC/cm^2 and an energy of 30 keV .

6.8 Conclusion

In conclusion, we have successfully applied direct electron beam patterning to organic crystalline materials. For the first time, optical channel waveguides and Mach-Zehnder structures in a bulk organic crystal have been produced in a single exposure step by applying a new concept, which is also offering the advantage that the waveguide core is not affected by the electron beam and thus the electro-optic and nonlinear optic properties are therein the same as in the bulk material. Waveguiding has been demonstrated in DAST channel waveguides and Mach-Zehnder modulators structured by using 30 keV e-beam irradiation. In addition, a first electro-optic modulation has been demonstrated in the produced Mach-Zehnder modulators. Therefore, this work gives a new perspective for the use of nonlinear optical organic materials for integrated optics.

The refractive index profile in DAST has been measured as a function of the electron range and the electron fluence in DAST. A reduction of the refractive index n_1 of $\Delta n_1 = -0.3$ at a wavelength of 633 nm has been obtained using an electron fluence of 2.6 mC/cm². Using this data and the 2 dimensional refractive index profile of the channel waveguide, the corresponding mode profiles and losses were determined. Furthermore, a configuration for single mode waveguides in DAST has been proposed which is of importance for future applications.

Chapter 7

New materials for nonlinear optical applications

In this chapter we give a very brief overview of new ionic-type crystals, which have been developed and investigated in our laboratory during the last years.

New material synthesis and the investigation of their fundamental chemical and physical properties are important issues concerning the wide use of organics in photonic applications. Organic materials offer several advantages over inorganic-type and standard semiconductor materials. They generally exhibit higher and faster nonlinearities and in addition offer numerous design possibilities [83,84]. Among organic materials, crystals based on strong Coulomb interactions are very attractive because of the following reasons. They show large nonlinearities, are very stable and relatively often crystallize in a noncentrosymmetric structure. The noncentrosymmetric crystal packing is achieved by strong Coulomb interactions between the anionic and cationic molecules in the crystal, thus the preferred antiparallel arrangement of the dipolar chromophores is circumvented [41,85].

The widely used and studied organic material DAST is such an ionic-type crystal whose crystallographic and optical properties have been presented in Chapter 2 already. Its high nonlinear optical coefficients are making DAST highly attractive for applications such as frequency conversion, electro-optic applications, optical parametric oscillation and THz generation. Despite various investigations and studies, the growth of large size high optical quality DAST crystals is still cumbersome and time consuming, with 4-6 week needed to attain a crystal with a surface area of about 1 cm^2 [46].

New materials which are easier and faster to grow are therefore desired. Furthermore, the theoretical limits of the second-order nonlinear optical activity of crystalline materials are still far from being reached [7]. It has already been shown that the crystal packing is very sensitive to minor changes of the molecular constituents [86]. Following the approach of changing the counter ion [87,88], several new DAST derivatives were synthesized and characterized. In Table 7.1 the chemical structures, the chemical formulas, the abbreviated names, the crystal-

Structure	Name Formula	Crystal system	Space group	Powder test ¹	Growth mm ³	Ref.
 	DAST $C_{23}H_{26}N_2O_3S$	monoclinic	Cc	1	$25 \times 25 \times 3$ (methanol)	[44]
 	DSHS $C_{22}H_{24}N_2O_4S$			0	(methanol)	[89]
 	DSMOS $C_{23}H_{26}N_2O_4S$	triclinic	P1	0.9pns	$3 \times 5 \times 0.3$ (methanol)	[89]
 	DSAS $C_{22}H_{25}N_3O_3S$			1pns	(methanol)	[89]
 	DSMAS $C_{24}H_{29}N_3O_3S$			0.7pns	(methanol)	[89]
 	DSTMS $C_{25}H_{32}N_2O_3S$	monoclinic	Cc	1	$30 \times 30 \times 2$ (methanol)	[90]
 	DSNS $C_{26}H_{26}N_2O_3S$	triclinic	P1	1.5	$2 \times 0.1 \times 0.1$ (DMSO)	[91]
 	DSMFS $C_{23}H_{23}F_3N_2O_3S$	triclinic	$\bar{P}1$	0	$3 \times 3 \times 0.2$ (methanol)	[92]
 	DSPFS $C_{23}H_{23}F_3N_2O_3S$	monoclinic	Cc	0.9	$5 \times 5 \times 1$ (ethanol)	[92]

Table 7.1: Summary of the investigated compounds. Given are the crystal system and the space-group symmetry. The data obtained by Kurtz powder test are referenced to DAST. The abbreviation *pns* after the number stands for that the ground powder was not sieved. The typical sample size of the crystals grown by slow cooling or solvent evaporation are given in the column "Growth" together with the used solvents.

lographic data, second-harmonic efficiency compared to DAST and their growth capability are summarized [89, 91, 92]. The second-harmonic efficiency was measured by Kurtz powder test technique in back reflection configuration at a fundamental wavelength of $1.9\ \mu\text{m}$ [93]. The second-harmonic signal at $950\ \text{nm}$ was then detected with a Si photodiode. Special care was taken to remove contributions from third-harmonic generation by putting appropriate filters. The ground powder was normally sieved to obtain particles with similar size ($60 - 90\ \mu\text{m}$). The abbreviation *pns* in Table 7.2 stands for powder not sieved, resulting in an uncertainty of about 10%-40% of the measured power. Crystal growth experiments were performed by slowly cooling the supersaturated solvent or by solvent evaporation.

The two crystallized compounds DSHS and DSMFS were centrosymmetric and therefore showed no second-harmonic generation. Crystal growth of the three materials DSHS, DSAS and DSMAS resulted in very small crystals, hence no further investigations could be made. DSMOS and DSNS showed a similar or superior second-order activity compared to DAST with 0.9 and 1.5 second-harmonic powder efficiency, respectively, but neither of these materials showed better crystal growth capability. The most promising material of the investigated organic salts is DSTMS, which has a similar second-harmonic efficiency and exhibits easier thin film processing and bulk crystal growth compared to DAST. Very large bulk crystal of more than $3 \times 3 \times 0.2\ \text{cm}^2$ with high optical quality were grown as well as thin DSTMS films of $5 \times 6\ \text{mm}^2$ area and a thickness of $5 - 30\ \mu\text{m}$ [90]. DSTMS also offers the advantage that the growth rate is by a factor 2-3 higher compared to DAST. The reasons are that the solubility of DSTMS in methanol is more than two times higher and that DSTMS nucleates fast and grows along all edges, whereas DAST prefers to only grow along the polar axis. A detailed study of the linear optical and nonlinear optical properties of this new promising organic crystal is given in Chapter 8.

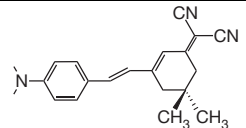
Structure	Name Formula	Crystal system	Space group	Powder test	Growth mm^3	Ref.
	DAT2 $\text{C}_{21}\text{H}_{23}\text{N}_3$	monoclinic	$P2_1$	$0.35@1.3\ \mu\text{m}$	$1 \times 1 \times 0.05$ (melt)	[94]

Table 7.2: Summary of properties of DAT2: Given are the crystal system, the space-group symmetry and the typical sample size of the crystals grown by Bridgman type melt growth technique. The data obtained by Kurtz powder test are referenced to DAST.

The organic salt nonlinear optical crystals shown in Table 7.1 have to be grown from solution. Melt growth, which is advantageous because of much faster growth rates, cannot be applied since the decomposition temperature of the optical chromophores is near their melting temperature. Therefore, new polyene chromophores, which were configurationally locked to increase their thermal stability, were investigated in our laboratory. The chromophores consist

of a π -conjugated hexatriene bridge between the dialkylamino or methoxy electron donors and the dicyanomethylidene electron acceptor [94]. Among the investigated molecules, 2-{3-[2-(4-dimethylaminophenyl)-vinyl]-5,5-dimethylcyclohex-2-enylidene} malononitrile (DAT2) exhibits a strong second-harmonic activity with 35% of the value of DAST at a wavelength of 1300 nm. The melting temperature and recrystallization temperature of DAT2 appear at about 235°C and 155°C, respectively. Since the decomposition temperature is above 300°C, DAT2 crystals were successfully grown by a Bridgman type melt growth technique. The typical samples obtained had a side length of about 0.5-2 mm and a thickness of less than 50 μm . A summary of the most important properties of DAT2 is given in Table 7.2. Configurationally locked polyene organic crystals are due to the much faster growth rate as well as the easier thin film processing very promising and attractive for applications in integrated electro-optics. Nevertheless, the nonlinearity achieved is not yet so high as for stilbazolium salts.

Chapter 8

Linear and nonlinear optical properties of the organic crystal DSTMS §

We report on the linear and nonlinear optical properties of the novel organic crystal 4-N, N-dimethylamino-4'-N'-methyl-stilbazolium 2,4,6-trimethylbenzenesulfonate (DSTMS). The principal refractive indices n_1 , n_2 , and n_3 have been determined by a direct measurement of the group index dispersion over a broad wavelength range from 0.6 to 1.6 μm . The linear absorption coefficients for light polarized along the dielectric axes have been measured in the transparency range from 600 to 2000 nm. DSTMS crystals show a large birefringence of $\Delta n = 0.5$ and low absorption $\alpha < 0.7\text{cm}^{-1}$ in the telecommunication wavelength range at 1.55 μm . Furthermore, the nonlinear optical tensor elements d_{111} , d_{122} , and d_{212} have been determined by the Maker-fringe technique at the fundamental wavelength of 1.9 μm . DSTMS crystals exhibit a very large nonlinear activity with a nonlinear optical coefficient $d_{111} = 214 \pm 20$ pm/V. Phase-matching curves determined from our optical data showed that parametric oscillation can be achieved in the wavelength range from 1 to 2.2 μm with effective nonlinear optical coefficients larger than 25 pm/V.

8.1 Introduction

Organic noncentrosymmetric materials are of great interest for applications in nonlinear optics, such as parametric light generation, frequency conversion, terahertz (THz) wave generation, and electro-optic light modulation [6]. These materials offer vast design possibilities to tailor the linear and nonlinear properties, and very high optical nonlinearities can be achieved. Owing to

[§]This chapter has been published in Journal of the Optical Society of America B, **24** (9), p. 2556-2561 (2007) [95]

the almost completely electronic origin of the nonlinearity, they are well suited for future high-speed devices. Compared with more widely studied poled electro-optic polymers [26], organic nonlinear optical crystals exhibit superior orientational (thermal) stability and photostability, which are the most critical parameters for implementing organic materials into real devices. Waveguide structuring for integrated optics with organic crystals by photobleaching [60, 63], femtosecond ablation [61], and ion implantation [69], as well as electro-optic modulation in thin organic single crystalline films [47] and channel waveguides produced by a graphoepitaxial melt growth [62] have been demonstrated. Besides these applications, organic crystals have recently attracted much attention as very efficient THz emitters by exploiting the process of optical rectification. The requirements for efficient THz generation are a high second-order nonlinear optical susceptibility and the possibility for velocity matching that is achievable in organic materials owing to relatively low dielectric constants [58]. The organic crystal 4-N, N-dimethylamino-4'-N'-methyl-stilbazolium tosylate (DAST) is at present the only commercial available material showing very high second-order nonlinear activity with $d_{111} = 210$ pm/V at $1.9 \mu\text{m}$ [42] combined with a low dielectric constant $\epsilon_{11} = 5.2$, and is therefore a very efficient source of THz radiation [58]. The growth of high optical quality DAST single crystals is still a challenge, and therefore optimization of the growth techniques [46, 96, 97] and the development of new molecules for crystal growth [85, 89, 94, 98] are subjects of present research.

We have recently developed a new promising stilbazolium salt 4-N, N-dimethylamino-4'-N'-methyl-stilbazolium 2,4,6-trimethylbenzenesulfonate (DSTMS) with very favourable crystal growth characteristics [90]. Owing to the high solubility in methanol - more than two times the one of DAST at room temperature - we were able to obtain very-large-area bulk single crystals of more than $3 \times 3 \times 0.2 \text{ cm}^3$ with high optical quality. In our work we report on the linear and nonlinear optical properties of DSTMS and present the phase-matching conditions for generation of light by optical parametric processes. We prove that DSTMS has superior properties as compared with DAST, since DSTMS shows excellent optical quality and the growth of large and high optical quality crystals is faster and more reproducible.

8.2 Crystal properties

DSTMS consists of a positively charged nonlinear optical chromophore stilbazolium and a negatively charged 2,4,6-trimethylbenzenesulfonate anion as shown in Fig. 8.1(a). The counter ion is used to override the preferred antiparallel crystallization of the chromophores. The single crystals used in our experiments were all grown in our laboratory from supersaturated methanol solution by the temperature-lowering method [90]. The samples used for our optical measurements were as grown c plates of about 1 mm thickness with the ab plane parallel to the largest surface (typically $5 \times 5 \text{ mm}^2$), or a plates with a thickness of about 2 mm and an area of $5 \times 5 \text{ mm}^2$ cut from a larger single crystal. The ab and the bc surfaces were polished to $\lambda/4$ surface quality.

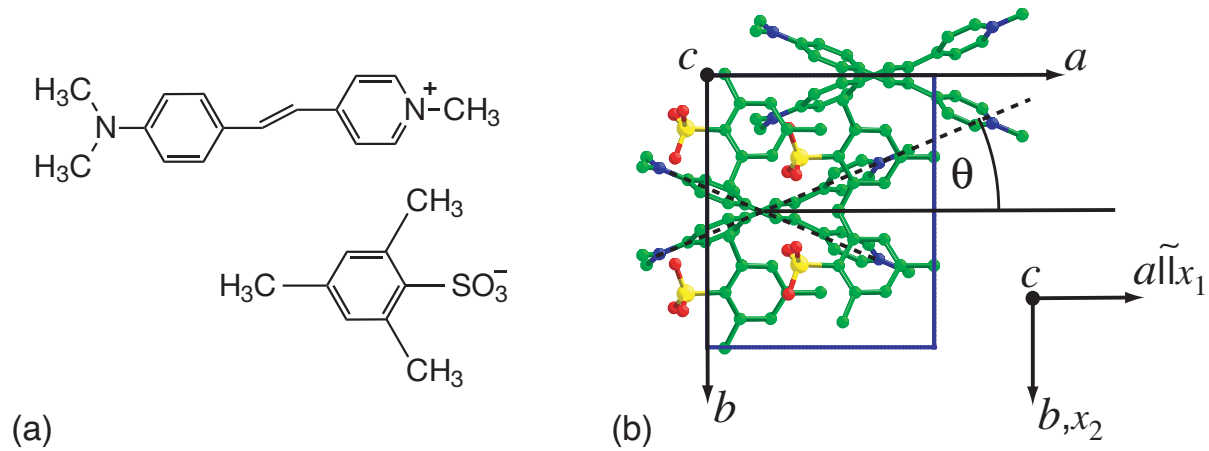


Figure 8.1: Molecular units of DSTMS. (a) Positively charged non-linear optical active chromophore stilbazolium and negatively charged 2,4,6-trimethylbenzenesulfonate anion. (b) Arrangement of the molecules in the unit cell as viewed along the c axis.

DSTMS belongs to the monoclinic space group Cc (point group m) with four cations and anions per unit cell, as depicted in Fig. 8.1(b). The lattice parameters are $a = 10.266 \text{ \AA}$, $b = 12.279 \text{ \AA}$, and $c = 10.266 \text{ \AA}$, with $\alpha = \beta = 90^\circ$ and $\gamma = 93.04^\circ$ [90].

The linear and the nonlinear optical properties are predominately ruled by the nonlinear optical chromophores, whose charge-transfer axes make an angle of $\theta = \pm 23^\circ$ with the crystallographic a axis [Fig. 8.1(b)]. The dielectric x_2 axis lies parallel to the crystallographic b axis, whereas the dielectric x_1 axis is almost parallel to the crystallographic a axis with an inclination angle of $3.6 \pm 0.3^\circ$, which we have determined in our samples by conoscopy [99].

8.3 Refractive indices of DSTMS

The refractive indices of DSTMS were determined with the previously reported group-index dispersion method [100] that can be summarized as follows. In a first step the group index n_g is obtained by measuring the time retardation ΔT of a femtosecond pulse within a sample relative to air. By acquiring group-index data over a broad wavelength range and analyzing the data set with the Sellmeier equation, the refractive index dispersion $n(\lambda)$ can be calculated. We applied this simple method because it is well suited for measuring the refractive indices of coplanar crystal plates.

The time retardation ΔT of the pulse within the sample relative to air is determined at each wavelength by two correlation measurements with the experimental setup shown in Fig. 8.2. In a first measurement the correlation between a probe pulse traveling in a delay line and the pulse propagating through the sample is measured. For the second measurement the sample is removed. In our experimental configuration the correlation was determined by noncollinear

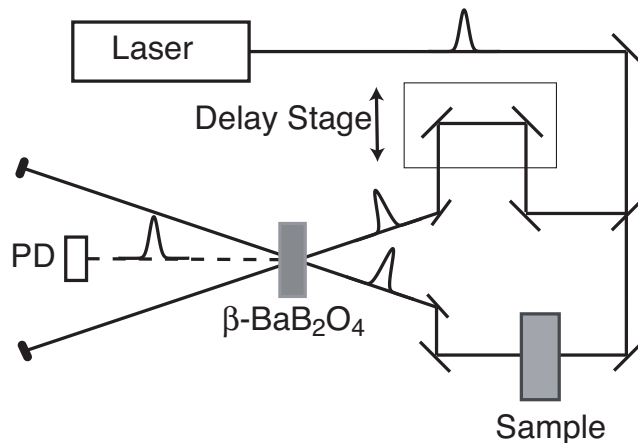


Figure 8.2: Refractive index setup. Experimental setup for determining the transit time of a femtosecond pulse traveling through a sample. Correlation measurements between a probe pulse in a delay line and a second pulse, which passes through the sample, are performed by noncollinear phase-matched second-harmonic generation in a β -BaB₂O₄ (BBO) crystal. A signal is detected with the photodiode (PD) only when the two pulses are spatially and temporally overlapping. A second correlation measurement without the sample is done to determine the time retardation ΔT relative to air.

phase-matched second-harmonic generation in a nonlinear optical β -BaB₂O₄ crystal. Thus, a signal is detected with the photodiode only when a spatial and temporal overlap between the probe pulse and the second pulse, which propagates through the sample or air in the reference measurement, is achieved. The time retardation ΔT is given by

$$\Delta T(d, \lambda) = \frac{d}{c} [n_g(\lambda) - n_{g,\text{air}}(\lambda)], \quad (8.1)$$

where d is the thickness of the sample and c the speed of light in vacuum. For the group index in air we used $n_{g,\text{air}} = 1$. The group index n_g is defined as

$$n_g(\lambda) = n(\lambda) - \lambda \frac{\partial n(\lambda)}{\partial \lambda}. \quad (8.2)$$

For our measurements we used an optical parametric generator/amplifier (OPG/OPA) (Quantronix, TOPAS) pumped with a Ti:sapphire laser providing 160 fs pulses at a center wavelength of 776 nm with a repetition rate of 1 kHz. Thus we were able to measure the group refractive index in a broad wavelength range from 570 to 1600 nm for light polarized along the principle dielectric axes. Figure 8.3 shows the measured group indices $n_{g,1}$ (circles), $n_{g,2}$ (diamonds), and $n_{g,3}$ (triangles) for light polarized along the dielectric x_1 , x_2 , and x_3 axes, respectively. To analyze the measured group-index dispersion we used a theoretical Sellmeier formula for $n(\lambda)$ considering one main oscillator given by

$$n^2(\lambda) = n_0^2 + \frac{q\lambda_0^2}{\lambda^2 - \lambda_0^2}, \quad (8.3)$$

where $\nu_0 = c/\lambda_0$ is the resonance frequency of the main oscillator and q is the oscillator strength. n_0 summarizes contributions from all other oscillators. The dashed curve in Fig. 8.3 corresponds best to the experimental data obtained by a least-square theoretical analysis. The resulting parameters are listed in Table 8.1.

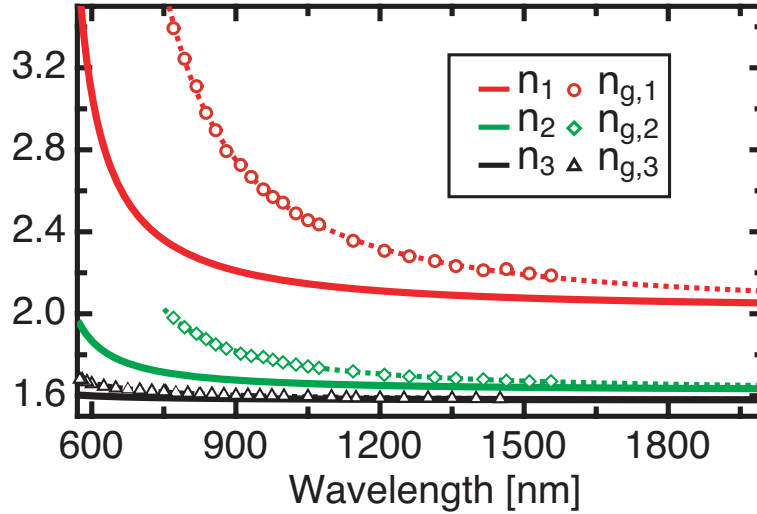


Figure 8.3: Group and refractive indices of DSTMS. Group indices $n_{g,1}$ (circles), $n_{g,2}$ (diamonds), and $n_{g,3}$ (triangles) of DSTMS as a function of the wavelength λ . The dashed curves are according to Eqs. (8.2) and (8.3) and correspond best to the experimental data, obtained by least-squares theoretical analysis. The solid curves are the corresponding dispersion relations of the refractive indices n_1 , n_2 , and n_3 , respectively.

	n_1	n_2	n_3
q	1.45 ± 0.05	0.36 ± 0.04	0.11 ± 0.07
n_0	2.026 ± 0.006	1.627 ± 0.004	1.579 ± 0.005
λ_0 [nm]	532 ± 5	502 ± 11	360 ± 100

Table 8.1: Sellmeier parameters for the refractive index dispersion of Eq. (8.3) that correspond best to the experimental data shown in Fig. 8.3 obtained by least square theoretical analysis.

The solid lines in Fig. 8.3 are the calculated refractive-index dispersion curves for n_1 , n_2 , and n_3 obtained with the parameters of Table 8.1. Because of the weak dispersion of the refractive index n_3 , the resonance wavelength λ_0 and the oscillator strength q along this axis could be determined with limited precision only.

DSTMS is highly anisotropic exhibiting a refractive index difference $\Delta n = 0.5$ between the refractive indices n_1 and n_2 at $1.5 \mu\text{m}$, which can be explained by the preferential alignment of the nonlinear optical chromophores along the x_1 axis, as depicted in Fig. 8.1.

8.4 Absorption coefficients of DSTMS

The transmission was measured for light polarized along the dielectric axes in the wavelength range from 400 to 2000 nm. The absorption coefficients were calculated from the measured transmission curves, taking into account Fresnel losses due to multiple reflections at the crystal surfaces.

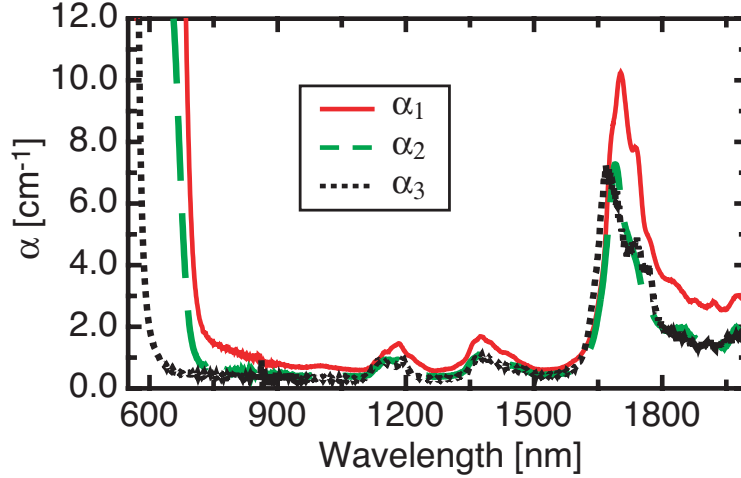


Figure 8.4: Absorption coefficients of DSTMS. Absorption coefficients α_1 (solid curve), α_2 (dashed curve), and α_3 (dotted curve) of DSTMS as a function of the wavelength λ .

As shown in Fig. 8.4, the absorption at telecommunication wavelengths is below 0.7 cm^{-1} for all polarizations. In the near infrared wavelength range weak absorption bands at about 1.15, 1.4 and 1.7 μm are present, corresponding to overtones of the C-H stretching vibration at 3.3 μm . The cutoff wavelength, which we defined for an absorption of 12 cm^{-1} , is at 685 nm for α_1 , 655 nm for α_2 , and 575 nm for α_3 . The relatively large shift can be explained by the orientation of the nonlinear optical chromophores.

8.5 Nonlinear optical properties

Since DSTMS belongs to the point-group symmetry m , the nonzero tensor elements $d_{ijk} = \frac{1}{2}\chi_{ijk}^{(2)}$ of the nonlinear optical susceptibility tensor elements are consequently d_{111} , d_{122} , d_{133} , $d_{131} = d_{113}$, $d_{232} = d_{223}$, $d_{212} = d_{221}$, d_{311} , d_{322} , d_{333} and $d_{313} = d_{331}$, resulting in an induced nonlinear optical polarization at the second-harmonic frequency $\mathbf{P}^{2\omega}$ with the components of

$$P_1^{2\omega} = \epsilon_0(d_{111}E_1^2 + d_{122}E_2^2 + d_{133}E_3^2 + 2d_{113}E_1E_3) \quad (8.4)$$

$$P_2^{2\omega} = \epsilon_0(2d_{223}E_2E_3 + 2d_{212}E_1E_2) \quad (8.5)$$

$$P_3^{2\omega} = \epsilon_0(d_{311}E_1^2 + d_{322}E_2^2 + d_{333}E_3^2 + 2d_{313}E_1E_3) \quad (8.6)$$

where E_i are the components of the incident electric field \mathbf{E}^ω at the fundamental frequency ω and ϵ_0 is the electric permittivity of free space.

The nonlinear optical tensor elements were measured by the standard Maker-fringe technique generalized for anisotropic absorbing materials [9]. As fundamental wavelength, the first Stokes line at $\lambda = 1907$ nm of a high-pressure Raman cell filled with H_2 was used, pumped by a Q -switched Nd:YAG laser operating at 1064 nm. A typical Maker-fringe curve obtained by measuring the d_{111} element of DSTMS is shown in Fig. 8.5.

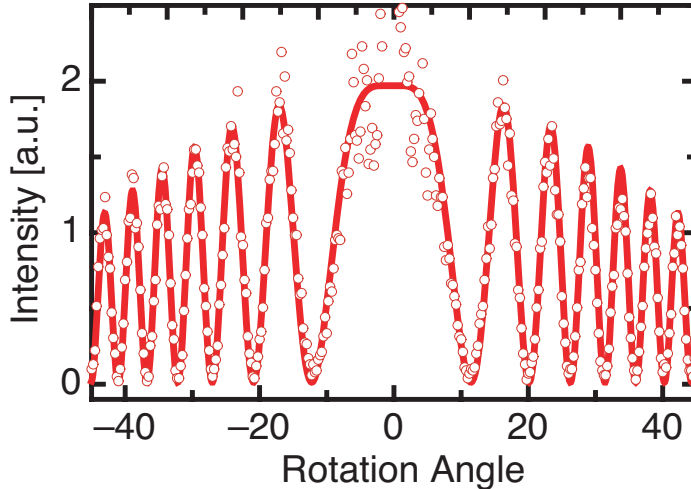


Figure 8.5: Maker-fringe measurement. Maker-fringe curve obtained by rotating a c plate DSTMS crystal around the dielectric x_1 axis. The impinged fundamental beam at $1.9 \mu\text{m}$ as well as the generated second-harmonic light at $0.95 \mu\text{m}$ were s -polarized.

With c plates of DSTMS the nonlinear optical susceptibility elements d_{111} , d_{212} , and d_{122} could be measured by selecting the appropriate polarization of the fundamental and of the second-harmonic waves. All measurements were referenced to quartz with $d_{111} = 0.277$ pm/V at $1.9 \mu\text{m}$ [42]. The obtained tensor elements and the corresponding coherence lengths l_c are summarized in Table 8.2.

DSTMS has a high second-order nonlinear optical activity. As expected, the nonlinear optical tensor element d_{111} is the largest owing to the preferential alignment of the chromophores along the x_1 axis of the crystal. The measured values are comparable to the ones of DAST with $d_{111} = 210 \pm 55$ pm/V, $d_{122} = 32 \pm 4$ pm/V, and $d_{212} = 25 \pm 3$ pm/V [42].

With the obtained results on the nonlinear optical susceptibilities and the dispersion of the refractive indices the electronic contribution to the electro-optic effect can be determined. In organic materials the electronic contribution to the electro-optic effect is dominant, in DAST it is about 75% of the low-frequency electro-optic coefficient r^T [19]. The electronic contribution to the electro-optic effect r^e at frequency ω can be estimated by using the quantum-mechanical two-level model for the dispersion of the microscopic nonlinearities [6] and the oriented-gas

model for the relation between the microscopic and macroscopic nonlinearities [19]. This model is related to the nonlinear optical tensor components d_{ijk} by

$$r_{ijk}^e(\omega) = \frac{-4}{n_{\omega,i}^2 n_{\omega,j}^2} \frac{f_i^\omega f_j^\omega f_k^0}{f_k^{2\omega'} f_j^{\omega'} f_i^{\omega'}} \frac{(3\omega_{eg}^2 - \omega^2)(\omega_{eg}^2 - \omega'^2)(\omega_{eg}^2 - 4\omega'^2)}{3(\omega_{eg}^2 - \omega^2)^2 \omega_{eg}^2} d_{kij}(-2\omega', \omega', \omega'), \quad (8.7)$$

where $f_i^\omega = [(n_i^\omega)^2 + 2]/3$ is the local field correction at frequency ω for light polarized along the dielectric x_i axis in the Lorentz approximation and $\omega_{eg} = 2\pi\nu_0$. Using the obtained values we get $r_{111}^e = 37 \pm 3$ pm/V. For DAST the same evaluation yields $r_{111}^e = 31 \pm 8$ pm/V at $1.9 \mu\text{m}$. Therefore, the electro-optic figure of merit $n_1^3 r_{111}^e$ of DSTMS, which is the important quantity concerning electro-optic modulation, is about 10% higher compared with the one of DAST.

	d_{111} [pm/V]	l_c^{111} [μm]	d_{122} [pm/V]	l_c^{122} [μm]	d_{212} [pm/V]	l_c^{212} [μm]	r_{111}^e [pm/V]	$n_1^3 r_{111}^e$ [pm/V]
DSTMS	214±20	3.6 ± 0.3	31±4	0.87 ± 0.03	35±4	2.7 ± 0.3	37±3	320±30
DAST	210±55	3.2 ± 0.3	32±4	0.67 ± 0.03	25±3	2.1 ± 0.2	31±8	290±75

Table 8.2: Nonlinear optical coefficients d_{ijk} and coherence lengths l_c of DSTMS and for comparison the corresponding values of DAST [42] as determined in an Maker-fringe experimental configuration at the fundamental wavelength of $1.9 \mu\text{m}$. The electronic contribution to the electro-optic coefficient r_{111}^e and the corresponding electro-optic figure of merit at $1.9 \mu\text{m}$ were calculated with Eq. (8.7).

8.6 Phase-matched parametric interaction

The favorable dispersion of DSTMS with $n_1 > n_2 > n_3$ and the relatively large off-diagonal elements d_{122} and d_{212} make efficient parametric generation of type I and II possible. The conditions that have to be fulfilled for efficient nonlinear interactions are energy conservation and momentum conservation (phase matching): $\omega_3 = \omega_1 + \omega_2$ and $\mathbf{k}_3 = \mathbf{k}_1 + \mathbf{k}_2$, respectively, where \mathbf{k}_i denotes the wave vector at frequency ω_i . For collinear interactions, for which all wave vectors are parallel to another, the phase matching condition is

$$n(\omega_3)\omega_3 = n(\omega_1)\omega_1 + n(\omega_2)\omega_2. \quad (8.8)$$

The nonlinear optical polarization \mathbf{P}^{ω_3} for sum-frequency generation from the fundamental waves $\mathbf{E}^{\omega_{1,2}}$ is described by

$$P_i^{\omega_3} = \epsilon_0 \sum_{ijk} 2d_{ijk}^{(\omega_3, \omega_1, \omega_2)} E_j^{\omega_1} E_k^{\omega_2}, \quad (8.9)$$

where d_{ijk} are the corresponding nonlinear optical tensor elements. For general directions of the wave vector and the polarizations in the crystal, the projection of the induced polarization

at frequency ω_3 along the direction of the electric field of the generated wave at ω_3 can be written as

$$|\mathbf{P}^{\omega_3}| = 2\epsilon_0 d_{\text{eff}} |\mathbf{E}^{\omega_1}| |\mathbf{E}^{\omega_2}|, \quad (8.10)$$

with

$$d_{\text{eff}} = \sum_{ijk} d_{ijk}^{(\omega_3, \omega_1, \omega_2)} \cos(\alpha_i^{\omega_3}) \cos(\alpha_j^{\omega_1}) \cos(\alpha_k^{\omega_2}), \quad (8.11)$$

where α_i^ω is the angle between the electric field vector at frequency ω and the axis i of the Cartesian coordinate system, in which d_{ijk} is given [101]. Since the electric field vectors are not perpendicular to the wave vectors \mathbf{k} in birefringent materials, the walk-off angles between the Poynting vectors and the wave vectors were taken into account for the calculation of the angles α_i .

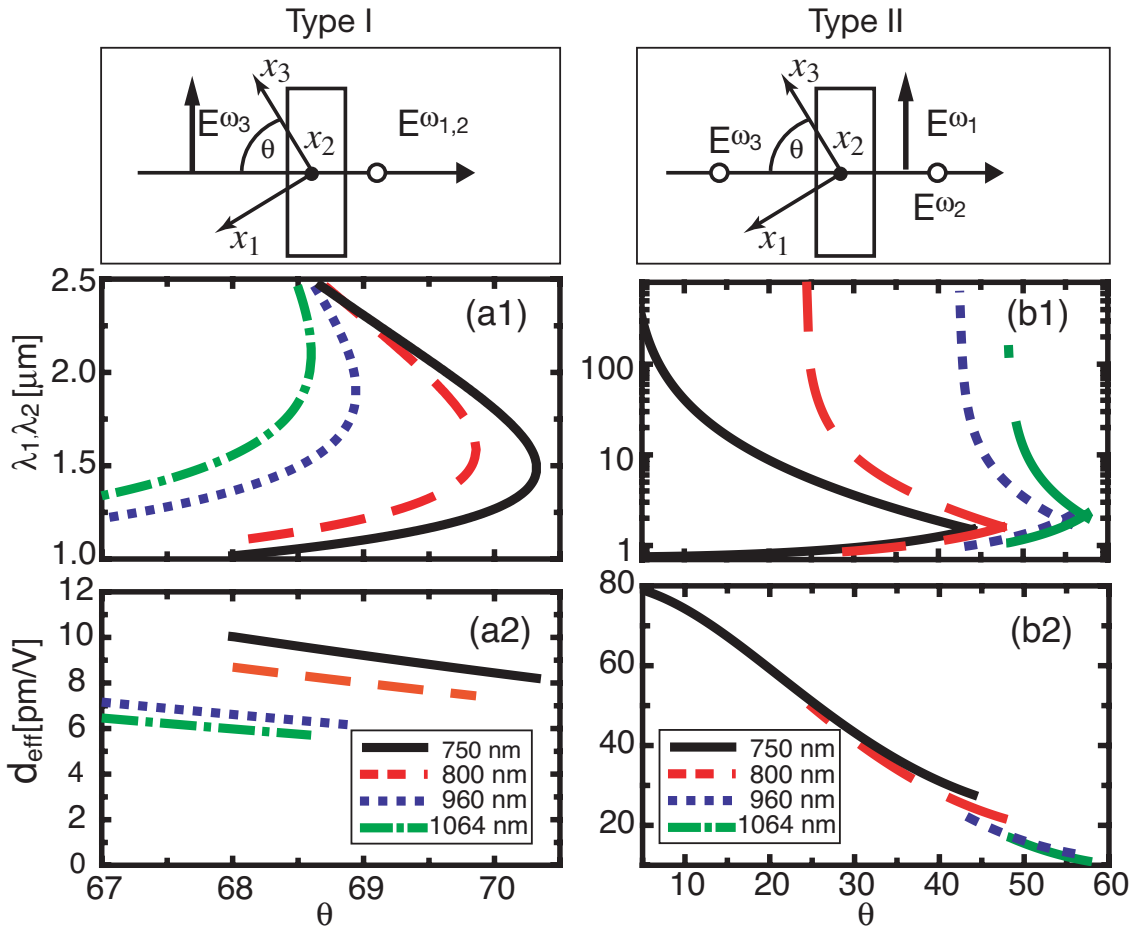


Figure 8.6: Parametric generation. Phase-matching curves for parametric light generation of type I (a1) and II (b1) as functions of the internal tuning angle θ for pumping wavelength of 750 nm (solid curve), 800 nm (dashed curve), 960 nm (dotted curve) and 1064 nm (dashed-dotted curve). The corresponding effective nonlinear optical coefficients d_{eff} are depicted in (a2) and (b2). The orientation of the samples and the polarizations of the interacting electric fields are depicted above the graphs.

In Fig. 8.6(a1) and (b1) the calculated phase-matching curves for parametric light generation of type I (the generated photons at λ_1 and λ_2 are of the same linear polarization) and II (the generated photons are of orthogonal linear polarization) as functions of the internal angle θ are shown. The solid curve corresponds to a pumping wavelength of $\lambda_3 = 750$ nm, the dashed curve to 800 nm, the dotted curve to 960 nm, and the dashed-dotted curve to a wavelength of 1064 nm, which are all emission lines of available high-power solid-state laser and diode sources. We can see that these sources are all well suited as pump wavelengths for parametric generation of light in DSTMS. The corresponding effective nonlinear optical coefficients d_{eff} were calculated with Eq. (8.11) taking into account the dispersion of the nonlinear optical coefficient by applying the quantum-mechanical two-level model [6]. Light in the wavelength range from 1 to 2.2 μm can be generated with type I phase matching by tuning the angle θ in a narrow range from 68° to 70.5° . Above 2.2 μm material absorption hinders an efficient generation of light. Type II phase matching offers the advantage of higher effective nonlinear optical coefficients, ranging from more than 10 to 40 pm/V compared with type I phase matching with 6-10 pm/V, whereas tuning of the angle θ in a broader range is required to access the whole wavelength range from 1 to 2.2 μm .¹

Compared with inorganic crystals LiNbO_3 with a nonlinear optical figure of merit of $\text{FM} = d_{\text{eff}}^2/n^3 \approx 3 \text{ pm}^2/\text{V}^2$ and BBO with $\text{FM} < 1 \text{ pm}^2/\text{V}^2$, which are often used for parametric light generation, DSTMS shows a 2 orders of magnitude higher figure of merit $\text{FM} \approx 160 \text{ pm}^2/\text{V}^2$ for the generation of $\lambda_1 = 1.5 \mu\text{m}$ by type II phase matching pumped with $\lambda_3 = 750$ nm.

8.7 Conclusions

We have determined the principal refractive indices of the recently developed organic nonlinear optical salt DSTMS in the wavelength range from 0.6 to 1.6 μm . A large anisotropy of the refractive index was measured, in agreement with the crystallographic packing of the nonlinear optical chromophores. The absorption coefficients have been determined in the wavelength range from 600 to 2000 nm. DSTMS shows very low absorption $\alpha < 0.7 \text{ cm}^{-1}$ at telecommunication wavelengths combined with a high electronic contribution to the electro-optic coefficient $r_{111}^e = 37 \text{ pm/V}$ and is therefore very interesting for high-speed photonic devices.

Furthermore, we have measured the nonlinear optical coefficients d_{111} , d_{122} , and d_{212} . DSTMS has a very high second-order susceptibility $d_{111} = 214 \pm 20 \text{ pm/V}$, comparable with that of the well-investigated DAST. Therefore and because of the easier and faster growth compared with DAST it is very promising for nonlinear optical applications including THz generation and detection. We have determined the phase-matching conditions for parametric light generation and have shown that DSTMS is well suited for optical parametric oscillation in the wavelength range from 1 to 2.2 μm because of large d_{eff} coefficients.

¹Note, that the refractive index dispersion in the far infrared and THz wavelength range was neglected for the calculations.

Chapter 9

Conclusions

The three different **waveguide structuring techniques**; photobleaching, ion implantation and direct electron beam patterning have been investigated, studied and successfully applied to the organic crystal DAST in order to realize planar and channel waveguides.

- **Photobleaching** of organic crystals is a very promising structuring technique, since a large reduction of the refractive index ($\Delta n_1 = -0.5$ at $1.55 \mu\text{m}$) can be obtained. Therefore, the method is well suited for the realization of high index contrast waveguides. Provided that thin organic crystalline DAST films are available, microrings with a diameter of $10 \mu\text{m}$ are feasible resulting in a free spectral range of about 20 nm. One advantage of photobleaching over standard photolithography is that only one illumination step is required to realize channel waveguides. For standard photolithography, on the other hand, several process steps are mandatory including a chemical or mechanical etching to transform the structure from the patterned photoresist into the DAST material. Therefore, the side walls of the bleached channel waveguides are generally smoother compared to the one produced by standard processing. At present the only drawback of photobleaching is the long illumination time required. Nevertheless, first experiments showed that the time required to realize waveguide structures can be dramatically reduced by the presence of oxygen. The bleaching process is fastened up by a factor of two to three under oxygen atmosphere of 0.9 bar compared to standard atmosphere. Therefore, increasing the process pressure may result in a further reduction of the illumination time, so that the total structuring time will be comparable to the one of standard photolithography. Since bleaching of DAST is a photooxidation process, the maximal depth achievable is limited by the indiffusion length of oxygen in DAST. Maximal bleaching depths of about $3 \mu\text{m}$ were attained for light polarized along the dielectric x_2 axis, which is sufficient for structuring thin organic films.
- **Ion implantation** has shown to be a valuable technique for the realization of planar waveguide structures in DAST. In contrast to inorganic materials, in which the refractive

index is reduced due to nuclear displacements at the end of the ion track, in organic crystals electronic excitations lead to molecular changes and hence to an alteration of the refractive index. Therefore, we can conclude that the implantation process in organic crystals is essentially different compared to inorganics. A refractive index barrier supporting waveguiding has been successfully realized at a depth of $9\ \mu\text{m}$ by low fluence $1\ \text{MeV}\ \text{H}^+$ implantation ($\phi = 1.25 \times 10^{14}\ \text{ions/cm}^2$) at an angle of 60° . Waveguiding has been demonstrated with losses of $7\ \text{dB/cm}$. The nonlinear optical properties are preserved to more than 90% in the waveguide core region as it has been shown by second-harmonic back reflection measurement on a wedged-polished sample surface. Electro-optical modulation in the produced waveguide structure has also been demonstrated. An essential advantage of ion implantation over thin film growth is the very accurate thickness control of the waveguide core, which can be achieved by tuning the ion implantation parameters. The thickness precision is in the range of a few tenths of micrometers. A further reduction of the barrier depth to about $6\ \mu\text{m}$ can be realized by lowering the implantation energy as it is shown in Appendix B in order to attain single mode behavior, which is a prerequisite for most photonic applications. Channel waveguides and Mach-Zehnder modulators have been realized subsequent to the ion implantation process by standard photolithography combined with reactive ion etching. At present, efficient coupling was only possible into structures with widths larger than $10\ \mu\text{m}$ due to a not so perfect edge quality. Therefore, the photobleaching technique could be a valid alternative to standard photolithography since the stability of the edge and the formed waveguides are better compared to the alone standing ridges which protrude from the sample surface. Furthermore, less process steps are required by using photobleaching. The low fluence ion implantation process is very attractive for the realization of planar waveguide structures owing to the short irradiation time of about 5 minutes on standard implanters. Since a fast standard thin film growth technique for DAST has not been found up to now, ion implantation is a promising technique for using DAST in integrated optics devices.

- **Direct electron beam patterning** is the most advanced structuring technique, owing to the fact that waveguide structures can be patterned in a single process step. Furthermore, electron beam patterning offers the benefit of sub wavelength - nanometer resolution. By using the newly developed concept of channel writing, waveguide structures have been successfully realized by direct electron beam patterning in organic materials. Channel waveguiding has been demonstrated at telecommunication wavelength ($\lambda = 1.5\ \mu\text{m}$). A maximal refractive index change of $\Delta n_1 = -0.3$ at a wavelength of $633\ \text{nm}$ has been measured obtained with an electron fluence of $2.6\ \text{mC/cm}^2$. Basic characterizations have been performed in order to relate the induced refractive index change to the deposited energy in the target material. The model introduced shows that the induced refractive index change depends linearly on the deposited energy. Based on this analysis, a single mode configuration has been simulated and proposed for future applications. Compared

to ion implantation combined with standard photolithography or photobleaching, electron beam patterning offers the advantage that channel waveguides can be realized in a single process step with very high resolution. In contrast to ion implantation, the waveguide core is not affected so that the nonlinear properties are completely preserved. Up to now, the main disadvantage is the relatively long exposure time. Nevertheless, since electron beam patterning becomes often used in research for the production of nanoscale devices such as photonic crystals, future exposure systems will possibly allow in-parallel exposure of different samples, which will fasten up the processing.

A first **electro-optic modulation** has been demonstrated in Mach-Zehnder integrated optical structures realized by direct electron beam patterning. At present the half wave voltage is still higher than 10 V, owing to a short interaction (arm) length of below 1 mm, and a low electric field strength, resulting from a relatively wide electrode spacing and a thick cladding layer. Modulators in DAST with a half wave voltage below 5 V should be feasible in near future by a proper electrode spacing of about the width of the waveguide core, a reduction of the buffer layer thickness, and an arm length of about 2 mm, which is considerably smaller compared to commercially available lithium niobate devices. Furthermore, DAST is well suited for high-speed electro-optic modulators. Therefore, we believe these results constitute an important step towards the utilization of organic nonlinear optical active crystals in integrated devices for telecommunication applications.

Beside waveguide structuring also more basic research on the development and the characterization of **new organic crystals**, to which the above mentioned structuring techniques can also be applied, has been made. Among the studied materials, DSTMS, which is a derivative of DAST, has shown to be more than a valid alternative due to the following reasons: DSTMS grows easily in large size bulk crystals of up to $30 \times 30 \times 3 \text{ mm}^3$ because of a faster nucleation and a higher solubility compared to DAST. The second-order nonlinearity measured at a wavelength of $1.9 \mu\text{m}$ is with $214 \pm 20 \text{ pm/V}$ slightly larger than the one reported for DAST. Hence, DSTMS is not only an efficient source for the generation of THz radiation by the nonlinear optical process of the optical rectification as it has been shown [90] but can also be utilized for the parametric generation of light in the wavelength range from $1 - 2.2 \mu\text{m}$ with effective nonlinear optical coefficients above 25 pm/V . Furthermore, DSTMS is a promising material for high-speed electro-optic applications because of a low material absorption at $1.5 \mu\text{m}$ ($\alpha < 0.7 \text{ cm}^{-1}$) combined with a low dielectric constant and a high electronic contribution to the electro-optic coefficient with $n^3 r_e = 320 \text{ pm/V}$ at a wavelength of $1.9 \mu\text{m}$.

Appendix A

Atmospheric dependence of the bleaching process

The dependence of the bleaching process on the surrounding atmosphere was observed by filling a vacuum chamber with different gases. The sample was illuminated for 3 hours at a wavelength of $\lambda_{\mathbf{B}} = 580$ nm with a peak power of about 2.8 W/cm². In the following table the gases used and the obtained bleaching depths are summarized.

Gas	Pressure	Depth
air	$p = 1.0$ bar	750 nm
air	$p = 0.1$ bar	0 nm
N ₂	$p = 0.9$ bar	0 nm
O ₂	$p = 0.9$ bar	1.5 – 1.8 μ m

Table A.1: Dependence of the bleaching process on the surrounding atmosphere.

No significant bleaching was observed at lowered air pressure of 0.1 bar and nitrogen atmosphere of 0.9 bar, whereas the bleaching process was fastened up under oxygen atmosphere (0.9 bar) by a factor two to three compared to normal air under atmospheric pressure. Therefore, we can conclude that photobleaching of DAST is a photooxidation process, whose depth is limited by the indiffusion length of oxygen. This result is an important finding regarding both, the photostability of integrated devices and the application of photostructuring for the realization of DAST waveguides.

Appendix B

Sample tilting in ion implantation and single mode waveguides

B1. Multiple implantations in organic crystals

The effect of multiple implantations with variation of the ion energy has been previously exploited to produce double or triple barrier layers in inorganic materials in order to decrease the tunneling losses of the guided light through the optical barrier into the substrate [71]. In contrast to inorganic crystalline materials, in which an amorphous layer is formed at the end of the ion track through nuclear energy deposition, organic crystals behave fundamentally different, since the refractive index is dominantly changed due to electronic excitations as already discussed in Chapter 4. Therefore, the effect of multiple implantations has also a different impact on the produced multiple barrier. Figure B.1 shows the calculated refractive index profile at the telecommunication wavelength of $\lambda = 1.55 \mu\text{m}$ for double implantation (full curve) obtained by 700 keV and 800 keV H^+ ion implantation at an angle of 60° . For comparison the corresponding profiles for single energy implantation (dotted and dashed curve) are depicted as well. The refractive index profiles were calculated as described in Chapter 5.

We can conclude by comparing these refractive index profiles that double energy implantation is not beneficial to implantation with a single ion energy. This is because the refractive index at the sample surface is also slightly reduced by H^+ ion implantation. The cumulated refractive index change of the multiple energy implantation results in a second peak at about $6.5 \mu\text{m}$, which is barely smaller than the refractive index at the surface. Therefore, the effective optical barrier is only marginally widened up by double energy implantation.

B2. Effect of sample tilting

During implantation, crystalline samples are normally oriented so that the implantation direction is not coinciding with one of the crystallographic axes in order to avoid channelling. We show here that in organic materials tilting has the beneficial effect of a more favorable energy

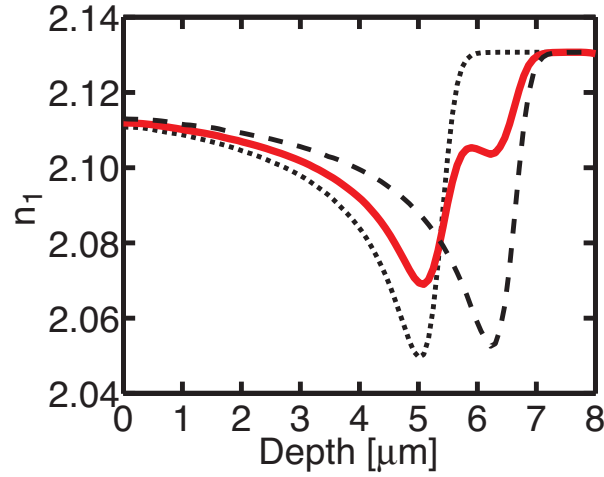


Figure B.1: Double barrier. The full curve represents the refractive index profile at a wavelength of $\lambda = 1.55 \mu\text{m}$ formed by double implantation with 700 keV and 800 keV H^+ ions with a fluence of $0.62 \cdot 10^{14}$ ions/cm² per energy at an angle of 60° . The dotted and dashed curves correspond to single energy implantation of 700 keV and 800 keV, respectively with a fluence of $1.25 \cdot 10^{14}$ ions/cm².

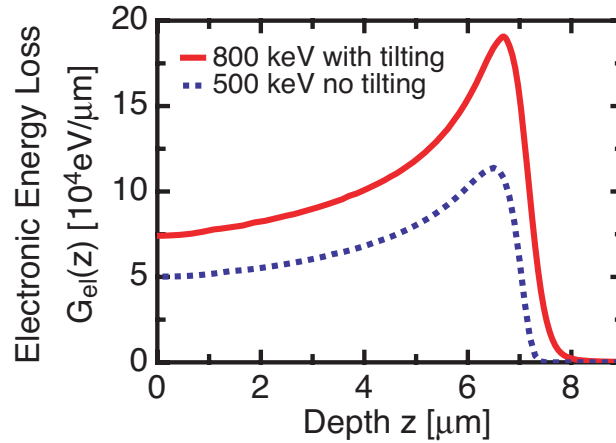


Figure B.2: Effect of sample tilting on the energy profiles. Deposited energy as a function of depth z for 500 keV H^+ ions (dashed curve) implanted under normal incidence and 800 keV H^+ ions (full curve) at an angle of 60° from normal incidence.

deposition profile compared to the one obtained by normal incidence. The model which relates the deposited energy to the induced refractive index profile is in detail described in Chapter 4. In Fig. B.2 the deposited energy profiles for 500 keV H^+ ions (dashed curve) implanted under normal incidence and 800 keV H^+ ions (full curve) implanted at an angle of 60° from normal incidence are shown. We aim for a small reduction of the refractive index in the waveguide core region combined with a well pronounced change of the refractive index in the barrier. The quantity of importance is therefore the ratio between the deposited energy at the peak position and the region closest to the sample surface. The ratio is 12% higher for the tilted sample compared to the profile obtained by normal incidence. Hence, the refractive index profile for the tilted configuration will have a higher refractive index contrast between waveguide core and barrier region and is therefore advantageous.

B3. Single mode configuration

Planar single mode waveguides are a prerequisite for the production of electro-optic photonic devices in order to attain a proper operation of them. The refractive index profile obtained by 1 MeV H^+ ion implantation is supporting two guided modes with low losses at a wavelength of $1.5 \mu\text{m}$ as shown in Chapter 5. Hence, the barrier depth has to be reduced to accomplish single mode waveguides. In Fig. B.3 the refractive index profile (full curve) of a single mode configuration is shown, obtainable by 800 keV H^+ ions implanted at an angle of 60° from normal incidence with a fluence of $1.25 \cdot 10^{14}$ ions/cm². The effective indices were calculated by the 2×2 matrix formalism and yield $n_{\text{eff}} = 2.103$ for the first mode with estimated losses below 1 dB/cm² [73, 79]. Higher order modes have estimated losses of above 25 dB/cm. A reduction of the waveguide core width by using lower energy ions would also result in a thinner barrier and hence leads to larger tunneling losses of above 1 dB/cm².

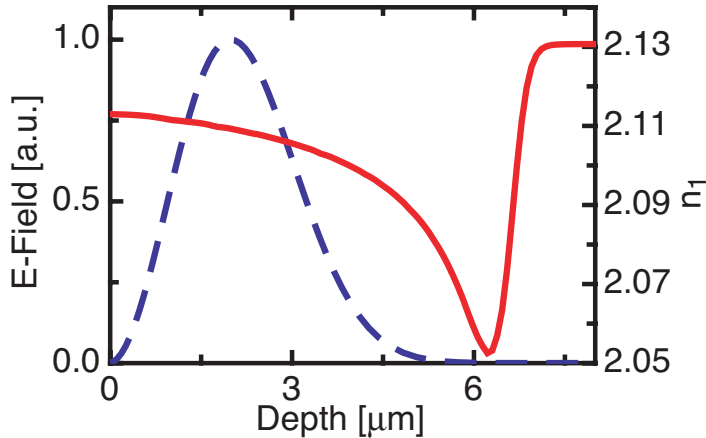


Figure B.3: Single mode structure. The full curve represents the refractive index profile at $1.5 \mu\text{m}$ obtained by $1.25 \cdot 10^{14}$ H^+ ions/cm² implantation with an energy of 800 keV. The dashed curve is the electric field of the corresponding first mode.

Appendix C

Ion implanted Mach-Zehnder modulators

Planar waveguides have been realized by ion implantation of 1 MeV H^+ ions at an angle of 60° . Subsequently, ridge waveguides and Mach-Zehnder modulators have been structured by standard photolithography. Owing to a peak refractive change at about $9\ \mu\text{m}$ depth, a high aspect ratio photoresist is required for ridge waveguide production. Furthermore, special care has to be taken that neither the photoresist nor its developer is attacking the organic crystal DAST. In this section the most important processing steps as well as essential structuring details are described.

C1. Theoretical consideration

Vertical confinement of light is ensured by the production of planar waveguides by H^+ ion implantation with a fluence of $\phi = 1.0 \times 10^{14}$ ions/cm². The refractive index profile for this fluence at a wavelength of 810 nm was calculated as described in Chapter 4. The profile was then transformed to a wavelength of $1.55\ \mu\text{m}$ with help of the model introduced in Chapter 5. Different waveguide geometries of a ridge waveguide structure were simulated by varying the width of the ridge W and its height H (Fig. C.1). The TE modes with the light polarized parallel to the dielectric x_1 axis were calculated with the full vectorial complex bend 2D mode solver of the integrated optics software OlympIOs. As over cladding SU-8 was chosen. Its refractive index at a wavelength of $1.55\ \mu\text{m}$ is 1.57 [102]. A systematic study of the mode confinement was made by varying the height H from 2 to $4\ \mu\text{m}$ in micrometer steps and the width W from 2 to $6\ \mu\text{m}$ in two micrometer steps. Higher and wider ridges generally lead to better confinement of the waveguide modes. Nevertheless, the achievable height of the structures is limited by the material properties of the photoresist. Furthermore, the structures should not be too wide in order to support only one guided mode so that a proper performance of the Mach-Zehnder modulators is guaranteed. The simulated losses showed the following features. For

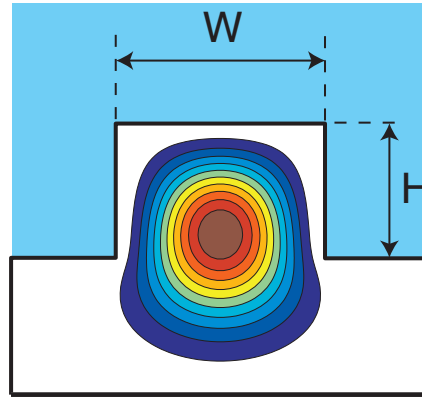


Figure C.1: Cross section of a ridge waveguide structure. The vertical confinement is realized by ion implantation. As overcladding SU-8 is used in order to reduce scattering losses and to protect the sample. The electric field strength of a simulated TE mode with light polarized along the dielectric x_1 axis is shown for the following waveguide ridge dimensions, $W = 6 \mu\text{m}$ and $H = 3.5 \mu\text{m}$.

- $H = 2 \mu\text{m}$: Only the waveguide with a width of $W = 6 \mu\text{m}$ has simulated losses of below 1 dB/cm.
- $H = 3 \mu\text{m}$ and $4 \mu\text{m}$: Waveguides with a width of $W = 2 \mu\text{m}$ have losses of over 15 dB/cm, whereas for $W = 4$ and $6 \mu\text{m}$ the losses are below 1 dB/cm and about 0.1 dB/cm, respectively.

Therefore, we can conclude that a ridge height of at least $3 \mu\text{m}$ and a minimal width of $4 \mu\text{m}$ is required in order to obtain low loss waveguiding performance. Figure C.1 shows an example of such an optimized waveguide profile with simulated losses of about 0.1 dB/cm.

C2. Structuring of ridge waveguides

Ridge channel waveguide structuring

The negative tone photoresist SU-8-5 from MicroChem was used for structuring DAST since it offers high aspect ratio processing and superb chemical and thermal stability. Nevertheless, the solvent of SU-8 is slightly attacking DAST. Therefore, a LOR-B3 lift-off resist (MicroChem) was used as a protective cladding and adhesion promoter for SU-8. Normally, the resist is pre- and post-baked on a hot plate. Since the DAST crystals used had a thickness of 3-4 mm and the heat dissipation is relatively low compared with Si wafers, the baking of the resist was done in an oven.

Ridge waveguides were structured by the following process steps that are also represented in Fig. C.2.

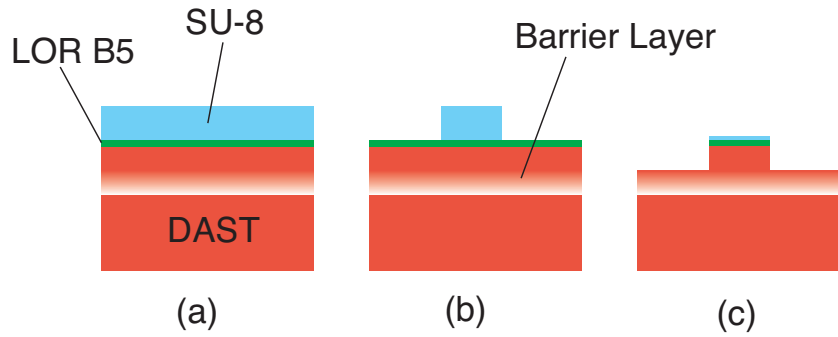


Figure C.2: Photolithography. (a) The implanted DAST sample is coated with an adhesion layer of LOR-B3 and subsequently with SU-8. (b) After the pre-exposure bake, exposure and post-exposure bake, the SU-8 photoresist is developed. (c) The waveguide structure is then transformed from the photoresist to the crystal by reactive ion etching.

- **Step 1:** Spinning of the adhesion promoter LOR-B3 at 6000 rpm (1') with a resulting film thickness of below 500 nm.
- **Step 2:** Functionalization of the surface with a Diener 100 W plasma generator (45'') with full power.
- **Step 3:** Spinning of the photoresist SU-8-5 at 5000 rpm (5') with a resulting thickness of about 4.4 μm .
- **Step 4:** Pre-exposure bake at 65°C (5') and 95°C (10').
- **Step 5:** Exposure (20''), using a Karl-Suss MJB3UV300 mask-aligner with 6 mW/cm² at 365 nm and 11 mW/cm² at 405 nm.
- **Step 6:** Post-exposure bake at 65°C (5') and 95°C (10').
- **Step 7:** Developing in SU8 developer (5-10'') and rinsing with isopropanol.
- **Step 8:** Post-exposure for 1'.
- **Step 9:** Reactive ion etching to transform the waveguide structures into DAST. After etching with the following combination of process gases on a Oxford Plasmalab 80 plus system : O₂ (35 sccm), N₂ (25 sccm) and CF₄ (5 sccm) with a power of 260 W for about 25 minutes, the etched depth in DAST was about 3.7 μm .

The impact of the etching process on different process gases was also investigated. Ar⁺ showed a too low sputtering rate. With pure oxygen sputtering an accumulation of debris on the SU-8 photoresist was observed, and by using CF_x, particles of DAST remained on the sample surface. Cleaning was only possible by applying strong shear forces by which the

sample surface was destroyed. Therefore, a combination of different gases showing the best etching performance was chosen.

Electrode patterning

Subsequent to the ridge waveguide structuring electrodes were patterned by using the photoresist AZ-5214E from MicroChem. Prior to the spinning of the AZ resist the ridge waveguides were protected with a SU-8 cladding.

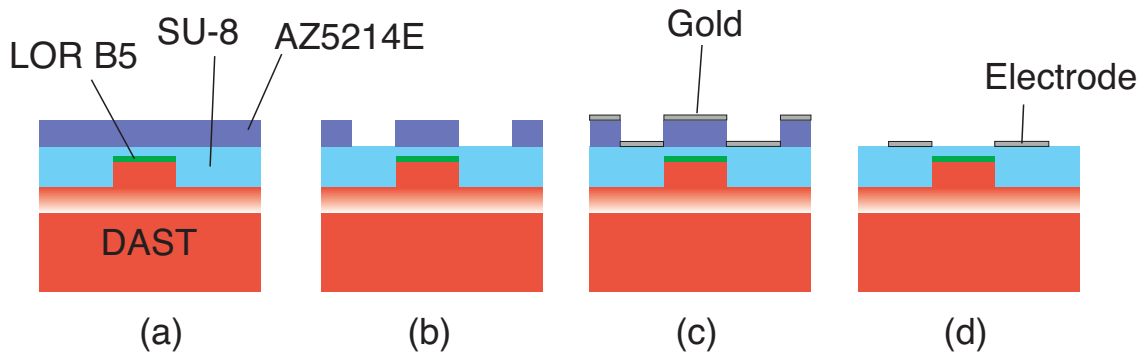


Figure C.3: Electrode patterning. (a) Protecting of the ridge waveguide with a SU-8 over cladding, followed by spinning AZ-5214E photoresist. (b) Baking of the resist, exposure and development of the structures. (c) Deposition of a gold layer. (d) Development of the electrodes in acetone.

The following procedure, which is depicted in Fig. C.3, was performed

- **Step 1:** Spinning of a SU-8 overcladding at 3000 rpm (5').
- **Step 2:** Pre-bake, exposure and post-bake of the SU-8 as described under ridge channel waveguide structuring.
- **Step 3:** Spinning of photoresist AZ-5214E at 5000 rpm (1') with a resulting thickness of about $1\ \mu\text{m}$.
- **Step 4:** Pre-exposure bake at 65°C (5') and 110°C (10').
- **Step 5:** Exposure for 30".
- **Step 6:** Developing in AZ-726 (30"), stopping of the process in water.
- **Step 7:** Gold electrode deposition; first 5 nm Cr are deposited in order to obtain a better sticking of the gold on the SU-8 and AZ photoresist.
- **Step 8:** Development in acetone; the side faces of DAST were covered with a thin paraffin layer and then the DAST crystal was put in acetone in order to remove AZ-5214E and the thin layer of gold on it. SU-8 is not attacked by acetone and therefore the deposited gold remains on it.

C3. Results and discussion

Channel ridge waveguides as well as Mach-Zehnder modulators with interaction lengths (arm length) of 0.5 mm and 1.0 mm between the optical wave and the modulation field were produced. The waveguides had a ridge height of $H = 3.7 \mu\text{m}$. The waveguide width W was varied from 3 – 10 μm . A series of Mach-Zehnder modulators is shown in Fig. C.4. After the structuring of the Mach-Zehnder modulators and the patterning of the corresponding electrodes, sharp edges were polished and light coupled into the waveguide structures by conventional end-fire coupling. At present, light could be only coupled into waveguides with widths of 10 – 30 μm , see also Chapter 4. The edge showed to have a too poor quality in order to efficiently couple waveguides with lower widths.

At the moment we are working on improving the sharp edge polishing in order to also couple light into waveguides with smaller dimensions.



Figure C.4: Mach-Zehnder modulators. The ridge waveguides have width from 3 to 10 μm .

Bibliography

- [1] T. Schneider, *Nonlinear Optics in Telecommunication* (Springer Verlag, Berlin, 2004).
- [2] T. D. Kim, J. D. Luo, J. W. Ka, S. Hau, Y. Q. Tian, Z. W. Shi, N. M. Tucker, S. H. Jang, J. W. Kang, and A. K. Y. Jen, “Ultralarge and thermally stable electro-optic activities from Diels-Alder crosslinkable polymers containing binary chromophore systems,” *Advanced Materials* **18**(22), 3038–3042 (2006).
- [3] J. Jackson, *Classical Electrodynamics* (John Wiley & Sons, New York, 1975).
- [4] D. Mills, *Nonlinear Optics* (Springer Verlag, Berlin, 1998).
- [5] R. W. Boyd, *Nonlinear Optics* (Academic Press, Boston, 1992).
- [6] C. Bosshard, K. Sutter, P. Prêtre, J. Hulliger, M. Flörsheimer, P. Kaatz, and G. P., *Organic Nonlinear Optical Materials* (Gordon and Breach Science Publishers, Amsterdam, 1995).
- [7] P. Günter, ed., *Nonlinear Optical Effects and Materials* (Springer Verlag, Berlin, 2000).
- [8] N. Blombergen and P. S. Pershan, “Light waves at boundary of nonlinear media,” *Physical Review* **128**(2), 606–622 (1962).
- [9] J. Jerphagnon and S. K. Kurtz, “Maker fringes - A detailed comparison of theory and experiment for isotropic and uniaxial crystals,” *Journal of Applied Physics* **41**(4), 1667–1681 (1970).
- [10] W. N. Herman and L. M. Hayden, “Maker fringes revisited - 2nd-harmonic generation from birefringent or absorbing materials,” *Journal of the Optical Society of America B-Optical Physics* **12**(3), 416–427 (1995).
- [11] M. Braun, F. Bauer, T. Vogtmann, and M. Schwoerer, “Detailed analysis of second-harmonic-generation Maker fringes in biaxially birefringent materials by a 4X4 matrix formulation,” *Journal of the Optical Society of America B-Optical Physics* **15**(12), 2877–2884 (1998).

- [12] D. W. Berreman, "Optics in stratified and anisotropic media - 4x4-matrix formulation," *Journal of the Optical Society of America* **62**(4), 502–510 (1972).
- [13] J. Zyss and J. L. Oudar, "Relations between microscopic and macroscopic lowest-order optical nonlinearities of molecular-crystals with one-dimensional or two-dimensional units," *Physical Review A* **26**(4), 2028–2048 (1982).
- [14] C. J. F. Boettcher, *Theory of Electric Polarization* (Elsevier, Amsterdam, 1952).
- [15] J. F. Ward, "Calculation of nonlinear optical susceptibilities using diagrammatic perturbation theory," *Reviews of Modern Physics* **37**(1), 1–18 (1965).
- [16] J. L. Oudar and J. Zyss, "Structural Dependence Of Nonlinear-Optical Properties Of Methyl-(2,4-Dinitrophenyl)-Aminopropanoate Crystals," *Physical Review A* **26**(4), 2016–2027 (1982c).
- [17] A. Yariv, *Quantum Electronics* (Wiley, New York, 1989).
- [18] C. Herzog, S. Aravazhi, A. Guarino, A. Schneider, G. Poberaj, and P. Günter, "Epitaxial K_{1-x}NaxTa_{0.66}Nb_{0.34}O₃ thin films for optical waveguiding applications," *Journal Of The Optical Society Of America B-Optical Physics* **24**(4), 829–832 (2007).
- [19] C. Bosshard, R. Spreiter, L. Degiorgi, and P. Günter, "Infrared and Raman spectroscopy of the organic crystal DAST: Polarization dependence and contribution of molecular vibrations to the linear electro-optic effect," *Physical Review B* **66**(20), 205,107 (2002).
- [20] B. E. A. Saleh and M. C. Teich, *Fundamentals of Photonics* (Wiley, New York, 1991).
- [21] A. Yariv, *Optical Electronics in Modern Commuications* (Oxford University Press, New York, 1997).
- [22] S. J. Chang, C. L. Tsai, Y. B. Lin, J. F. Liu, and W. S. Wang, "Improved electrooptic modulator with ridge structure in X-cut LiNbO₃," *Journal of Lightwave Technology* **17**(5), 843–847 (1999).
- [23] I. P. Kaminow and T. L. Koch, eds., *Optical Fiber and Telecommunication IIIB* (Academic Press, New York, 1997).
- [24] D. M. Gill and A. Chowdhury, "Electro-optic polymer-based modulator design and performance for 40 Gb/s system applications," *Journal of Lightwave Technology* **20**(12), 2145–2153 (2002).
- [25] G. P. Agrawal, *Fiber-Optics Communication Systems* (John Wiley & Sons, New York, 2002).

- [26] Y. Q. Shi, C. Zhang, H. Zhang, J. H. Bechtel, L. R. Dalton, B. H. Robinson, and W. H. Steier, “Low (sub-1-volt) halfwave voltage polymeric electro-optic modulators achieved by controlling chromophore shape,” *Science* **288**(5463), 119–122 (2000).
- [27] Y. Enami, C. T. Derose, D. Mathine, C. Loychik, C. Greenlee, R. A. Norwood, T. D. Kim, J. Luo, Y. Tian, A. K. Y. Jen, and N. Peyghambarian, “Hybrid polymer/sol-gel waveguide modulators with exceptionally large electro-optic coefficients,” *Nature Photonics* **1**(3), 180–185 (2007).
- [28] F. Pan, G. Knöpfle, C. Bosshard, S. Follonier, R. Spreiter, M. S. Wong, and P. Günter, “Electro-optic properties of the organic salt 4-N,N-dimethylamino-4'-N'-methyl-stilbazolium tosylate,” *Applied Physics Letters* **69**, 13–15 (1996).
- [29] M. Jazbinsek and M. Zgonik, “Material tensor parameters of LiNbO₃ relevant for electro- and elasto-optics,” *Applied Physics B-Lasers and Optics* **74**(4-5), 407–414 (2002).
- [30] M. Lee, H. E. Katz, C. Erben, D. M. Gill, P. Gopalan, J. D. Heber, and D. J. McGee, “Broadband modulation of light by using an electro-optic polymer,” *Science* **298**(5597), 1401–1403 (2002).
- [31] A. Guarino, *Electro-optic Microring Resonators in Inorganic Crystals for Photonic Applications, PhD. Thesis* (ETH Zürich, 2007).
- [32] A. Guarino, G. Poberaj, D. Rezzonico, R. Degl’Innocenti, and P. Günter, “Electro-optically tunable microring resonators in lithium niobate,” *Nature Photonics* **1**(7), 407–410 (2007).
- [33] H. Tazawa, Y. H. Kuo, I. Dunayevskiy, J. D. Luo, A. K. Y. Jen, H. R. Fetterman, and W. H. Steier, “Ring resonator-based electrooptic polymer traveling-wave modulator,” *Journal of Lightwave Technology* **24**(9), 3514–3519 (2006).
- [34] A. Leinse, M. B. J. Diemeer, A. Rousseau, and A. Driessen, “A novel high-speed polymeric EO modulator based on a combination of a microring resonator and an MZI,” *IEEE Photonics Technology Letters* **17**(10), 2074–2076 (2005).
- [35] B. Bortnik, Y. C. Hung, H. Tazawa, B. J. Seo, J. D. Luo, A. K. Y. Jen, W. H. Steier, and H. R. Fetterman, “Electrooptic polymer ring resonator modulation up to 165 GHz,” *IEEE Journal Of Selected Topics In Quantum Electronics* **13**(1), 104–110 (2007).
- [36] Q. F. Xu, B. Schmidt, S. Pradhan, and M. Lipson, “Micrometre-scale silicon electro-optic modulator,” *Nature* **435**(7040), 325–327 (2005).
- [37] Q. F. Xu, B. Schmidt, J. Shakya, and M. Lipson, “Cascaded silicon micro-ring modulators for WDM optical interconnection,” *Optics Express* **14**(20), 9430–9435 (2006).

- [38] K. Okamoto, *Fundamentals of Optical Waveguides* (Academic Press, New York, 2000).
- [39] F. Michelotti, A. Driessen, and M. Bertolotti, *Microresonators as Building Blocks for VLSI Photonics* (AIP Conference Proceedings, Melville, New York, 2004).
- [40] I. L. Gheorma and R. M. Osgood, "Fundamental limitations of optical resonator based high-speed EO modulators," *Ieee Photonics Technology Letters* **14**(6), 795–797 (2002).
- [41] S. R. Marder, J. W. Perry, and W. P. Schaefer, "Synthesis of organic salts with large 2nd-order optical nonlinearities," *Science* **245**(4918), 626–628 (1989).
- [42] U. Meier, M. Bösch, C. Bosshard, F. Pan, and P. Günter, "Parametric interactions in the organic salt 4-N, N-dimethylamino-4'-N'-methyl-stilbazolium tosylate at telecommunication wavelengths," *Journal of Applied Physics* **83**, 3486–3489 (1998).
- [43] G. L. Bryant, J. C. P. Yakymyshyn, and K. R. Stewart, "Structure of 4'-dimethylamino-4-methyl-4-azastilbenium p-toluenesulfonate hydrate," *Acta Crystallographica* **C49**, 350–351 (1993).
- [44] F. Pan, M. S. Wong, C. Bosshard, and P. Günter, "Crystal growth and characterization of the organic salt 4-N,N-dimethylamino-4'-N'-methyl-stilbazolium tosylate (DAST)," *Advanced Materials* **8**(7), 592–595 (1996).
- [45] G. Knöpfle, R. Schlessler, R. Ducret, and P. Günter, "Optical and nonlinear optical properties of 4'-dimethylamino -N-methyl-stilbazolium tosylate (DAST) crystals," *Nonlinear Optics* **9**, 143–149 (1995).
- [46] P. Laveant, C. Medrano, B. Ruiz, and P. Günter, "Rainbow photonics - Growth of nonlinear optical DAST crystals," *Chimia* **57**(6), 349–351 (2003).
- [47] M. Thakur, J. J. Xu, A. Bhowmik, and L. G. Zhou, "Single-pass thin-film electro-optic modulator based on an organic molecular salt," *Applied Physics Letters* **74**(5), 635–637 (1999).
- [48] M. Thakur, Y. Shani, G. C. Chi, and O. K., "Thin single crystal films of organics; waveguiding in PTS films," *Synthetic Metals* **28**, D595–D604 (1989).
- [49] L. G. Zhou and M. Thakur, "Molecular orientation in single crystal thin films of N-(4-nitrophenyl)-(L)-prolinol," *Journal of Materials Research* **13**(1), 131–134 (1998).
- [50] M. Deutsch, M. C. Gerstenberg, H. F. Gossenberger, V. S. Ban, and S. R. Forrest, "Macroscopically ordered thin films of an organic salt grown by low-pressure organic vapor-phase deposition," *Journal of Crystal Growth* **203**(3), 412–420 (1999).
- [51] M. Baldo, M. Deutsch, P. Burrows, H. Gossenberger, M. Gerstenberg, V. Ban, and S. Forrest, "Organic vapor phase deposition," *Advanced Materials* **10**(18), 1505–1514 (1998).

-
- [52] R. Schlessler, T. Dietrich, Z. Sitar, F. Gitmans, A. Kundig, L. Eng, B. Munch, and P. Günter, “Organic molecular-beam deposition of highly nonlinear-optical 4'-nitrobenzylidene-3-acetamino-4-methoxy-aniline,” *Journal of Applied Physics* **78**(8), 4943–4947 (1995).
- [53] S. R. Forrest, P. E. Burrows, A. Stroustrup, D. Strickland, and V. S. Ban, “Intense second harmonic generation and long-range structural ordering in thin films of an organic salt grown by organic vapor phase deposition,” *Applied Physics Letters* **68**(10), 1326–1328 (1996).
- [54] F. Pan, K. McCallion, and M. Chiappetta, “Waveguide fabrication and high-speed in-line intensity modulation in 4-N,N-4'-dimethylamino-4'-N'-methyl-stilbazolium tosylate,” *Applied Physics Letters* **74**(4), 492–494 (1999).
- [55] S. Manetta, M. Ehrensperger, C. Bosshard, and P. Günter, “Organic thin film crystal growth for nonlinear optics: present methods and exploratory developments,” *Comptes Rendus Physique* **3**(4), 449–462 (2002).
- [56] R. Spreiter, C. Bosshard, F. Pan, and P. Günter, “High-frequency response and acoustic phonon contribution of the linear electro-optic effect in DAST,” *Optics Letters* **22**(8), 564–566 (1997).
- [57] A. Schneider, I. Biaggio, and P. Günter, “Optimized generation of THz pulses via optical rectification in the organic salt DAST,” *Optics Communications* **224**(4-6), 337–341 (2003).
- [58] A. Schneider, M. Neis, M. Stillhart, B. Ruiz, R. U. A. Khan, and P. Günter, “Generation of terahertz pulses through optical rectification in organic DAST crystals: theory and experiment,” *Journal of the Optical Society of America B-Optical Physics* **23**(9), 1822–1835 (2006).
- [59] A. Schneider, M. Stillhart, and P. Günter, “High efficiency generation and detection of terahertz pulses using laser pulses at telecommunication wavelengths,” *Optics Express* **14**(12), 5376–5384 (2006).
- [60] T. Kaino, B. Cai, and K. Takayama, “Fabrication of DAST channel optical waveguides,” *Advanced Functional Materials* **12**(9), 599–603 (2002).
- [61] P. Dittrich, R. Bartlome, G. Montemezzani, and P. Günter, “Femtosecond laser ablation of DAST,” *Applied Surface Science* **220**(1-4), 88–95 (2003).
- [62] W. Geis, R. Sinta, W. Mowers, S. J. Deneault, M. F. Marchant, K. E. Krohn, S. J. Spector, D. R. Calawa, and T. M. Lyszczarz, “Fabrication of crystalline organic waveguides with an exceptionally large electro-optic coefficient,” *Applied Physics Letters* **84**(19), 3729–3731 (2004).

- [63] L. Mutter, M. Jazbinsek, M. Zgonik, U. Meier, C. Bosshard, and P. Günter, “Photo-bleaching and optical properties of organic crystal 4-N, N-dirnethylamino-4 ’-N ’-methyl stilbazolium tosylate,” *Journal of Applied Physics* **94**(3), 1356–1361 (2003).
- [64] B. Cai, T. Hattori, H. H. Deng, K. Komatsu, C. Zawadzki, N. Keil, and T. Kaino, “Refractive index control and grating fabrication of 4 ’-N,N-dimethylamino-N-methyl-4-stilbazolium tosylate crystal,” *Japanese Journal of Applied Physics Part 2-Letters* **40**(9AB), L964–L966 (2001).
- [65] T. Kaino, K. Takayama, B. Cai, and K. Komatsu, “Fabrication of nonlinear optical waveguide,” *Ferroelectrics* **257**(1-4), 13–26 (2001).
- [66] K. Komatsu, K. Takayama, B. Cai, and T. Kaino, “Waveguide fabrications of 4-(4-dimethylaminostyryl)-1-methylpyridinium tosylate (DAST) crystal,” *Ieice Transactions On Electronics* **E85C**(6), 1258–1263 (2002).
- [67] A. K. Bhowmik, J. J. Xu, and M. Thakur, “Polarized optical absorption and photoluminescence measurements in single-crystal thin films of 4’-dimethylamino-N-methyl-4-stilbazolium tosylate,” *Applied Physics Letters* **75**(21), 3291–3293 (1999).
- [68] S. Follonier, M. Fierz, I. Biaggio, U. Meier, C. Bosshard, and P. Günter, “Structural, optical, and electrical properties of the organic molecular crystal 4-N,N-dimethylamino-4 ’-N ’-methyl stilbazolium tosylate,” *Journal of the Optical Society of America B-Optical Physics* **19**(9), 1990–1998 (2002).
- [69] L. Mutter, A. Guarino, M. Jazbinsek, M. Zgonik, P. Günter, and M. Dobeli, “Ion implanted optical waveguides in nonlinear optical organic crystal,” *Optics Express* **15**(2), 629–638 (2007).
- [70] P. D. Townsend, “An overview of ion-implanted optical waveguide profiles,” *Nuclear Instruments & Methods in Physics Research Section B-Beam Interactions with Materials and Atoms* **46**(1-4), 18–25 (1990).
- [71] D. Fluck, D. H. Jundt, P. Günter, M. Fleuster, and C. Buchal, “Modeling of refractive-index profiles of He⁺ ion-implanted KNbO₃ waveguides based on the irradiation parameters,” *Journal of Applied Physics* **74**(10), 6023–6031 (1993).
- [72] C. Solcia, D. Fluck, T. Pliska, P. Günter, S. Bauer, M. Fleuster, L. Beckers, and C. Buchal, “The refractive-index distribution $n_c(z)$ of ion-implanted KNbO₃ waveguides,” *Optics Communications* **120**(1-2), 39–46 (1995).
- [73] P. Townsend, P. Chandler, and Z. L., *Optical Effects of Ion Implantation* (Cambridge U. Press, Cambridge, 1994).

-
- [74] L. Zhang, P. D. Townsend, P. J. Chandler, and J. R. Kulisch, "Ion-implanted waveguides in polymethylmethacrylate," *Journal of Applied Physics* **66**(9), 4547–4548 (1989).
- [75] A. Guarino and P. Günter, "Nondestructive method for the characterization of ion-implanted waveguides," *Optics Letters* **30**(18), 2412–2414 (2005).
- [76] P. Townsend, "Development of ion implantation for optical applications," *Vacuum* **51**, 301–304 (1998).
- [77] D. Fluck, T. Pliska, M. Kupfer, and P. Günter, "Depth profile of the nonlinear-optical susceptibility of ion-implanted KNbO₃ waveguides," *Applied Physics Letters* **67**(6), 748–750 (1995).
- [78] J. Olivares, A. Garcia-Navarro, G. Garcia, A. Mendez, F. Agullo-Lopez, A. Garcia-Cabanes, M. Carrascosa, and O. Caballero, "Nonlinear optical waveguides generated in lithium niobate by swift-ion irradiation at ultralow fluences," *Optics Letters* **32**(17), 2587–2589 (2007).
- [79] M. Ramadas, E. Garmire, A. K. Ghatak, K. Thyagarajan, and S. M. R., "Analysis of absorbing and leaky planar waveguides: a novel method," *Optics Letters* **14**, 376–378 (1989).
- [80] A. J. Houghton and P. D. Townsend, "Optical-waveguides formed by low-energy electron-irradiation of silica," *Applied Physics Letters* **29**(9), 565–566 (1976).
- [81] S. G. Blanco, A. Glidle, J. H. Davies, J. S. Aitchison, and J. M. Cooper, "Electron-beam-induced densification of Ge-doped flame hydrolysis silica for waveguide fabrication," *Applied Physics Letters* **79**(18), 2889–2891 (2001).
- [82] K. Komatsu, T. Abe, O. Sugihara, and T. Kaino, "Waveguide pattern formation in organic nonlinear optical crystal by electron beam irradiation," *Proceedings of SPIE* **5724**, 131–138 (2005).
- [83] S. R. Marder, C. B. Gorman, F. Meyers, J. W. Perry, G. Bourhill, J. L. Bredas, and B. M. Pierce, "A unified description of linear and nonlinear polarization in organic polymethine dyes," *Science* **265**(5172), 632–635 (1994).
- [84] J. Zyss, ed., *Molecular Nonlinear Optics* (Academic Press, New York, 1994).
- [85] B. J. Coe, J. A. Harris, I. Asselberghs, K. Wostyn, K. Clays, A. Persoons, B. S. Brun-schwig, S. J. Coles, T. Gelbrich, M. E. Light, M. B. Hursthouse, and K. Nakatani, "Quadratic optical nonlinearities of N-methyl and N-aryl pyridinium salts," *Advanced Functional Materials* **13**(5), 347–357 (2003).

- [86] M. S. Wong, F. Pan, M. Bosch, R. Spreiter, C. Bosshard, P. Günter, and V. Gramlich, "Novel electro-optic molecular cocrystals with ideal chromophoric orientation and large second-order optical nonlinearities," *Journal Of The Optical Society Of America B-Optical Physics* **15**(1), 426–431 (1998).
- [87] S. R. Marder, J. W. Perry, and C. P. Yakymyshyn, "Organic salts with large 2nd-order optical nonlinearities," *Chemistry of Materials* **6**(8), 1137–1147 (1994).
- [88] S. Okada, K. Nogi, Anwar, K. Tsuji, X. M. Duan, H. Oikawa, H. Matsuda, and H. Nakanishi, "Ethyl-substituted stilbazolium derivatives for second-order nonlinear optics," *Japanese Journal of Applied Physics Part 1-Regular Papers Short Notes & Review Papers* **42**(2A), 668–671 (2003).
- [89] Z. Yang, S. Aravazhi, A. Schneider, P. Seiler, M. Jazbinsek, and P. Günter, "Single crystals of stilbazolium derivatives for second-order nonlinear optics," *Advanced Functional Materials* **15**(7), 1072–1076 (2005).
- [90] Z. Yang, L. Mutter, M. Stillhart, B. Ruiz, Aravazhi., M. Jazbinsek, A. Schneider, V. Gramlich, and P. Günter, "Large-size bulk and thin-film stilbazolium-salt single crystals for nonlinear optics and THz generation," *Advanced Functional Materials* **accepted** (2007).
- [91] B. Ruiz, Z. Yang, V. Gramlich, M. Jazbinsek, and P. Günter, "Synthesis and crystal structure of a new stilbazolium salt with large second-order optical nonlinearity," *Journal Of Materials Chemistry* **16**(27), 2839–2842 (2006).
- [92] Z. Yang, M. Worle, L. Mutter, M. Jazbinsek, and P. Günter, "Synthesis, crystal structure, and second-order nonlinear optical properties of new stilbazolium salts," *Crystal Growth & Design* **7**(1), 83–86 (2007).
- [93] S. K. Kurtz and T. T. Perry, "A powder technique for evaluation of nonlinear optical materials," *Journal of Applied Physics* **39**(8), 3798–3813 (1968).
- [94] O. P. Kwon, B. Ruiz, A. Choubey, L. Mutter, A. Schneider, M. Jazbinsek, V. Gramlich, and P. Günter, "Organic nonlinear optical crystals based on configurationally locked polyene for melt growth," *Chemistry of Materials* **18**(17), 4049–4054 (2006).
- [95] L. Mutter, F. D. J. Brunner, Z. Yang, M. Jazbinsek, and P. Günter, "Linear and nonlinear optical properties of the organic crystal DSTMS," *Journal of the Optical Society of America B* **24**, 2556–2561 (2007).
- [96] S. Brahadeeswaran, S. Onduka, M. Takagi, Y. Takahashi, H. Adachi, M. Yoshimura, Y. Mori, and T. Sasaki, "Growth of high-quality DAST crystals for THz applications," *Journal of Crystal Growth* **292**(2), 441–444 (2006).

- [97] A. S. H. Hameed, W. C. Yu, C. Y. Tai, and C. W. Lan, "Effect of sodium toluene sulfonate on the nucleation, growth and characterization of DAST single crystals," *Journal of Crystal Growth* **292**(2), 510–514 (2006).
- [98] T. Taniuchi, S. Ikeda, Y. Mineno, S. Okada, and H. Nakanishi, "Terahertz properties of a new organic crystal, 4'-dimethylamino-N-methyl-4-stilbazolium p-chlorobenzenesulfonate," *Japanese Journal of Applied Physics Part 2-Letters & Express Letters* **44**(28-32), L932–L934 (2005).
- [99] M. Born and E. Wolf, *Principles of Optics* (Pergamon Press, Oxford, 1980).
- [100] A. Schneider, F. D. J. Brunner, and P. Günter, "Determination of the refractive index over a wide wavelength range through time-delay measurements of femtosecond pulses," *Optics Communications* **257**, 354–358 (2007).
- [101] B. Wyncke and F. Brehat, "Calculation of the effective 2nd-order non-linear coefficients along the phase matching directions in acentric orthorhombic biaxial crystals," *Journal of Physics B-Atomic Molecular and Optical Physics* **22**(2), 363–376 (1989).
- [102] A. Borreman, S. Musa, A. A. M. Kok, M. B. J. Diemeer, and A. Driessen, "Fabrication of polymeric multimode waveguides and devices in SU-8 photoresist using selective polymerization," *Proceedings Symposium IEEE* p. 83 (2002).

Acknowledgments

After about 5 years in the Nonlinear Optics Laboratory the time to finish comes. I have had many hours of fun, interesting research work and exciting findings, but also moments with feelings of agitation were present - not only because of missing the Wallis's sun. Finally, all came to a good end. Without helpers, all these would not have been possible. Therefore, I would like to thank specially

- Prof. Peter Günter, for giving me the possibility to make my PhD in his group,
- Prof. Marko Zgonik, for the support during my diploma thesis and the first year as a PhD student and for being the co-examiner at the PhD exam,
- Mojca, for all the corrections, discussions and quiet work you have done and for being so a good team leader,
- Andrea, with whom I have shared from the very beginning the same office, for his positive attitude, for encouraging me, for many fruitful discussions, for his help by plenty of Illustrator and Matlab problems, and all the hours we have spend together sitting side by side in the office,
- Daniele, for bringing vitality in the office, with discussions or loud phone calls, and also for making conferences, on which we have been, funnier and somehow a special event,
- Christian, for his support with computer problems and lab electronics,
- Jaroslav, for his expert and very careful sample preparation with the very delicate DAST crystals,
- Edwin, for designing and building all possible holders and apparatuses,
- Zhou, for developing plenty of new compounds,
- Blanca, Sturzi and Reto for growing the DAST crystals,
- Steffen, for his straightforward repairing of all possible machines,
- Manuel, for his expert writing of the structures with e-beam,
- Arno, for adjusting the fs laser and bringing it to the best performance,
- Tobias and Fabian, for the relaxing breaks at the bistro after lunch,
- Roger and Flurin, for shortening the breaks with top football,
- Hermann, for many funny discussions about politics, sport and all other possible topics, and all the others, for their help and support and providing the good spirit in this group.

Curriculum Vitae

Name	Lukas Mutter
Date of birth	May 15, 1977 in Visp (Switzerland)
1984–1990	Primary school in Ried-Brig
1990–1992	Secondary school in Brig
1992–1997	High school, Kollegium Spiritus Sanctus in Brig
1997–2002	Study of physics at the Swiss Federal Institute of Technology (ETH) in Zurich
2002	Graduation with a thesis on “ <i>Herstellung von Wellenleitern in DAST Kristallen</i> ” in the Nonlinear Optics Research Group of Prof. P. Günter
2002–2007	Research and teaching assistant in the Nonlinear Optics Group of Prof. Dr. P. Günter, ETH Zurich
2007	PhD thesis on “ <i>Nonlinear optical organic crystals for photonic applications</i> ”

List of publications

- L. Mutter, M. Jazbinšek, C. Herzog, and P. Günter
“Electro-optic and nonlinear optical properties of ion implanted waveguides in organic crystals”
submitted to Optics Express.
- L. Mutter, M. Koechlin, M. Jazbinšek, and P. Günter
“Direct electron beam writing of channel waveguides in nonlinear optical organic crystals”
Optics Express, in press.
- L. Mutter, F. D. J. Brunner, Z. Yang, M. Jazbinšek, and P. Günter
“Linear and nonlinear optical properties of the organic crystal DSTMS”
Journal of the Optical Society of America B, **24**, 2556-2561 (2007).
- L. Mutter, A. Guarino, M. Jazbinšek, M. Zgonik, P. Günter, and M. Doebeli
“Ion implanted optical waveguides in nonlinear optical organic crystal”
Optics Express, **15**, 629-638 (2007).
- L. Mutter, P. Dittrich, M. Jazbinšek, and P. Günter
“Growth and planar structuring of DAST crystals for optical applications”
Journal of Nonlinear Optical Physics & Materials, **13**, 559-567 (2004).
- L. Mutter, M. Jazbinšek, M. Zgonik, U. Meier, Ch. Bosshard, and P. Günter
“Photobleaching and optical properties of organic crystal 4-N, N-dimethylamino-4'-N'-methyl-stilbazolium tosylate”
Journal of Applied Physics, **94**, 1356-1361 (2003).
- S. J. Kwon, O. P. Kwon, J. I. Seo, M. Jazbinšek, L. Mutter, V. Gramlich, T. Schmid, R. Zenobi, Y. S. Lee, and P. Günter
“Highly nonlinear optical configurationally locked triene crystals containing unusually short C-C single bonds squeezed by intermolecular hydrogen bonds ”
in preparation.
- H. Figi, L. Mutter, C. Hunziker, B. J. Coe, M. Jazbinšek, and P. Günter
“Optical and nonlinear optical properties of a stilbazolium salt DAPSH crystal”
in preparation.
- Z. Yang, L. Mutter, M. Stillhart, B. Ruiz, S. Aravazhi, M. Jazbinšek, A. Schneider, V. Gramlich, and P. Günter
“Large-size bulk and thin-film stilbazolium-salt single crystals for nonlinear optics and THz generation”
Advanced Functional Materials, **17**, 2018-2023 (2007).

- Z. Yang, M. Wörle, L. Mutter, M. Jazbinšek, and P. Günter
“Synthesis, crystal structure, and second-order nonlinear optical properties of new stilbazolium salts”
Crystal Growth & Design, **7**, 83-86 (2007).
- O. P. Kwon, B. Ruiz, A. Choubey, L. Mutter, A. Schneider, M. Jazbinšek, V. Gramlich, and P. Günter
“Organic nonlinear optical crystals based on configurationally locked polyene for melt growth”
Chemistry of Materials, **18**, 4049-4054 (2006).